

Degradation of modular hip joint implants. A corrosion and tribocorrosion approach

THÈSE N° 8591 (2018)

PRÉSENTÉE LE 25 MAI 2018

À LA FACULTÉ DES SCIENCES ET TECHNIQUES DE L'INGÉNIEUR

GROUPE SCI STI SM

PROGRAMME DOCTORAL EN SCIENCE ET GÉNIE DES MATÉRIAUX

ÉCOLE POLYTECHNIQUE FÉDÉRALE DE LAUSANNE

POUR L'OBTENTION DU GRADE DE DOCTEUR ÈS SCIENCES

PAR

Angela BERMUDEZ CASTAÑEDA

acceptée sur proposition du jury:

Prof. P. Muralt, président du jury
Dr S. Mischler, directeur de thèse
Dr P. Schmutz, rapporteur
Dr C. Rieker, rapporteur
Prof. B. Jolles-Haerberli, rapporteuse



ÉCOLE POLYTECHNIQUE
FÉDÉRALE DE LAUSANNE

Suisse
2018

*To my beautiful butterfly
Ale, you are our upgraded version.
You are in our prayers and hopes.*

I would like to express my gratitude to Colciencias and Swiss Confederation for the financial support along this PhD.

Abstract

Total hip joint arthroplasty is a medical procedure to replace a natural failed joint by an artificial joint to improve the quality of life of the patient. In spite of its broad success, there is a concern about the relation between the presence of modular hip joint implants and health complications such as necrosis of surrounding tissues, adverse tissue reaction and high metal ions concentration in the body. Indeed, analysis of retrieved implants showed that modular interfaces undergo tribological and corrosion phenomena leading to wear and formation of surface films composed of a mixture of metallic and oxidized material.

In parallel, several degradation mechanisms have been proposed to explain what occurs in the modular joints. Those mechanisms are pitting, galvanic corrosion, hydrogen embrittlement, crevice-corrosion and fretting-corrosion. However, no consensus except for the recognized role of fretting-corrosion has been reached. Based on the required conditions for these mechanisms to happen, the two more likely occurring phenomena are fretting-corrosion and crevice-corrosion. Even though, several contradictions subsist about the effective incidence of crevice-corrosion on biomedical Ti and CoCr alloys.

Accordingly, the general goal of this work is to clarify and shed more light on the mechanisms responsible for modular implant degradation. The first research axis aims at identifying the occurrence of crevice-corrosion in modular hip joint configuration as well as to determine its contribution to the degradation of modular hip joint implants. As further step, this work aims at identifying and rationalizing through a predictive model the different mechanical and chemical mechanisms responsible for fretting corrosion degradation. The strategy taken here consists in the combination of tailored state of the art experiments and of advanced theoretical concepts related to the disciplines of corrosion and tribology.

The study of crevice-corrosion of Ti6Al4V and CoCr alloy was carried out in a configuration mimicking the geometrical crevice found in modular hip trunnions in contact with ceramic heads. The incidence of two different pH conditions and several potential applied was evaluated in NaCl 0.9% wt. The evolution of the potential was

followed inside and outside the crevice. The validity of the experimental approach was assessed by calibration with a well known crevice-corrosion sensitive system (FeCr15% in sulfuric acid). Interestingly, no potential drop or evidence of degradation was found when testing CoCr and Ti biomedical alloys up to a duration of one month. In addition, an existing IR-Voltage model to predict the occurrence of crevice-corrosion was used to calculate, based on the experimental results and data from the literature, under which condition crevice-corrosion occurs in hip joint configuration. The validity of the model was verified through quantitative comparison with the experimental results obtained with the FeCr15% in H₂SO₄ model system. This IR-Voltage model predicts that in a wide range of passivation potential, crevice gap and conductivity, biomedical alloys cannot undergo crevice-corrosion. The model indicates that crevice corrosion can occur only under the unrealistic condition that the electrical conductivity of the body fluid surrounding the implant approaches the one of drinking water.

According to these results, the attention was addressed towards fretting-corrosion phenomena as the main responsible for modular hip joint implants deterioration.

A predictive model of fretting corrosion wear integrating mechanical and chemical phenomena has been developed. A set of experiments was carried out in NaCl 0.9%wt under cathodic and anodic potential; in order to study the degradation mechanisms of the modular hip joint implants under different electrochemical and mechanical conditions. It was observed that worn material comes from the third body formed under fretting-corrosion. The properties of this third body depend on the prevailing electrochemical conditions in the contact, thus determining the wear rate. Considering these observations and taking into account mechanical and chemical parameters, this work proposes a fretting wear model inspired from an existing tribocorrosion model based on the mass balances between the bulk material, the third body and the electrolyte. This model allows determining wear based on crucial electrochemical and mechanical parameters and constitutes a first step towards the development of theoretical tools scaled to modular hip joint configuration.

Key words: modular hip joint implants, crevice-corrosion, biomedical alloys, fretting-corrosion, degradation, third body layer, tribocorrosion.

Résumé

L'arthroplastie totale de la hanche est une procédure médicale visant à remplacer une articulation défaillante par une articulation artificielle dans le but d'améliorer la qualité de vie du patient. En dépit de son succès général, il y a une crainte concernant une relation entre la présence d'implants modulaires de l'articulation de la hanche et des complications de santé telles que la nécrose des tissus environnants, la réaction indésirable des tissus et une concentration élevée d'ions métalliques dans le corps. En effet, l'analyse d'implants récupérés après une arthroplastie a montré que les interfaces modulaires subissent des phénomènes tribologiques et corrosifs conduisant à de l'usure et à la formation de films de surface composés d'un mélange de métaux et d'oxydes.

En parallèle, plusieurs mécanismes de dégradation ont été proposés pour expliquer ce qui se passe dans une articulation modulaire. Ces mécanismes sont la corrosion par piqûres, la corrosion galvanique, la fragilisation par l'hydrogène, la corrosion cavernueuse et la fretting-corrosion. Cependant, aucun consensus, à l'exception du rôle reconnu de la fretting-corrosion n'a été atteint. Sur la base des conditions requises pour que ces mécanismes se produisent, les deux phénomènes les plus probables sont la corrosion de contact et la corrosion cavernueuse. Toutefois, plusieurs contradictions subsistent concernant l'effet de la corrosion cavernueuse sur les alliages biomédicaux Ti et CoCr.

Par conséquent, l'objectif général de ce travail est de clarifier et de mieux comprendre les mécanismes responsables de la dégradation des implants modulaires. Le premier axe de recherche a pour but d'identifier le taux d'apparition de la corrosion cavernueuse dans une articulation modulaire de la hanche ainsi que de déterminer sa contribution concernant la dégradation de l'implant. Dans un deuxième temps, ce travail vise à identifier et à rationaliser à travers un modèle prédictif les différents mécanismes mécaniques et chimiques responsables de la dégradation par corrosion de contact. La stratégie utilisée ici consiste en l'association d'expériences adaptées et de concepts théoriques avancés liés à la corrosion et à la tribologie.

L'étude de la corrosion cavernueuse des alliages Ti6Al4V et CoCr a été réalisée dans une configuration imitant la géométrie de la crevasse trouvée dans les tourillons modulaires de la hanche en contact avec les têtes en céramiques. L'effet de deux valeurs de pH et de différents potentiels a été évalué dans une solution de NaCl 0.9%. L'évolution du potentiel a été suivie à l'intérieur et à l'extérieure de la crevasse. La validité de l'approche expérimentale a été évaluée par étalonnage avec un système de corrosion cavernueuse connu (FeCr15% dans une solution d'acide sulfurique). Curieusement, aucune chute de potentiel ou d'évidence de dégradation n'a été observé lors d'essais sur les alliages

biomédicaux CoCr et Ti d'une durée de 1 mois. En outre, un modèle IR-Voltage existant pour prédire l'apparition de la corrosion carvencuse a été utilisé pour calculer, sur la base des résultats expérimentaux et des données de la littérature, sous quelles conditions la corrosion de contact se produit dans la configuration de l'articulation de la hanche. La validité du modèle a été vérifiée par comparaison quantitative avec les résultats expérimentaux obtenus avec le système modèle FeCr15% dans H₂SO₄. Ce modèle IR-Voltage prédit que dans une large gamme de potentiel de passivation, de taille de crevasse et de conductivité, les alliages biomédicaux ne subissent pas de corrosion caverneuse. Le modèle indique que la corrosion carvencuse ne se produit que dans des conditions irréalistes où la conductivité électrique du fluide corporel environnant l'implant se rapproche de celle de l'eau distillée.

Selon ces résultats, l'attention a été portée sur le phénomène de corrosion de contact comme étant le principal responsable de la détérioration des implants modulaires de l'articulation de la hanche.

Un modèle prédictif d'usure par corrosion par frottement intégrant des phénomènes mécaniques et chimiques a été développé. Un ensemble d'expériences a été réalisé dans NaCl à 0,9% en poids sous potentiel cathodique et anodique; afin d'étudier le mécanisme de dégradation des implants modulaires de l'articulation de la hanche dans différentes conditions électrochimiques et mécaniques. Il a été observé que le matériau usé provient du troisième corps formé sous la corrosion par frottement. Les propriétés de ce troisième corps dépendent des conditions électrochimiques dominantes dans le contact, déterminant ainsi le taux d'usure. Considérant ces observations et prenant en compte des paramètres mécaniques et chimiques, ce travail propose un modèle d'usure par frottement inspiré d'un modèle de tribocorrosion existant basé sur les bilans massiques entre le matériau en vrac, le troisième corps et l'électrolyte. Ce modèle permet de déterminer l'usure en fonction de paramètres électrochimiques et mécaniques cruciaux et constitue un premier pas vers le développement d'outils théoriques adaptés à la configuration modulaire de l'articulation de la hanche.

Key words : implants modulaires d'articulation de la hanche, corrosion caverneuse, alliages biomédicaux, corrosion de contact, dégradation, couche de troisième corps, tribocorrosion



Acknowledgments

I owe very deep gratitude to my advisor Stefano Mischler who gave me the opportunity to work under his supervision. This PhD changed my life. Thank you for your guidance, patience and your confidence in realizing this thesis. Thank you, for the long scientific discussions, which enhanced my knowledge in the tribocorrosion field.

I would like to acknowledge Brigitte Jolles, Claude Rieker and Patrick Schmutz, for accepting to be the jury members of this thesis. The discussions and the feedbacks were an important complement to this work.

My most sincere gratitude goes to Javier Navarro and Alex Roda, professors from Universitat Politècnica de Valencia. Your help and contribution from the mathematical and mechanical point of view was crucial in the development of this project. The Matlab routine to calculate the VonMises stresses was provided by Alex Roda.

I would like to thank as well the Atelier MX, especially Pierre-André Despont and Yves Ruschetta, their professional help and creativity allowed me to develop the experimental part of this thesis.

I was very lucky to know Nicholas Xantopoulos for his energy, cheerfulness and enthusiastic friendship and also for having introduced me to his Greek culture and music. Your love for mountains almost killed mine but thanks to you I learned to enjoy the alpine landscapes. Also, I want to thank Pierre Mettraux for his technical help, his ski lessons and his reminders to keep my smile. Thank you as well to Sandra Guadalupe, for introducing me to the Swiss – Ecuadorian world. I keep in my heart the beautiful time that we shared together. To Shoufan Cao who opened my eyes to Chinese's culture; Thanks for your humor and constant kind help.

My gratitude goes also to the TIC's girls. I was very lucky to work in your company. You were a big support during my happiest, hardest and sometimes darkest moments. Leili, I will not forget your sweetness and how much our cultures share. Valentine, it was a great pleasure to discover the admirable and talented friend that you are. The scientific discussions, the ski lessons and more especially your love, company and support girls will be always with me.

I would like to thank as well my colleagues from TIC's lab: Fabio, Vance and all the master students that passed by the lab. Thank you for the scientific discussion and the nice apéros that we shared, I will miss the Christmas dinners.

I am also deeply grateful to the Roda-Igual family. You were my support and the optimistic spirits during my last two years here. I never will forget your enthusiasm about science and tribocorrosion. I enjoyed all the political, literary and emotional talks that we had. Thank you for opening your house's door to me and sharing your life with me and also letting me get to know the beautiful, smart and sweet Pau and Lara, I love them.

I want to express my gratitude to ACIS community, which gave me the opportunity to work for our country and to meet amazing and smart people working untiringly for Colombia. Personally and professionally it was a great experience.

This achievement is also thanks to my dear Marcela, Luciana, Laura, Lucia, Nathalie, Lina, Juliana, María Alejandra and Audrey. Powerful, admirable and wonderful women able to open any door in front of them. My dear friends thank you for the laugh, love and even tears that we shared. Thank you Jhonny and Nicolas, without your advice, jokes and company, this time in Switzerland would have been less fun. All of you gave me colourful and warm days, which made my roots stronger.

I would like also to thank the group of the Confederation scholarship holders and Karin. This group of people from different nationalities left me with beautiful moments around Switzerland.

I want to thank Yura, Cris, Mauro, Ale and Juan, your visits were precious experiences for me. To all my dear friends Juli, lore, Caro, Tati, to the "Cronopios: Chris, Carlitos, Audrey and Ed", you were a beautiful company and source of love from distance. To Jaz and Angélica, you were my angels in the first year. To Juanda, thank you for the drinks and the skepticism that we sheared during my first years. Thank you all for the nice time we had together. All of you are like a breath of air plenty of love.

Thanks to my dear Mel, your support, love, humor and strength are treasures for me. You are a lovely person.

I'm deeply grateful to my dear professor Juan Guillermo Castaño, who encouraged me to start this adventure. You are a great human and scientific support. Thanks also to Adriana and Johanna, Diana and Diego, the Colombian people interested in tribocorrosion that came to TIC's lab. I had beautiful memories of our time together, the long scientific journeys and discussions.

I am very grateful to my family, for their support and for believing in me. I would like to thank specially my parents: you live in my hearth, in my thoughts and in my words. As well as my sister and my nice, who are my best reasons for continuing every day.

Finally, I would like to thank Javier. I never imagined that coming here I was going to find you and you were going to find me. Thank you for your love, your music, your patience and your support.

Table of contents

| | |
|---|-----|
| Abstract | i |
| Résumé | iii |
| Acknowledgments | v |
| Table of contents | vii |
| 1. Introduction..... | 1 |
| 1.1 Modular Hip Joint Prostheses | 1 |
| 1.2 Materials used in modular hip joint implants..... | 5 |
| 1.3 Trunnionosis and retrieved implants findings..... | 6 |
| 1.3.1 Metal ions concentration..... | 6 |
| 1.3.2 Debris and tribofilms | 6 |
| 1.3.3 Degradation mechanisms..... | 8 |
| 1.4 Statement of the problem | 10 |
| 2. State of the art | 12 |
| 2.1 Crevice-corrosion fundamentals | 12 |
| 2.1.1 Crevice-corrosion generalities..... | 13 |
| 2.1.2 Crevice-corrosion IR-Voltage Model | 15 |
| 2.2 Crevice-corrosion of biomedical alloys..... | 17 |
| 2.2.1 Biomedical alloys | 17 |
| 2.2.2 Crevice corrosion of biomedical alloys..... | 19 |
| 2.3 Fretting Corrosion wear | 24 |
| 2.3.1 Definition and generalities | 24 |

| | | |
|-------|---|----|
| 2.3.2 | Two body models | 25 |
| 2.3.3 | Third body models..... | 27 |
| 2.3.4 | Third body In-Vitro evidence. Observations | 29 |
| 2.3.5 | Ti6Al4V and CoCr under fretting corrosion tests..... | 30 |
| 3. | Objectives and strategy | 32 |
| 3.1 | Goal..... | 33 |
| 4. | Crevice-corrosion | 34 |
| 4.1 | Crevice-corrosion experiments | 34 |
| 4.1.1 | Materials..... | 35 |
| 4.1.2 | Cell configuration | 38 |
| 4.1.3 | Electrical assembly and data acquisition | 42 |
| 4.1.4 | Chemical conditions | 43 |
| 4.2 | Results..... | 45 |
| 4.2.1 | Crevice-corrosion of Stainless Steel - FeCr15%..... | 45 |
| 4.2.2 | Crevice-corrosion behavior of CoCr | 50 |
| 4.2.3 | Crevice-corrosion behavior of Ti6Al4V | 53 |
| 4.2.4 | Summary of results..... | 57 |
| 5. | Crevice-corrosion model | 59 |
| 5.1 | Crevice corrosion model applied to FeCr15% system..... | 59 |
| 5.2 | IR crevice – corrosion model in biomedical alloys | 60 |
| 5.2.1 | IR-Voltage model parameters | 61 |
| 5.2.2 | CoCr alloys..... | 61 |
| 5.2.3 | Ti6Al4V alloy | 63 |
| 5.3 | Model extrapolation..... | 64 |
| 5.3.1 | CoCr alloy | 64 |
| 5.3.3 | Summary | 69 |
| 6. | Fretting-corrosion experiments..... | 70 |
| 6.1 | Instrumentation and materials..... | 70 |
| 6.2 | Experimental conditions..... | 71 |
| 6.3 | Results..... | 72 |

| | | |
|-------|---|-----|
| 6.4 | Surface characterization..... | 79 |
| 6.4.1 | Anodic conditions (0.5V) | 79 |
| 6.4.2 | Cathodic conditions (-1V) | 85 |
| 6.4.3 | Acting mechanisms | 90 |
| 7. | Third body model..... | 92 |
| 7.1 | Physical model..... | 92 |
| 7.2 | Compartments and flows | 95 |
| 7.3 | Mass balance..... | 97 |
| 7.4 | Model calibration..... | 98 |
| 7.4.1 | Passivation charge density | 98 |
| 7.4.2 | Proportionality constants K1 and K2..... | 99 |
| 7.4.3 | Stress transmission factor | 100 |
| 7.4.4 | Determination of unknown parameters K3 and K5 | 102 |
| 7.5 | Model prediction | 104 |
| 8. | Discussion..... | 108 |
| 9. | Conclusions..... | 111 |
| 10. | References | 113 |

List of symbols

| | |
|----------|---|
| C_1 | Compartment related to the total mass of the metallic substrate |
| C_2 | Compartment related to the metallic particles in the friction film |
| C_3 | Compartment that contains oxide particles in the friction film |
| C_4 | Compartment of metal particle concentration in the electrolyte or the re-deposition |
| d_c | Critical distance |
| d_{ox} | Thickness of the oxide layer |
| D_x | Amplitude displacement (μm) |
| σ | Solution conductivity ($\Omega^{-1} \text{cm}^{-1}$) |
| E | Potential (V) |
| E_{ap} | Applied Potential (V) |
| E_p | Passive potential (V) |
| E | Young's modulus (MPa) |
| E' | Effective Young's Modulus (MPa) |
| F | Faraday's constant ($\text{C}\cdot\text{mol}^{-1}$) |
| F_N | Normal force applied (N) |
| G | gap (cm) |
| H | Material hardness ($\text{N}\cdot\text{m}^{-2}$) |
| H_{TB} | Third body hardness ($\text{N}\cdot\text{m}^{-2}$) |
| I | Current (μA) |
| x | |

| | |
|---------------------|---|
| K_{chem} | Proportionality constant for chemical wear |
| K_{mech} | Proportionality constant for chemical wear |
| K_1 | Proportionality constant |
| K_2 | Proportionality constant |
| K_3 | Proportionality constant - wear rate |
| K_4 | Proportionality constant |
| K_5 | Proportionality constant |
| k | Sides wall in the crevice |
| l | Crevice length (cm) |
| M_{ox} | Molecular weight of the oxide (g.mol^{-1}) |
| m_{ox} | Mass of the oxide layer |
| M_r | Molecular weight |
| n | Valencia number |
| $n_{\text{mol ox}}$ | Oxide moles number (mol) |
| n_{ox} | Number of moles forming the oxide layer |
| η | Viscosity (Pa.s) |
| ρ | Lubricant density (g.cm^{-3}) |
| ρ_{met} | Metal density (g.cm^{-3}) |
| ρ_{ox} | Oxide density (g.cm^{-3}) |
| P | Potential (V) |
| Q_p | Passivation charge density (C.m^{-2}) |
| r_{ox} | Oxide stoichiometric relation |
| R' | Effective radius of curvature (mm^2) |
| STF | Stress transmission factor |
| F_T | Tangential force (N) |
| V'_{chem} | Chemical volume of the system (Kg.s^{-1}) |
| V_{mec} | Mechanical volume (Kgs^{-1}) |
| V_{ox} | Volume of the oxide layer |
| v_s | Sliding velocity of the fretting system (m.s^{-1}) |
| w_2 | Metal particles proportion |
| z | Valence number of ions in the oxide |

| | |
|----------|---|
| ϕ_1 | Flow of metal particles removed from the substrate by mechanical wear (Kg.s ⁻¹) |
| ϕ_2 | Flow of material detached from the substrate due to the wear accelerated corrosion (Kg.s ⁻¹) |
| ϕ_3 | Mass flow leaving the contact from the third body (Kg.s ⁻¹) |
| ϕ_4 | Flow of material particles that once are broken and leave the third body layer they remain in the contact being reincorporated to the layer again (Kg.s ⁻¹) |
| ϕ_5 | Chemical oxidation of metal particles inside of the friction film (Kg.s ⁻¹) |

1. Introduction

1.1 Modular Hip Joint Prostheses

Hip joint prostheses are implanted as artificial joints in human body to replace failed natural joints. In general, this surgical procedure improves mobility and alleviates patients' pain. There have been more than 2.5 millions hip joint replacements performed in the United States until 2010, while in Australia about 480.000 were documented in the annual report of the Australian Orthopaedic Association 2017 (AOA) [1]–[3].

In a natural hip joint, cartilage covering the femoral head ensures soft movements. In addition, the distal portion of the femur provides stiffness and transmits forces required for the movement.

Hip joint replacement consists of the substitution of the upper part of the femur and the acetabulum. The medical procedure of implanting a hip joint replacement, known as total hip arthroplasty (THA), is required when fractures or diseases damage the natural joint, as Figure 1-1 shows [4].

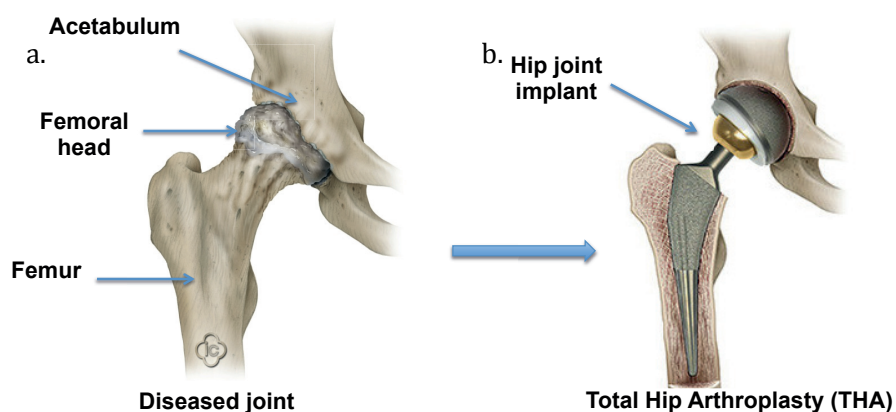


Figure 1-1. a) Hip joint degenerated by a disease b) artificial hip joint, adapted image [4]

Over time, several hip joint prosthesis designs and materials have been developed to satisfy the necessary mechanical, chemical and biological requirements.

One of the most commonly used designs is made of two components: the acetabular socket and the monoblock implant. As illustrated in Figure 1-1, in a monoblock device, the femoral head, neck and stem are in one single piece [5].

Nonetheless, one single material is unable to provide the variety of properties that an implant is required to present at each given position along its length. For instance, while in the femoral head wear resistance is essential, in the neck and the stem, stiffness, elasticity and biocompatibility are required. So, consequently in the monoblock implants typically either fracture on the neck, related to fatigue, or wear on the femoral head are observed.

To avoid monoblock prosthesis failures, modularity was introduced around the 60's. However, it was not until the 80's that its application gained momentum [6], [7]. Modular design facilitates tailoring of the prosthesis according to patient's anatomy and revision procedures. In addition, the properties of different materials could be combined in one single configuration.

There are two kinds of modularity. One where the femoral head is separated from the stem – known as unipolar model – shown in Figure 1-2b. A second configuration where the neck is separated from the stem and a second junction is created, this model is called bipolar (Figure 1-2c). Currently, the main used design is the uni-polar model [1], [6].

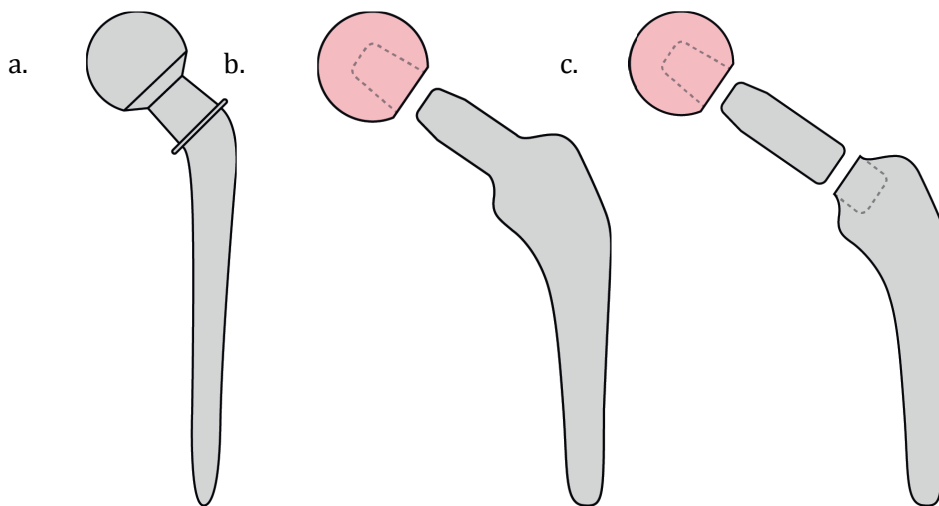


Figure 1-2. Hip joint implants design a) monoblock, b) unipolar and c) bipolar prosthesis

In spite of the advantages, modularity can cause several health issues related to ions and particles released from the materials. Some examples include: Adverse Tissue Reaction (ATR), cutaneous reaction, tissue necrosis and high metallic ions level in the blood, among

others. In a literature review, Esposito et al [6] found these modularity problems, started to increase since 2010, as a consequence of the increment of arthroplasty surgeries with modular designs.

Modular hip joint prosthesis work under severe conditions: i) variable load (depending on gait phase) that can reach more than three times the body weight [8].; ii) low amplitude relative movements with variable frequencies; iii) contact with corrosive synovial fluids and average temperature of 37 °C [9], [10].

So, particles and ions release are related to the degradation mechanisms, that in turn are governed by several factors such as: load (weight), movement, body fluids in contact with the artificial joint, implant design and materials.

Modular Design

In a modular prostheses, the connection between the femoral head/neck is done through a male part called *trunnion* and a female part known as *bore* [11], see Figure 1-3. The femoral neck/stem junction is composed of a male and female connection as well. In both cases, the mechanical contact is considered as cone on cone.

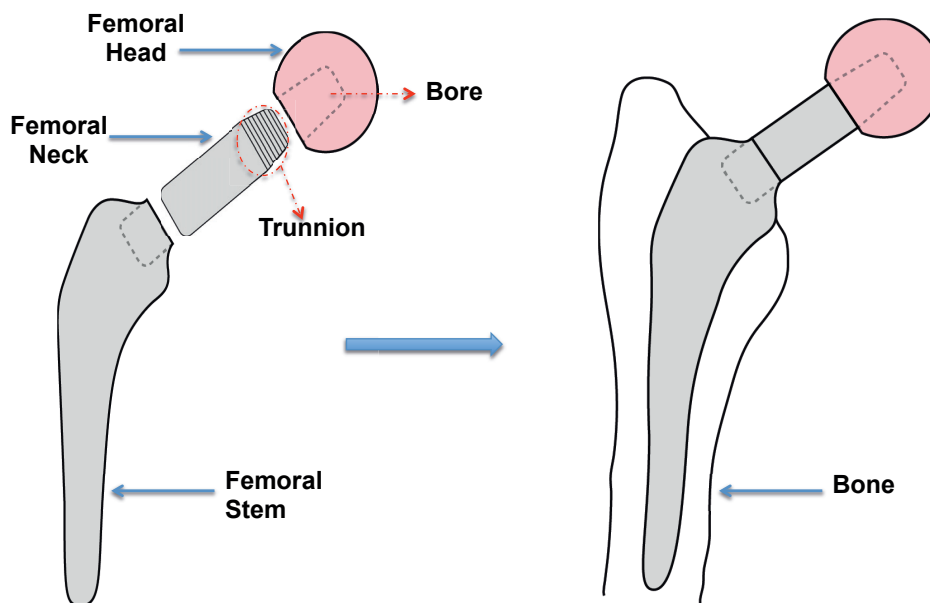


Figure 1-3. a) Bipolar prosthesis parts and b) Prosthesis implanted

Several aspects should be considered in the trunnion design namely surface finish, crevice depth and geometry of the trunnion-bore junction.

Surface finish of the female and male parts can affect mechanical and chemical behavior of the joint. Some trunnion designs have thread patterns on the surface to increase fixation, even though it has been reported that smooth surfaces and longer tapers decrease modular degradation [12]–[14].

In a modular design, a narrow gap (also called crevice) is formed between the modular junctions: femoral head-neck and femoral neck-stem. Crevice size depends on geometry and tolerances of modular pieces. It is also affected by patient's movements and physical exertion. Bigger gaps facilitate the entry of synovial fluid into the joint.

Materials that can be potentially coupled to form the femoral head-neck junction are the following: metal/metal and ceramic/metal. The material choice is important for the mechanical behavior of the prosthesis and also plays a role on the crevice configuration; since the geometrical gap depends on the material couple.

The mismatch angle recommended for ceramic/metallic junction is positive to avoid impacts and tension on the ceramic piece. Conversely, for metal/metal couple this angle is negative, allowing the fixation without negative effects due to the resilience and deformability of metallic materials. Both cases are represented in Figure 1-4.

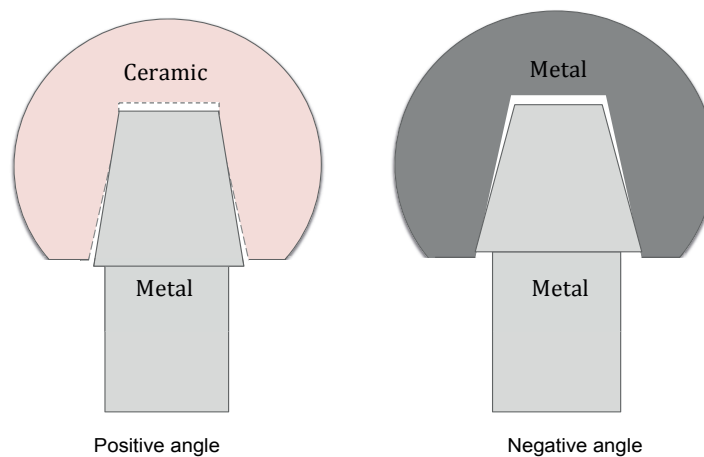


Figure 1-4. Recommended hip joint implants angles, adapted image [17]

For bore and trunnion connection, angles difference accepted by the industry are around 0.0167° [15]. This tolerance avoids angular mismatches that favor asymmetric load distribution and fixation problems. A bigger angle difference can induce degradation by tribochemical processes [14], [16].

However, in spite of the recommended tolerances, in a retrieval study where 50 ceramic heads and 50 metallic heads were analyzed, angles differences were found between 0.10 and 0.20° [17].

On the other hand, during the THA surgery the femoral head is hammered into the femoral neck to avoid micro-motion and to ensure fixation between the modular pairs of the implant. The assembly forces between modular parts can reach $4 - 6.7$ kN [18], [19]. Higher fixation forces generate lower freedom of movement. That is especially true if the trunnion surface presents a thread pattern where the pattern can deform as a result of the impact [12], [18], [20], [21].

Finally, clean and dry surfaces must be guaranteed when assembling the different parts. Contamination can contribute to generation of wear, relative movements between the parts and asymmetric application of forces [22].

1.2 Materials used in modular hip joint implants.

To ensure efficient performance of the hip joint implant, specific material properties must be considered: elasticity, yield stress, fatigue, hardness, wear resistance, corrosion resistance, biocompatibility and biofunctionality [23], [24].

Ceramic materials such as Alumina (Al_2O_3) and Zirconia (ZrO_2) are used in femoral heads, due to their wear resistance and non-reactive behavior.

Biomedical alloys used are mainly Titanium (Ti) and Cobalt-Chromium (CoCr) alloys. The corrosion resistance of these passive metals lies on the spontaneous formation of a surface oxide layer when in contact with air or water [25].

Femoral neck and stem parts are manufactured with Ti alloys, due to its corrosion resistance, high tensile strength (100-120 GPa) and biocompatibility [5], [26], [27]. However, its limited wear resistance prevents its use in the joint contact [28].

Conversely, Cobalt-Chromium (CoCr) alloys have been widely used for producing femoral heads because of their wear resistance and the good mechanical properties and corrosion resistance.

Modular hip joint parts under variable load, relative movement and in contact with body fluids can expose biomedical alloys to the simultaneous phenomena of wear, passivation and depassivation. The combination of all these processes leads to a tribocorrosion phenomenon, which leads the deterioration of modular hip joint implants associated to the effect of debris particles on tissues and high metal ion levels in the blood. In consequence, it is of the utmost importance to elucidate the deterioration mechanisms and governing factors in those modular hip joints.

Even though several deterioration mechanisms have been invoked to explain hip joint implants degradation, the acting mechanical and chemical interactions are not yet well understood. In consequence, there is an apparent need for mechanistic approaches that identify the main responsible mechanisms and the conditions required for their occurrence. Therefore, there is a need for systematic investigations aimed at improving our understanding of the involved phenomena.

1.3 Trunnionosis and retrieved implants findings

Trunnionosis is known as the material degradation process between the modular joints, femoral head-neck and neck stem junction, where metal ions, corrosion products and debris are released [29], [30].

Wear debris and metallic particles tend to remain on site; therefore they can often be found agglomeration in the surrounding tissue. This problem is particularly noticeable with CoCr alloys. These particles can reach sizes from few nanometers to 400 micrometers [31]–[34].

In contrast, ions can either stay in the vicinity of the joint or be transported through bloodstream to organs such as liver, spleen, among others [6] [31]–[34]. So far, no evidence of negative long term effects of these mobile ions on human health has been found for Ti and CoCr[6] but there is a big concern about the poisoning due to the Cobalt dissolution [35], [36]. Still, several works related to the control of cobalt, chromium, titanium and aluminum levels in serum and urine have been published.

1.3.1 Metal ions concentration

Jacobs et al [37], found a dramatic increase in the concentration of chromium, titanium and cobalt levels in a controlled group of patients with a modular hip implant made in Ti and CoCr alloys after 36 months.

Cooper et al [32] also studied bipolar hip joint prostheses, where the stems were made of TiMoZrFe, femoral necks of CoCr and femoral heads of ceramic material and CoCr. In all cases higher cobalt and chromium ion levels were found compared to the acceptable values in the serum; the highest registered values were the cobalt values.

Gkagkalis et al [31] reported in 2015 a retrieval study of patients with bipolar hip joint implants. Stems were made of Ti6Al4V, femoral neck in CoCr alloys and ceramic femoral heads were used. Chromium and cobalt levels were also controlled. Findings coincide with the study of Cooper et al [32], where higher cobalt ion levels were measured compared to the acceptable values.

1.3.2 Debris and tribofilms

Gkagkalis et al [31] also reported debris, wear and corrosion products on tapers of explanted femoral necks (Figure 1-5). The authors found a layer, as shown in Figure 1-6b, in the femoral neck-stem junction, which is a mixture of titanium, chromium and cobalt

oxides. Degradation was attributed to the incomplete contact between the surfaces of the two modular parts that allow micro-movements. Higher proportion of Cr in the layer was explained by the tendency of chromium to precipitate in neutral pH as the one of the synovial fluid. Titanium particles found in the neck surface were attributed to the mass transfer from the femoral stem [31].

This kind of degradation was also found in other independent study by Huber et al [33] where 11 modular hip joint explants were analyzed. Femoral heads and stems were made in CoCr alloy and Ti6Al4V, respectively. In this case, thin layers were found in the head-neck junction, on the surface of both pieces as shown in Figure 1-6. The chemical analysis of one deposit found in the surface of the trunnion revealed that the layer is a mixture of Cr and Ti oxides. Additionally, corrosion products and metallic particles, where Cr and Ti were detected, were extensively found in the tissue surrounding the prostheses on 9 of 11 studied cases.

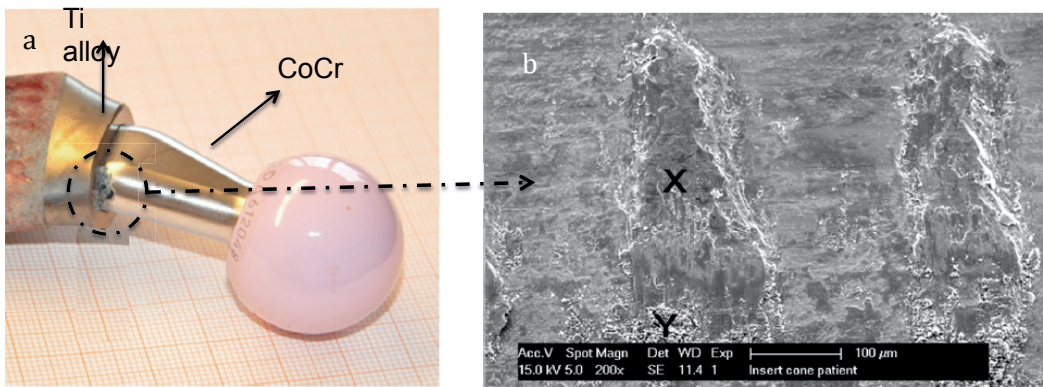


Figure 1-5. a) Modular hip joint explanted with fretting corrosion at the femoral stem-neck junction b) tribofilm found on the neck junction, image adapted from Gkagkalis et al [31].

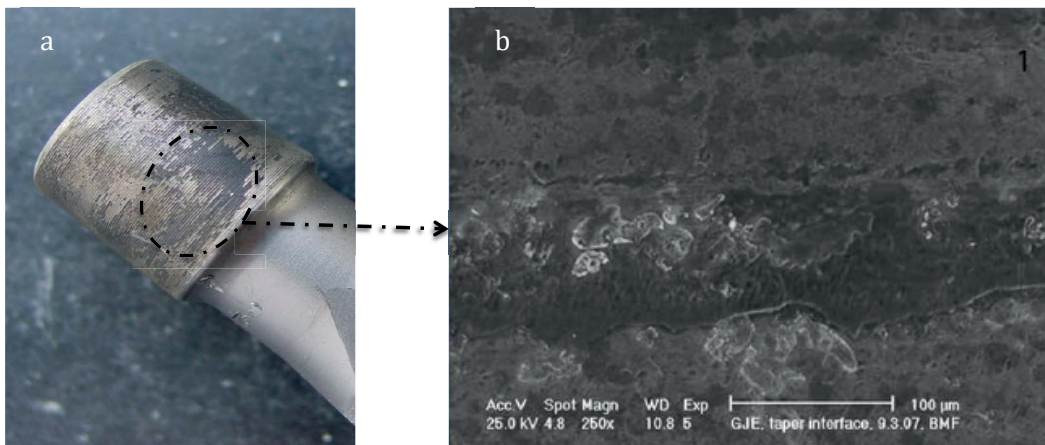


Figure 1-6. a) Tapered neck from modular hip joint implants with signs of damage, b) Scanning electron microscopy of the cone [33]

Those layers, called tribofilm, have been reported in several case studies for metal on metal couples on the femoral head/neck junction [38]–[41] and less frequently in ceramic on metal couples [32], [42]. This tribofilm act as a *third body*, which can be defined as a layer formed between two materials in contact under mechanical and chemical action. This third body is exposed to mechanical stresses and chemical reactions in the same way that joints operate. Third body layer has an effect on the differences in velocity of the pieces in contact, force distribution and the real surface area exposed to the human environment [43]–[45].

Accordingly, metallic and oxidized particles found in the surrounding tissue as well as the metal ions travelling along the body are originated from material ejected or released from these tribofilms. Therefore, understanding how these tribofilms are formed and identifying the main factors that govern their properties are relevant to modular hip joint degradation issues.

1.3.3 Degradation mechanisms

Several degradation mechanisms have been suggested for modular degradation: Fretting-corrosion, crevice-corrosion, pitting, galvanic-coupling and hydrogen embrittlement. Nowadays, there is a consensus about the occurrence of fretting corrosion phenomena, as the product of small amplitude motions, load and environmental conditions [10]. Furthermore, third body formation is characteristic of materials under this degradation mechanism.

In the following paragraphs crevice-corrosion, pitting, galvanic-coupling and hydrogen embrittlement and fretting-corrosion are discussed.

Crevice-corrosion

This degradation mechanism is a well-known autocatalytic process that concerns passive metals. This localized corrosion mechanism takes places in presence of a cavity, where the oxygen concentration is limited by the mass transport. Then, this oxygen depletion induces a difference between potential registered outside and inside of the cavity. As a consequence, there is a disruption of the passive film, which generates material dissolution and corrosion into the cavity[46].

Crevice-corrosion has been proposed as a degradation mechanism due to the special geometry configuration of modular implants. Body temperature and aggressive species from the body fluids have been considered also as parameters that favor this kind of degradation mechanism [38], [40]. However, some aspects remain unclear about crevice-corrosion taking place in modular hip joint implants from the electrochemical and chemical point of view.

Firstly, in a modular junction, material depassivation occurs by mechanical action between the modular parts. Then, to avoid repassivation and generate the active-passive cell, specific geometrical, electrochemical and chemical conditions are needed in the joint. However, no evidence of the formation of an active-passive cell for CoCr and Ti alloys under modular hip joint configuration have been reported.

Secondly, CoCr and Ti alloys are recognized for their resistance to crevice-corrosion at low temperature. Crevice-corrosion degradation has only been reported for Ti alloys in systems at high temperature conditions ($>100^{\circ}\text{C}$) [47]–[49].

Whether or not crevice-corrosion degradation occurs in modular hip joint configuration is controversial.

Pitting corrosion

Pitting-corrosion is a form of localized corrosion involving the local destruction of the passive film followed by high dissolution rates. This mechanism has been proposed as possible degradation mechanism because pits were observed in some modular parts. However, the likelihood of such phenomena could not be confirmed by in vitro tests.

About pits formation, those have been observed in tribofilm but as a consequence of conditions or mechanical fatigue of the material derived from fretting conditions [50], [51]. In that way, the occurrence of holes can be attributed to a different mechanisms than pitting corrosion.

In addition, Ti and CoCr alloys are recognize for their resistance to this kind of localized corrosion [46], [52] even under simulated body fluids and different electrochemical conditions [53].

In summary, there are no evidences supporting the appearance of pitting-corrosion or it has been considered as very unlikely.

Galvanic-coupling

This is a form of corrosion occurring when two dissimilar metal are in contact and exposed to the same electrolyte. In the contact, the corrosion rate of the less noble metal will increase. Although this degradation mechanism could take place in artificial joints, Trunnionosis also occurs in ceramic on metal contacts, in which the ceramic is well known to be electrochemically non-reactive [32], [42]. The effect of the particular conditions inside of the body on the material electro chemical-potential are not well understood.

Hydrogen embrittlement

Hydrogen embrittlement is a degradation mechanism caused by the diffusion of hydrogen atoms in the metallic matrix, which becomes more brittle, thus more prone to fracture. It has been proposed as a corrosion mechanism from the observation of retrieval implants made in Ti alloy [54]. However, until now, no study has reported this phenomenon for modular parts in CoCr alloys.

The generation of hydrogen, and thus embrittlement, on metallic surfaces immersed in aqueous solutions requires either very low pH values (high acidity) or low potential. Electrochemical potentials of biomedical alloys inside of the human body are unknown. However, Madina et al [44] electrochemically generated hydrogen on titanium alloys and found that no embrittlement occurs above very cathodic potentials of -1.5 V (Ag/AgCl).

With respect to pH, Igual et al [55] found that synovial fluid's pH varies around 7. Those values correspond to patients with inflammation, which means that low pH is not a natural characteristic of the synovial fluid. Likewise Virtanen et al [9] reported pH values from 4.7 to 7.7.

Those evidences leads to the conclusion that hydrogen embrittlement is not a driving force for modular hip joint degradation.

Fretting-corrosion

Fretting-corrosion is widely known for being the cause of wear, metal ions release and debris coming from uni-polar or bi-polar prosthesis. In consequence, the interest to understand fretting-corrosion phenomenon encouraged the development of fretting corrosion in vitro test, where third body could be reproduced [45], [56]–[58].

Besides the environment, modular designs features have been analyzed as factors that influence fretting–corrosion in modular hip joint implants. Taper's length, head diameter and specially, impact force of the assembly, surface roughness as well as the angle mismatch between the taper and the internal cone of the head have been found as a critical factors [18], [15], [59], [60].

In parallel, theoretical models have been proposed to describe tribochemical processes where a friction film influences deterioration [44], [61], [62]. However, there is still a lack of knowledge about the third body formation and the fretting-corrosion conditions required for it. An approach that integrates what is known from in-vitro experiments and theoretical models is also missing and it is needed to explain retrieval findings.

1.4 Statement of the problem

The clinical problems associated with the degradation of modular junctions encourage developing appropriate testing methodologies and predictive models. The findings in retrieval studies are analyzed in the light of the mechanism that can take place under modular hip joint conditions.

Modular hip joint degradation is a complex phenomenon, which involves patient characteristics, implants design and materials. Improving the understanding about what happens inside of the modular joints is required to deal with degradation at all possible levels (patients, surgeons, companies and scientists)

Several degradation mechanisms were proposed in the literature. Unfortunately, they are not supported by clean experimental evidence and in some cases they are even in contradiction with the corrosion state of the art.

As consequence, there is a need for systematic investigations aiming at improving our understanding of these degradation phenomena. Particular interest is on crevice-corrosion and fretting-corrosion, two mechanisms that can occur in hip joints configuration.

This understanding requires developing appropriate testing methodologies as well as predictive models, which gives a theoretical frame to assesses the degradation mechanisms of modular hip joint prostheses.

2

State of the art

To understand modular hip joint implants degradation, the basics of crevice-corrosion and fretting-corrosion will be considered in the following. This chapter presents a theoretical overview of both phenomena where existing models will be described and discussed. Subsequently, relevant properties of biomedical alloys under corrosion and tribocorrosion conditions are also reviewed.

2.1 Crevice-corrosion fundamentals

Crevice-corrosion is a well-known localized degradation mechanism that mainly affects passive metals. In general, this phenomenon takes places in narrowed spaces such as joints, under seals or gaps where oxygen concentration gradients develop within the electrolyte.

Let's assume a cavity (crevice) formed on a planar surface in contact with an electrolyte with dissolved oxygen. Corrosion process takes place and leads to oxygen depletion in the electrode proximity. In the outside part, initial oxygen concentration is re-established by the mass transport but not in the crevice. In consequence, the oxygen depletion in the crevice leads to a loss of passivity and a preferential corrosion with respect to the outside part. Then, an electrochemical cell is formed between the surface that behaves as a cathode and the cavity, which acts as an anode. [46]. This electrochemical cell is known as aeration cell.

2.1.1 Crevice-corrosion generalities

Material dissolution increases the corrosion rate inside of the crevice (anode) which is potential dependent [63]. The current from the passive regions (cathodes) is due to oxygen reduction in acidic media, as reaction 1 shows.



The effect of oxygen concentration in a passive metal can be understood through the Evans diagram shown in Figure 2-1. Passive metals have a characteristic active-passive transition called the passive potential (E_p). Above this value a protective oxide layer is formed, reaction 2, while below this value the material actively corrodes, reaction 3. Note that reaction 2 and 3 imply a transfer of electrons. Thus the reaction rates can be expressed as electrical current density (i).



In the Evans diagram of Figure 2-1, (where the current (I) is plotted as a function of the potential (V)) a simplify anodic polarization curve of a passive metal is plotted together with two cathodic curves representing the oxygen evolution. As observed, the potential at which the cathodic curves, oxygen curves, cross the anodic one is the corrosion potential. At this potential the anodic and cathodic reaction have the same velocity and material dissolution takes place. E_{cor} is the potential spontaneously attained by the metal once immersed in a given solution. This potential determines the corrosion current (I_{cor}).

Curve 1 in Figure 2-1 corresponds to high oxygen concentration while the low concentration is represented by curve 2. The passive material in a high oxygen concentration electrolyte shows a E_{cor1} in the passive domain ($E > E_{pass}$). It means, oxygen availability allows the formation of an oxide layer, see reaction (2). While electrolytes with lower oxygen concentrations lead to a E_{cor2} in the active domain ($E < E_{pass}$). Under this condition, active dissolution of the material takes place (reaction 3). A difference in potential is established between the areas rich in oxygen with respect to the places where it is limited. This potential difference induces a current. Likewise, there is a potential drop due to the resistance of the electrolyte that finds the current. This effect is known as the ohmic drop [46], [64], [65].

Because the charge transfer across the metal-electrolyte interface depends of the reaction rate, which is a function of the potential, this reaction rate can be expressed as current (I).

Coming back to the cavity in the planar surface, Figure 2-2 represents an aeration cell of a passive metal where the difference in the oxygen concentration causes a potential decrease from the surface E_1 to the bottom of the crevice E_2 that becomes active. This figure represents crevice-corrosion process. Crevice area is smaller when compared to

the area of the material that is still passive. Thus, the area effect anode/cathode becomes more relevant and this leads to the main source of current [46], [63]. Then, along the crevice this potential drop establishes an active-passive transition zone [64], [66], [67].

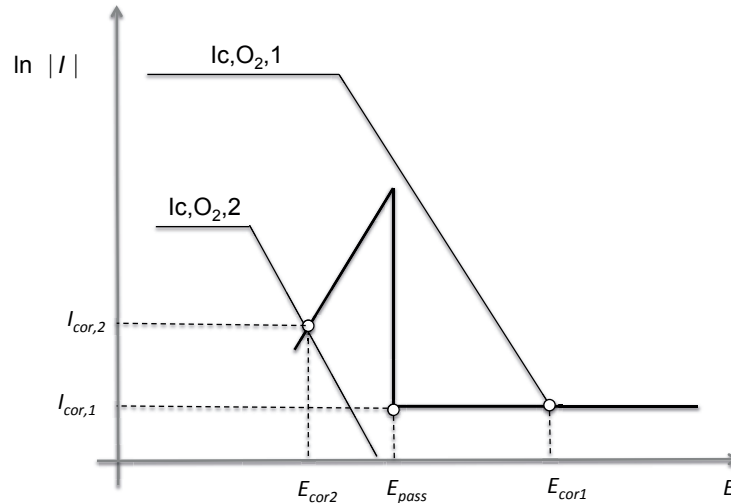


Figure 2-1. Evans diagram of an aeration cell, adapted image [46]

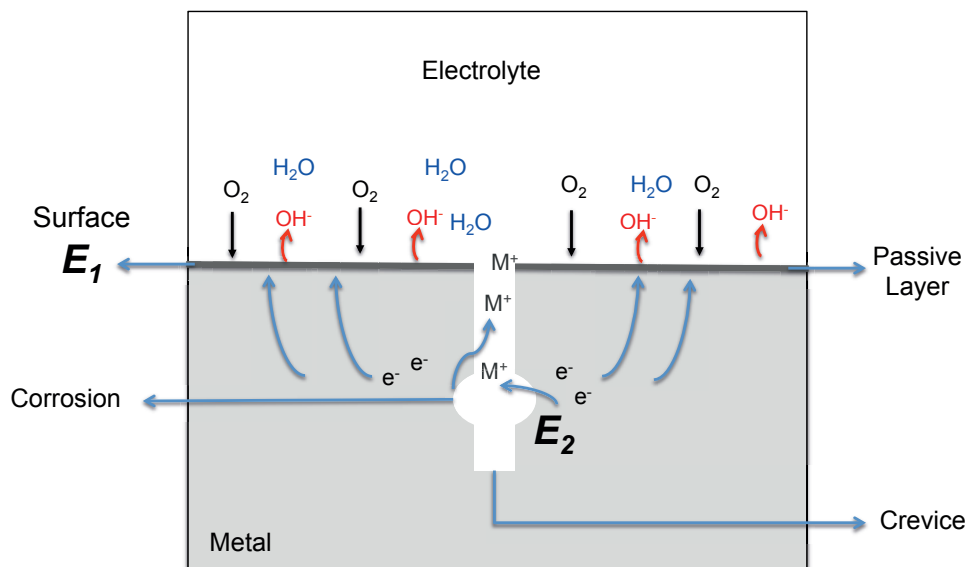


Figure 2-2. Corrosion process in an aeration cell

Under these circumstances, the potential at the external surface as well as in the top of the crevice, corresponds to the imposed potential E_{ap} or to the open circuit potential of the system.

Afterwards, once the depassivation of the crevice has taken place, the potential drop, the acidification of the media as well as the presence in high concentrations of aggressive ions such as Cl^- stabilize the active-passive cell [46], [49], [63], [65], [68].

Geometrical factors play an important role. Klassen et al [69], found that a deeper crevice increases the sensitivity of the system to fail under localized corrosion. Besides, Jackson et al [47] reported several industrial cases where narrower crevices increase crevice-corrosion occurrence.

2.1.2 Crevice-corrosion IR-Voltage Model

Several models have been proposed to predict pH, chloride concentration, potential and current evolution as a function of time, distance or chemical parameters in crevice-corrosion systems [70]–[72]. However, for the modular artificial hip joints case, the IR-Voltage model [73] provides the most appropriate and robust frame for crevice-corrosion understanding.

The IR-Voltage has been developed and presented by Pickering and co-workers in several publications [63], [64], [66]–[68], [73]–[76]. Based on the aeration cell concept, this model takes into account geometrical, chemical and electrochemical parameters to quantitatively determine crevice-corrosion.

The IR-Voltage model proposes that the potential along the crevice (Figure 2-4) can be expressed by equation 4 [77], where the potential at position x is a function of the potential at the top of the crevice E_{ap} , the resistance of the electrolyte (R) and the anodic current (I). This current in turn depends on the distance, the material, the crevice geometry and the resistance of the solutions that change due the acidification of the media, material dissolution and metal complex hydrolysis [64], [67], [68], [77][77][75][18]. The potential $E(x)$ is in between the passive potential (E_{pass}) and the mixed potential between the metal and the H^+ , known as limiting potential (E_{lim}) [67]. This definition from equation 4 allows determining the potential distribution along the crevice, represented in Figure 2-3.

$$E(x) = E_{x=0} - IR_x \quad (4)$$

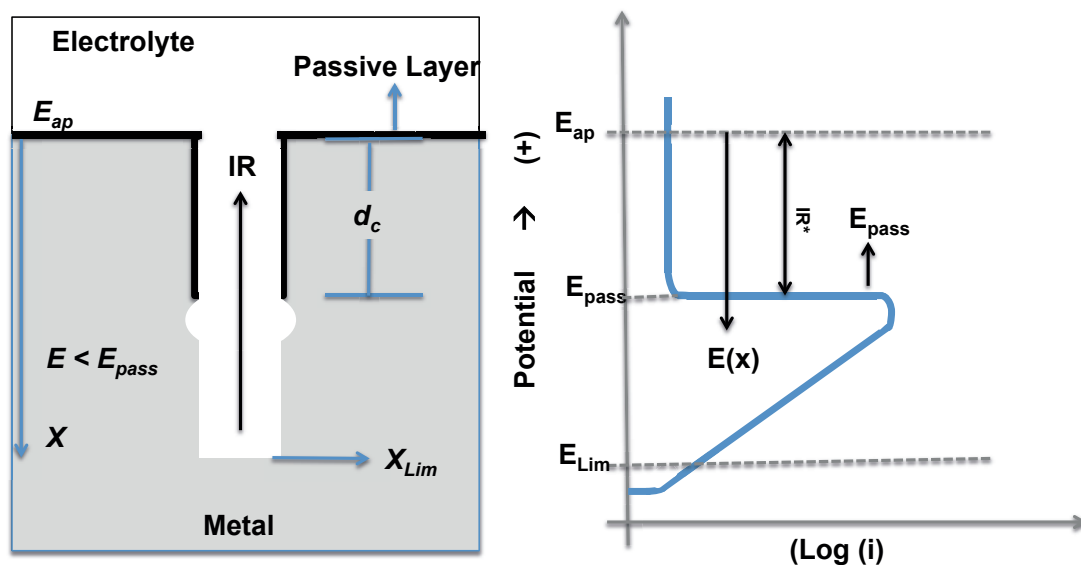


Figure 2-3. Crevice-corrosion cell according to IR-Voltage model, adapted image [64]

The relation between the potential drop and the active-passive cell establishment was defined by the IR criterion. Under this criterion, crevice corrosion takes place if the potential drop inside of the crevice, defined as IR , is higher than the difference between the potential on the surface and the passivation potential, represented as IR^* [73], [76]. See equation 5 and 6.

$$IR > IR^* \quad (5)$$

Where,

$$IR^* = |E_{ap} - E_{pass}| \quad (6)$$

Equation 5 is satisfied at depth d_c (critical distance) in the crevice. In other words, the crevice material below d_c loses passivity and actively corrodes at this rate. This potential drop changes with time due to the evolution of the system, as well as the current and the solution resistance do.

The critical distance d_c can be calculated from equation 7 [67]:

$$d_c = \frac{I - \sqrt{I^2 - 2k\sigma l^2 g i_{pass} |E_{ap} - E_{pass}|}}{k l i_{pass}} \quad (7)$$

Where, I : crevice current (μA); i_{pass} : passivation current density ($\mu A \text{ cm}^{-2}$); E_{pass} : passivation potential (mV); σ : solution conductivity ($\Omega^{-1} \text{ cm}^{-1}$); k : sides wall; l : length (cm); g : gap (cm) and E_{ap} : applied potential (mV).

This model can be applied to calculate d_c in early stages of crevice corrosion as long as some limitations are taken into account [67][77]:

- The data used in the model, such as E_{pass} and i_{pass} , have to be taken from a polarization curve carried out in the same electrolyte as the one used in the system with the crevice configuration.
- To avoid the influence of parallel processes in the cell, homogeneity of the applied potential along the material must be considered.
- Finally, as the chemistry of the electrolyte changes as it was mentioned above, the critical distance varies as well as a function of the time.

Equation 7 can be further simplified. If the ratio between the passivation current density (i_{pass}) and the maximum current density (i_{max}) is lower than 0.05, the contribution of the passive current coming from the crevice walls to the total current is very low and can be neglected [67]. Then, the expression is simplified to:

$$d_c = \frac{|E_{ap} - E_{pass}| * \sigma l g}{I} \quad (8)$$

The IR-Voltage model has been developed for a specific configuration and tested on materials which sensitivity to crevice-corrosion is known. However, unknown aspects about crevice-corrosion degradation mechanism could be elucidated if the applicability of this model can be validated for complex geometries, such as the modular hip joint configurations and for biomedical alloys.

2.2 Crevice-corrosion of biomedical alloys.

The corrosion resistance of Ti and CoCr alloys to corrosion under environmental conditions is widely accepted. However, several works have questioned the integrity of these biomedical alloys under crevice-corrosion condition due to the phenomenological interpretation of surfaces in retrieval implants.

The corrosion resistance of these alloys relies on the homogeneity and integrity of their oxide passive layer, which is formed as soon as the material contacts air, or water. In consequence, corrosion degradation mechanisms take place if the passivity is broken and corrosion is accelerated when the repassivation is not possible.

2.2.1 Biomedical alloys

Ti alloys

As mentioned above, Ti alloys are widely used as biomedical alloys in hip joint implants due to the corrosion resistance, biocompatibility, high strength and lower modulus equivalent to the cortical bone [78].

Currently, profuse literature related to Ti alloys technology can be found, such as surface modification to improve osteointegration, surface films to improve mechanical properties and its limited wear resistances as well as modification on the microstructure.

Ti alloys can be classified according to the crystalline structure at room temperature stabilized by the alloying elements and thermomechanical processing: α , which corresponds to hexagonal closest packed (h.c.p.), near-: α , β that is body cubic centered (b.c.c), metastable- β and ($\alpha + \beta$) where both structures coexist [26], [79]. The corrosion resistance and mechanical properties of Ti alloys are determined by the microstructure.

Several alloys β , metastable β and well as ($\alpha + \beta$) are used in biomedical applications. Some of these alloys are Ti₂₉Nb₁₃Ta_{4.6}Zr, Ti₁₂Mo₆Zr₂Fe (TMZF), Ti₃₅Nb₇Zr-5Ta, Ti-15Mo-5Zr-3Al Ti₆Al₄V, Ti-13Nb-13Zr, Ti₆Al₇Nb and Ti₅Al_{2.5}Fe, the Ti₆Al₄V being the most widely used in hip devices [26], [79], [80]. Its standard composition is reported in Table 2-1 [27]. In general, mechanical properties of β and ($\alpha + \beta$) alloys can be controlled through heat treatments [26].

The spontaneous passivation of this alloy makes it difficult to study the passivation mechanism. However, it is known that the passive oxide layer formed in this alloys consist of TiO₂ and that under anodic polarization this layer grows at a ratio of 2nm/V. In consequence, low passive currents are registered in several acidic solutions at different pH (4×10^{-6} A/cm² to 4×10^{-9} A/cm²). In general, Ti alloys are resistant to oxidizing acids; seawater and neutral solutions but the passive layer is disrupted in presence of fluorides [25].

Table 2-1. Standard chemical composition (%wt) Ti6Al4V alloy [27]

| Al | V | Fe | O | N | C | H | Ti |
|---------|---------|------|------|------|------|-------|---------|
| 5.5-6.5 | 3.5-4.5 | 0.25 | 0.13 | 0.05 | 0.08 | 0.012 | Balance |

Hosseini et al [81] and Brauer and Nann in Kaesche [25] studied the active-passive transition of pure commercial Ti in H₂SO₄ as a function of the concentration. In both cases E_{pass} for high concentrate H₂SO₄ values were from -0.4V to 0V.

CoCr alloys

Wear and mechanical resistance are properties required by hip joint devices, which have been satisfied by CoCr alloys. The composition of CoCr for cast or wrought alloys, i.e. ASTM F75 and F1537 respectively, which are widely used for hip joint implants [80-81], are specified in Table 2-2.

Table 2-2. Standard chemical composition (wt%) of CoCr alloy F75 [82]

| Co | Cr | Mo | W | Ni | Mn | Si | Fe | C | N | P | Al | S |
|-----------|---------|---------|-----|-----|-----|-----|------|------|------|------|-------|------|
| 58.9-69.5 | 27.0-30 | 5.0-7.0 | 0.2 | 2.5 | 1.0 | 1.0 | 0.75 | 0.35 | 0.25 | 0.02 | 0.030 | 0.01 |

The matrix of these alloys corresponds to a Co-rich and the crystalline structure hexagonal closest package. However, this phase becomes a face cubic center structure by heat process transformation. In consequence, both structures coexist at room temperature [83], [84].

The high strength of these alloys is given by the solution hardening and carbide precipitation. However, agglomeration of carbides and large size-grains are found affecting the corrosion resistance, the fatigue life of the alloy and the yield strength of the alloy. Zones poor in chromium, due to its migration and formation of chromium carbides (Cr₂₃C₆), behave as anode while the rest of the material behaves as cathode, generating localized corrosion phenomena. Therefore, either long annealing process are done to dissolve chromium carbides or the biomedical devices are obtained by powder metallurgy, where a powder of the alloy is compress under high pressures and temperature [83]–[85]. Final microstructure has less large size grains and defects, which reduce the yield strength and the fatigue risk [86].

Passive layer formed in CoCr mainly consist in Cr₂O₃ and its thickness growths as a function of potential at a rate of 10nm/V [87], [88]. Even though, active-passive transition of CoCr alloys are not well defined in the literature. It has been demonstrated that CoCr alloys passive behavior is controlled mainly by Cr [87]. In consequence, the active-passive transition of chromium can be a good approximation for CoCr alloys. Kaesche found ([25]) that active-passive transitions of chromium are related to pH, as

the latter increases the transition to more negative potentials. In addition, in presence of acidic solution the oxide layer becomes thinner as long as the potential decrease.

Therefore, crevice-corrosion as degradation mechanism can affect biomedical alloys only if the passivity is broken. In consequence, this section presents several studies (related in Table 2-3) where Ti and CoCr alloys are evaluated under crevice-corrosion conditions in order to elucidate which parameters play a role in the degradation.

2.2.2 Crevice corrosion of biomedical alloys

Crevice corrosion in Ti alloys

Since the 60's, several works have been focused on the behavior of Ti alloys under crevice-corrosion conditions at high temperatures and in concentrated salt solutions.

In the latest 60's, Jackson and Boyd [47] reviewed industrial corrosion cases concerning Ti. At that time, no crevice-corrosion failure was reported at room temperature, while damage at a temperature higher than 100°C in 1 or 2 N NaCl were found at pH values ranging from 5 to 9.

The effect of the pH and temperature on the crevice-corrosion degradation of Ti alloys was studied by Pariona et al [48] and Griess [49], respectively.

Pariona et al [48] determined that Ti alloys evaluated in a range of pH from 0.87 to 6.72, present the highest current densities ($10^3 \mu\text{A}$) and material dissolution were reported for Titanium in 1M NaCl solution at pH 1 or lower at 100°C. In this study, crevice-corrosion configuration were reproduced for electrochemical test by the fixation of Ti screws in a non-conductive surface and for immersion test, a sandwich structure made of Ti and a no-conductive material plates.

On the other hand, the effect of temperature was studied by Griess [49] using electrochemical polarization test. Those experiments were conducted in a range of 150°C to 200°C in 0.9% NaCl-0.1M HCl. To reproduce the crevice geometry, two Ti plates were joined with a screw. Even though crevice corrosion did not occur in all the samples, more severe attacks were registered at higher temperatures.

Likewise, Abdulsalam [65] reported highest crevice corrosion occurrence where the potential drop in the crevice in systems with high concentration of chlorides (1.5%HCl+19%NaCl and 25%NaCl) in a range of temperatures from 80°C and 100°C. Crevice geometry was made using two nuts fixed into a bolt, the system was immersed in the solutions while the evolution of potential and current was registered. Ti samples were also evaluated in a solution with lower concentration of chlorides (1.5%HCl) at 80°C. For this case, no ohmic drop occurred inside of the crevice and as a consequence no crevice-corrosion damage was found.

The effect of sulphates has been also studied. Vicentini et al [89] evaluated the minimum sulphuric acid concentration needed at 40° C, to generate crevice-corrosion degradation of a rod made of Ti covered by a shield and connected to another Ti rod uncovered. They found a critical concentration around 0.5M H₂SO₄ to reproduce crevice in the shielded part that behaves as an anode.

Similarly, Rajendra et al [90] evaluated also the effect of solution composition in Ti at high temperature ($>100^{\circ}\text{C}$) in a crevice-corrosion configuration, which consisted of a sandwich structure where the sample was placed between two sheets made of acrylic resin. The study confirm that exposing pure Ti to solutions that contain halide ions or sulphates favor crevice-corrosion damage. A decrease in the potential was registered for Ti in the crevice corrosion configuration, however, there is no information about the quantification of the damage, neither about the distance were it was found.

In addition, Chenghao et al [91] published in 2015 a work where Ti6Al4V was evaluated under crevice corrosion condition in Ringer's artificial body fluid. No crevice-corrosion degradation was found but homogeneous corrosion was reported which is a contradictory finding according to the passive behavior of this alloy.

In general, studies at high temperature, where Ti alloys are more sensitive to crevice-corrosion conditions, low pH and medium concentration of Cl^- were insufficient to provoke damage, if the aeration cell was not formed and in consequence there was no potential drop [48], [49], [65], [92], [93]. Crevice-corrosion attacks were registered only in systems at high temperature.

Numerical analysis about results from crevice corrosion experiments was done by Heppner et al [93]. Through modeling, they found the influence of the solution pH and conductivity on the degradation due to crevice-corrosion. Likewise, the high influence of the hydrogen reduction was found from the analysis of the data specially, in the potential drop for Ti immersed in 0.5M NaCl at 70°C .

According to the crevice-corrosion studies mentioned above, it is expected that crevice-corrosion does not occur in the hip joint configurations due to the fact that temperatures are lower compared to the systems reviewed in this chapter. However, the evolution of the electrochemical behavior of Ti alloys in experiments carried out at longer times (maximum duration was 10 days) or at potentials outside the passive region have not been reported. Then, it is uncertain if some changes in the electrochemical behavior can occur under those conditions and derivate in a disruption of the passive layer.

Crevice corrosion in CoCr alloys

The use of CoCr alloys in several fields led to the study of their crevice corrosion resistance since the 70's. In a review published by Kuhn [94], some contradictions were found among the different results which brought as conclusion that CoCr resistance to crevice-corrosion is associated to its chemical composition. The presence of Ni makes this alloy prone to crevice-corrosion, while contents of Mo ($>5\%$) in presence of Cr ($\approx 20\%$) increase the material resistance.

Wrought and cast CoCr alloys were evaluated by Devine et al [95] under crevice corrosion as well as stainless steel 316L (SS) in deareated 10% HCl - 1% FeCl_3 at 37°C . Mild to severe crevice-corrosion damage was reported for cast CoCr alloys, and 316L SS while no damage was found on samples made of wrought CoCr.

In the same year, Levine and Staehle [96] published a study focused on crevice-corrosion degradation of biomedical alloys. The crevice-corrosion configuration

consisted of two metallic blocks separated by a crevice of 0.5 mm. Experiments using CoCr alloys and Ti6Al4V were carried out in Ringer solutions at 37 °C. Results from those tests demonstrated the stability of the potential registered for both alloys. Some experiments were performed for CoCr/316LSS and CoCr/Ti6Al4V couples. Results showed low current values ($>1 \times 10^{-6}$) and fluctuations on the potential. However, once the contacts were opened after 30 days only pitting was found on the stainless steel.

More recently, in 2002 Reclaru et al [97] published a work where CoCr alloy samples were coupled with stainless steel, in order to check if galvanic coupling or crevice corrosion occurred. In both cases the conclusion was that CoCr alloy did not suffer crevice-corrosion and/or galvanic corrosion.

Finally, Goldberg et al [98] evaluated couples of CoCr/CoCr, CoCr/Ti6Al4V and Ti6Al4V/Ti6Al4V on a simulator (under static and dynamic conditions) and fretting test looking for crevice-corrosion evidence. Current, OCP, Cl⁻, O₂ and pH were measured during the test. No significant evidence of crevice-corrosion was found in CoCr/CoCr and Ti6Al4V/Ti6Al4V samples in all tests. Results from CoCr/Ti6Al4V couple showed a slight decrease in oxygen concentration and pH and an increase in the Cl⁻ concentration with time (80h). However, no changes in current or potential (inside of the crevice) were observed once the loading was stopped and no evidence of damage of the material surfaces was reported.

In addition, despite the studies where biomedical alloys did not suffer damage in simulated body solutions at room temperature [96], some contradictions are found contrasting those results with studies where CoCr alloy samples deterioration was reported [95], [98]. Unfortunately, those works did not register potential drops or significant current changes to be analyzed, neither the phenomenological evidence about the failure.

Few studies controlled important parameters such as the crevice gap or performed the tests changing the electrochemical conditions, which is extremely important due to the uncertainty about the active-passive transition of these alloys. In consequence, a systematic study of crevice-corrosion focused on hip joint implants and able to control geometrical and electrochemical conditions is required. In parallel, careful experimental methodologies need to be developed in order to control electrochemical and geometrical conditions as well as to measure characterizable variables of the system and their evolution at long exposure times.

Nowadays theoretical tools to predict corrosion, adapted and applied to hip joint configurations are needed. They must be able to take into account geometrical and electrochemical conditions to clarify the degradation phenomena of modular hip joint implants.

Table 2-3. Bibliography about crevice-corrosion studies in Ti6Al4V and CoCr alloys

| Authors | Biomaterial tested | Conditions | | Observation |
|---------------------------------------|--|---------------------|---|--|
| | | Temperature (°C) | Solution | |
| Griess (1968) | Ti | 150° to 200°C | 0.9% NaCl-0.1MHCl pH: 3 | <ul style="list-style-type: none"> • Crevice corrosion was registered in half of the samples. • Attacks were more severe at higher temperatures. |
| Vicentini, Sinigaglia, Taccani (1975) | Ti | 40°C | H ₂ SO ₄ 0.2M,0.5M,1M,2M pH: Unspecified | <ul style="list-style-type: none"> • Crevice-corrosion was reported. |
| Devine and Wulff (1977) | Wrought CoCr, Cast CoCr and Stainless steel 316L | 37 °C | 0.9% NaCl pH: Unspecified | <ul style="list-style-type: none"> • No crevice-corrosion occur in wrought CoCrMo • Mild crevice – corrosion was found in cast CoCr alloy • Severe crevice-corrosion was reported for 316L SS |
| Levine and Staehle (1977) | 316L, Ti, Ti6Al4V, CoCr (Stellite 25) | 37°C | Ringer's solution, pH: 7.2-7.4 | <ul style="list-style-type: none"> • No crevice-corrosion attack on Ti, Ti6Al4V and CoCr. |
| Sury and Semlitsch in Kuhn (1981) | Wrought CoNiCrMoTi, Cast CrCoMo | Room temperature | 10% FeCl ₃ | <ul style="list-style-type: none"> • Slight crevice-corrosion was reported in Cast CrCoMo |
| Satoh, Shimogori and Kamikubo (1987) | Ti, Ti-0.3Mo-0.8Ni, Ti-0.1 5Pd | 100 °C | <ul style="list-style-type: none"> • 20%NaCl, pH:4-6 • 42%MgCl, pH: Unspecified | <ul style="list-style-type: none"> • Severe crevice-corrosion occurred in Ti samples without Pd |

| | | | | |
|---|-------------------------------------|--------------------------|---|---|
| Pariona, Müller (1997) | Ti | 50°C, 70°C, 90°C, 100 °C | <ul style="list-style-type: none"> • NaCl 1M, pH: 0.87 - 6.72 • Na2SO, pH: 6.72 | <ul style="list-style-type: none"> • Crevice – corrosion was found at 100°C in OCP. |
| Akashi, Nakayama, and Fukuda (1998) | Ti (Ti-Gr. I), Ti alloy (Ti-Gr. 12) | 60°C, 70°C, 80°C, 90 °C | NaCl (10-10 x 10 ⁵ ppm) pH: 7 | <ul style="list-style-type: none"> • Crevice corrosion occurred at 90°C under 0.3V. • A potential drop was registered to initiate crevice-corrosion. • There is not description about the severity of the damage |
| Abdulsalam (2007) | Ti | 100 °C | 25%NaCl pH: 4.7 | <ul style="list-style-type: none"> • A significant ohmic drop was reported for pieces that suffered crevice-corrosion. |
| Rajendran and Nishimura (2007) | Ti, Ti15Mo | 100 °C | 10%NaCl pH: 1-3, 5. | <ul style="list-style-type: none"> • Crevice – corrosion was reported at 100°C. • Ohmic drop was registered in the crevice configuration. • There is not description about the severity of the damage |
| Chenghao, Li'nan, Chuanjun, Naibao, (2015) | CP Ti, Ti-6Al-4V, and Ti-Ni SMA | 100 °C | Ringer's solution pH: 7.4 | <ul style="list-style-type: none"> • Crevice current values for CP Ti and Ti6Al4V are almost zero during all the experiment. • No crevice-corrosion was reported. |
| Reclaru, Lurf, Eschler, Blatter, and Meyer (2002) | REX734 stainless steel and CoCr | 37 °C | 9g/l NaCl pH: 5.7 | No crevice-corrosion was found in CoCr samples. |

2.3 Fretting Corrosion wear

2.3.1 Definition and generalities

Fretting corrosion is a material degradation phenomenon caused by reciprocating motions of small amplitude combined to a corrosive attack by the surrounding electrolyte. As a main characteristic, the contact size is larger than the amplitude of the movement [99]–[103].

As already pointed out in chapter 1, fretting-corrosion phenomenon is an important issue in medicine. Wear can be accelerated by the chemical degradation of the material leading to the loss of asepsis and causing adverse reactions in the surrounding tissue [24], [62], [98], [100], [104]–[106].

Two materials in a tribological contact, under load and relative movement, in presence of an electrolyte are subjected to mechanical and chemical wear. The mechanical wear corresponds to the material removed by the mechanical action while the chemical wear is the material removed by the corrosion under tribological conditions [107]. Then, the damage caused by fretting-corrosion is affected by the normal load, frequency, amplitude displacement, the rigidity of the system, the electrolyte and the prevailing electrochemical conditions [43], [108]–[110].

Figure 2-4 shows fretting loops, which correspond to a representation of the tangential force (F_T , N) vs. amplitude displacement (D_x , μm), where the slope corresponds to the compliance of the contact [58], [110]. Those diagrams allow following the evolution of the elastic and plastic accommodation of the system over time. Under fretting-corrosion, three mechanical regimes can take place: Stick, partial slip and gross slip. Each regime is associated to a mode of surface damage:

Figure 2-4a corresponds to the stick regime, which occurs at lower amplitude displacements. Under this regime the tangential force produced during the movement is equal to normal force (F_N) times the coefficient of friction (COF). In other words, stresses produced by the small displacement are accommodated by the elastic deformation on the contact, so low or negligible wear occurs. Figure 2-4b represents the partial slip, which occurs at higher displacements compared to the previous regime. In this case, the normal load times COF is higher than the tangential force. Therefore, under this condition stick regime usually occurs at the center of the contact while in the extremes slip takes place. Wear and corrosion occurs in a low proportion, damage is mainly attributed to crack growth and fretting fatigue. Materials under stick or partial slip can be affected by fretting fatigue. Finally, the third regime corresponds to gross slip Figure 2-4c, which occurs under high displacements where the tangential force is higher than the product of COF and F_N . Thus, the slip at the interface distributes or accommodates plastically the stresses in the

contact area. A significant amount of material is worn under this regime by the effect of wear and corrosion; especially for passive alloys where besides wear, passivation and depassivation processes take place. When the material is worn, the passive metal is removed, then fresh material contacts the environment and oxidizes. This combined process between wear and corrosion increases the wear rate [57], [111]–[113].

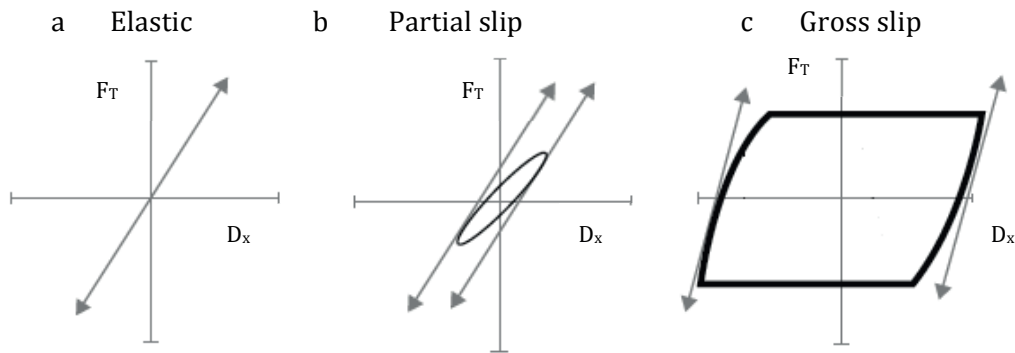


Figure 2-4. Regimes as a function of displacement amplitude and tangential force a) stick, b) partial slip and c) gross slip, adapted image [113]

Barril et al [58] carried out fretting tests in dry and in wet conditions (under cathodic and anodic potentials) on a Ti alloy. The tests were done to analyse the influence of the electrochemical parameters on the fretting behavior of the material. This study revealed that higher wear volumes were obtained under anodic conditions, when the material is passive. Thus, material is worn while passivation and depassivation processes are taking place. In this case, metallic and oxidized particles are generated because of the tribocorrosion action. Deformation due to stresses and chemical reaction transform those particles in a tribofilm which gets trapped in the contact area [44], [61], [100], [114]. This tribofilm may be lubricant or abrasive according to the conditions of the system [104]. Then, as it was mentioned before, these tribofilms behave as a third body, which in turn is exposed to mechanical deformation and chemical reaction. In addition, this layer modifies the velocity between the bodies in contact and also affects the distribution of the force thus the wear rate, among others. Consequently, the way to address the study of the fretting corrosion phenomena is through the third body concept.

2.3.2 Two body models

The first fretting model was proposed in 1954 by Uhlig [115], equation (9). In this model, total wear depends of: Firstly, the chemical wear corresponding to the first two terms related to the weigh lost by removing the oxide layer which is rebuild due to the chemical action. Secondly, mechanical wear, that corresponds to the third term, which is the weight

lost because of the ploughing action. Uhlig's model depends on number of cycles (C), frequency (f), amplitude of displacement (l) and normal load (F_N) [115].

$$V_T = (k_0 l F_N^{1/2} - k_1 F_N) \frac{C}{f} + k_2 l F_N C \quad (9)$$

Later, in several works carried out by Mischler et al. [58], [61], [62], [114], [116], [117] a similar Uhlig's concept was followed. For tribocorrosion systems in absence of a third body, a mechanistic approach describing the total wear volume as the addition of the mechanical (V_{mech}) and chemical (V_{chem}) wear (equation 10) was proposed [118].

$$V_T = V_{chem} + V_{mec} \quad (10)$$

For this mechanistic approach, mechanical wear is related to the material removed by mechanical action. V_{mech} follows Archard's law (equation 11) and it can not be directly measured through experiments [99].

$$V_{mech} = K_1 v_s \frac{F_N}{H} \quad (11)$$

Here, V_{mech} is proportional to the sliding velocity v_s, the normal force F_N and inversely proportional to the hardness H. The wear constant is defined as K₁.

Chemical wear is defined as the material lost by wear-accelerated corrosion; it takes into account material removed from the passive layer and from the substrate. A passive metal under tribochemical conditions, suffers a material loss by the mechanical action but also a material loss caused by the depassivation processes. When the mechanical action removes the passive layer, the underlying metal in contact with the environment repassivates. Under this context, wear induced depassivation and repassivation processes together with the corrosion outside the area of contact increase the material loss [117]. The material volume loss by the chemical action is calculated through Faraday's law as shown in equation 12, where, M corresponds to the atomic mass of metal, n is the oxidation number of the metal, F is Faraday's constant and ρ is the metal density. In tribochemical systems, I corresponds to the anodic current registered during rubbing [114].

$$V_{chem} = \frac{IM}{nF\rho} \quad (12)$$

This approach have been developed in several works [99], [114], [117], [119]–[122]. In those works, the dependence of the wear rate and the coefficient of friction on the applied potential (cathodic and anodic) has been proved. Under anodic conditions, wear rate increased and a thick third body was generated when compared to the cathodic conditions, in which the particle detachment was lower thus the third body film was thinner.

Cao et al [121], [122] proposed a tribocorrosion model including the lubrication phenomenon which was successfully applied to tribochemical degradation in the sliding system found in hip joint implants, specifically in the acetabular cup/femoral head junction. This model considered lubrication effects in the joint; wear accelerated corrosion and mechanical wear caused by the plastic deformation of the asperities. Then, the total

wear is calculated by expression (13) where lubricant properties like viscosity of solution (η) and density (ρ) are considered. Mechanical parameters as the effective radius of curvature (R'), Young's modulus and effective Young's modulus (E and E' , respectively), harness (H) are used. k_{mech} and k_{chem} represent mechanical and chemical wear rate, respectively. While considering that these processes affect passive metals, this estimation considered the electrochemical effect on the passivation and depassivation process under sliding conditions in the terms of (Q_p) passivation charge density, atomic mass, oxidation valence (n) and Faraday constant (F).

$$V_T = k_{mech} \frac{(E)^{0.6556}}{n^{0.9685}} \cdot \frac{(F_n)^{1.3129} (v_s)^{0.0315}}{(R')^{1.1473} H} + k_{chem} \frac{MQP(E')^{0.3278}}{nF\rho\eta^{0.4843}} \cdot \frac{(F_n)^{0.6565} (v_s)^{0.5158}}{(R')^{0.5737} H^{0.5}} \quad (13)$$

2.3.3 Third body models

A mechanistic approach for tribocorrosion systems in presence of a third body layer was proposed by the model of Guadalupe et al [62]. This model was developed for third bodies produced under sliding conditions at high temperature pressurized water.

The material affected by wear and wear-accelerated corrosion is based on mass balances. The system is defined in terms of compartments, which represents the bulk material, the third body and the material worn from the contact.

Four compartments were defined: Firstly, C1 is material from the substrate, which consist of material from the bulk and the oxidized material from passive layer. The material removed from this compartment by wear and wear accelerated corrosion feeds the third body. Subsequently, this layer is made of compartment C2 and compartment C3. C2 represents the oxidized material in the third body, which is feed from the substrate and from the metallic material in the friction film becoming oxide due to the contact with the electrolyte. From this compartment the material is ejected to the electrolyte. Likewise, compartment C3 is the metallic material that came from C1 and got trapped in the contact. As mentioned before this layer is exposed as well to mechanical and electrochemical action. As a consequence this layer is corroded, deformed and worn. So, at initial states it is considered a dynamic system that reaches after a while the steady state. Finally, C4 corresponds to material ejected from the friction film to the liquid media, those particles in the electrolyte can be redeposited and integrated to the third body layer, see Figure 2-5.

Guadalupe et al [62] also proposed, mass balances for each compartment as described in equations (14) to (17). The mass (M_x) is defined as a function of time (t) and it is correlated through the material flows described in equation 18 to 21. These material flows are the dynamic path through which the material go from the base material to the third body and from there to the electrolyte.

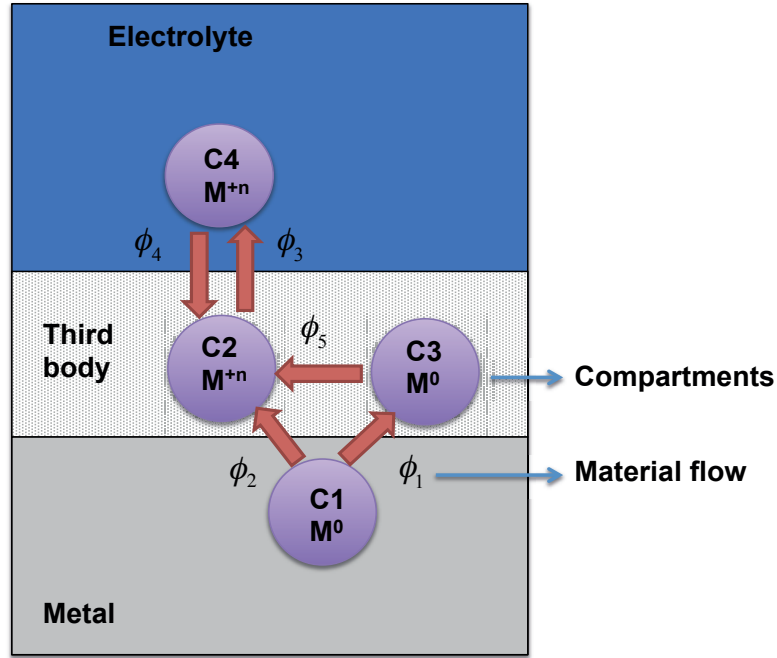


Figure 2-5. Material compartments and material flows relation of a system under tribocorrosion conditions where a third body layer is formed experimentally under in high temperature pressurized water, adapted image [62].

$$M_1(t) = -t(\phi_1 + \phi_2) \quad (14)$$

$$M_2(t) = \left(t + \frac{-1+e^{-tK\phi_5}}{K\phi_5} \right) \phi_1 + t\phi_2 + \left(\frac{-1+e^{-tK\phi_4}}{K\phi_4} \right) \phi_3 \quad (15)$$

$$M_3(t) = \frac{(1-e^{-tK\phi_5})\phi_1}{K\phi_5} \quad (16)$$

$$M_4(t) = \frac{(1-e^{-tK\phi_4})\phi_3}{K\phi_4} \quad (17)$$

Those material flows are related to the third body formation. Equation (18) describes the first flow ϕ_1 , which corresponds to the metal being detached from the substrate according to Archard's law. Secondly, the oxidized particles from the substrate feeding the third body are the second flow ϕ_2 in equation (19) that in turn, follows a wear-accelerated corrosion expression. In addition, equation (20) defines the third flow ϕ_3 , which corresponds to the material ejected from the friction film. Finally, flows related to re-deposition ϕ_4 in equation (21) and to the oxidation of metallic material ϕ_5 inside the FF, described by equation (22) are considered as well [62].

$$\phi_1 = K_{\phi_1} \cdot \rho_{metal} \cdot a \cdot F_N \cdot v_s \cdot \frac{1}{H} \quad (18)$$

$$\phi_2 = K_{\phi_2} \cdot \frac{M_{mol}}{n \cdot F} \cdot v_s \cdot Q_p \cdot \left(\frac{F_N}{H}\right)^{0.5} \quad (19)$$

$$\phi_3 = K_{\phi_3} \cdot \rho_{oxide} \cdot F_N \cdot v_s \cdot r_{ox} \quad (20)$$

$$\phi_4 = K_{\phi_4} \cdot |M^o|_4 \quad (21)$$

$$\phi_5 = K_{\phi_5} \cdot |M^o|_3 \quad (22)$$

Consecutively, flows are described in terms of [62]: normal force (F_N); sliding velocity (v_s); micro-surface hardness (H); oxidation valence (n); passivation charge density (Q_p); Faraday constant (F); atomic mass (M_{mol}); stoichiometric ratio metal/ oxide, r_{ox} ; metal concentration in the electrolyte IM^oI_4 ; metal concentration in friction film IM^oI_3 as well as metal and oxide density (ρ_{metal} and ρ_{oxide} , respectively); K_{ϕ_1} and $K_{\phi_{13}}$ as wear coefficients; and K_{ϕ_2} , K_{ϕ_4} and $K_{\phi_{15}}$, which are proportionality constants. Finally, the attenuation factor (a) is considered as well in this work, as the possible lubricating or abrasive influence of the friction film on the tribochemical response of the system.

This model provided the basis for mathematically quantifying the wear volume under sliding conditions in presence of a third body layer.

2.3.4 Third body In-Vitro evidence. Observations

A fretting corrosion test was done to evaluate the tribochemical behaviour of Ti6Al4V/Al₂O₃ couple used in hip joint modular implants. Observations about wear tracks revealed a third body layer similar to those found in retrieval implants Figure 2-6 [58]. The used parameters, wear rate, current, coefficient of friction among other results are complete and well described.

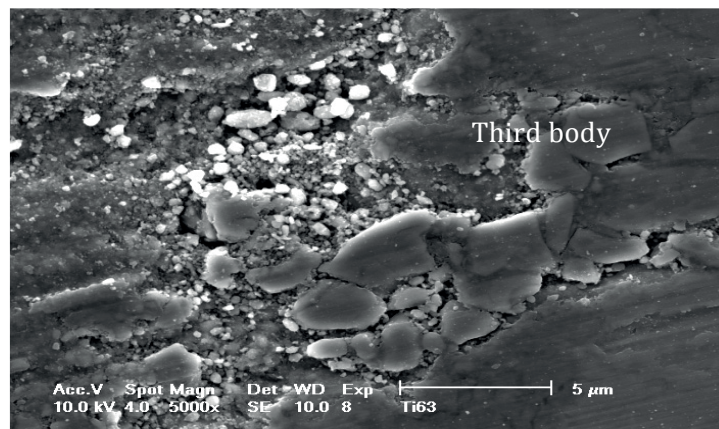


Figure 2-6. Third body layer from In-Vitro Test from a ball on flat configuration system. Conditions: Ti6Al4V /Al₂O₃ , adapted image [58].

Barril et al [57], [58] found the influence of critical electrochemical and mechanical parameters on the wear rate under fretting-corrosion, which means on the third body evolution. For the described Ti6Al4V/Al₂O₃ couple, potential, frequency, load, amplitude and stiffness influence were evaluated through the response of the system in terms of wear volumes, current and friction coefficient.

Clearly, Barrill et al [57], [58] found a strong effect of the electrochemical conditions on wear volume. Several tests were done with different potential, load, oscillation frequency, and displacement. Degradation was higher when load, sliding velocity and oscillation frequency was increased while the system was under anodic potential and gross slip regime. In turn, this degradation corresponds to higher currents registered during the test.

2.3.5 Ti6Al4V and CoCr under fretting corrosion tests

Tribochemical effects on passive metals correspond directly to the wear of oxidized and fresh material. Furthermore, intrinsic mechanical and chemical material properties affect the degradation response.

Material performance can be measured through total wear. Electrochemical answer can be monitored through the evolution of the OCP and current, while the mechanical response from the elastic accommodation and effective displacement observed in fretting loops.

As a passive material, under fretting corrosion condition, there is a drop in the open circuit potential once the movement starts as a consequence of material depassivation. This behavior is reported in works as the Baxmann et al [123] study, where samples of Ti6Al4V were evaluated under fretting conditions at frequency of 1Hz, several normal loads (25N, 50N, 100N and 250N) and displacements (10 μm, 25 μm and 50 μm). Gross slip and significant wear was observed from 50 μm for any load.

Similarly, increments in currents are registered once the movement started, which is the case of the Ti6Al4V/Al₂O₃ couple evaluated by Hiromoto et al [124], to understand the influence of collagen and albumin on the fretting-corrosion performance. Conditions imposed were: normal load of 10 or 30N were applied, at frequency of 1Hz, amplitude displacement of 100 μm and applied potential of -1V and 0.5V. They found none effect of the albumin and small effect of the collagen on the mechanical and tribochemical answer. Wear-accelerated corrosion was attributed mainly to the potential applied and the normal load.

Diomidis et al [125] evaluated several β Ti alloys under fretting condition at normal load of 10N, amplitude displacement of 100 μm, frequency of 1Hz, at 2V vs MSE in Hank's balance solution with additions of bovine serum albumin, hyaluronic acid sodium salt from streptococcus and dipalmitoylphosphatidylcholine. In general, the predominant regime was gross slip. During a 3600s, wear volume registered was between $1,2 \times 10^{-3}$ and $1,9 \times 10^{-3}$ mm³. They found through the OCP and current evolution that repassivation

phenomena are a function of the alloy composition. In this case they did not find a significant effect of the additives on the electrochemical behavior, but the major influence was on the mechanical wear.

Swaminathan et al [106] carried out fretting corrosion test in Ti6Al4V/Ti6Al4V in phosphate buffered saline solution. Loads from 0.5 N to 50N were applied, frequency of 1.25 Hz and amplitude of 50 μ m. Potentials were applied according to the couple and for Ti6Al4V/Ti6Al4V it was -100mV. Increments in current were registered until values of 20N-30 (166 MPa). From this point a change in the fretting regime was registered as it was reported in several works cited above [57], [58], [123], [126].

Studies of fretting corrosion of CoCr alloys are scarcer compared to Ti alloys. Concerning the fretting corrosion behavior of CoCr/CoCr couples, Swaminathan et al [106] found currents which reached 1.2 mA/cm² at -100mV. Even though there was also a current drop, this occurred at higher contact pressures, so the fretting regimes change. It means that gross slip regime remained until 650 MPa of contact pressure.

Ocran et al [127] carried out fretting-corrosion experiments in a pin-on-disc equipment for CoCr/CoCr couple at OCP. Normal load applied was 330N, frequency 2 Hz and a wear path of 1mm. Results were compared with dry condition. A decreasing in the wear and third body layer were observed. However, in this study electrochemical behavior is not described for experiments carried out in liquid.

In all cited studies for Ti alloys, friction films were observed in the wear track. Tribochemical experiments have been used to model the third body phenomena and for analyzing electrochemical effects on the degradation based on this approach.

3 Objectives and strategy

As was discussed previously in the introduction, several degradation mechanisms have been proposed to explain those findings without reaching a general consensus about all of them. Deterioration mechanisms proposed include: pitting, hydrogen embrittlement, galvanic coupling, crevice-corrosion, and fretting corrosion, with the latter being the most widely accepted as the main cause. In consequence, considering the available information in the literature about the role that each of these degradation mechanisms plays in the modular hip joint implants, it can be concluded:

- For hydrogen embrittlement or pitting-corrosion no evidence has been found of their occurrence in modular hip joint configurations in In-Vitro scale. Furthermore, it is unlikely that the specific electrochemical conditions required for those mechanisms to take place are fulfilled in modular hip joint implants.
- In addition, the electrochemical characteristics inside the body are not still well understood, which limits the comprehension of the role that mechanisms such as galvanic coupling plays. However, to explain the main findings in retrieval implants, this lack of knowledge can be overcome by the fact that metallic ions in the blood and tribofilms have been found also in configurations where the femoral neck is ceramic.
- Several hypotheses about crevice-corrosion occurrence in modular implants configuration are not yet clear. Even though the geometrical configuration of modular implants fit the conditions for crevice-corrosion, several studies carried out using biomedical alloys have found that crevice-corrosion occurs only under high temperature conditions (for Ti) or high concentration of halides. Following this reasoning, it is questionable whether that aeration cells can be established for biomedical alloys under modular configurations. Finally, according to the specific geometrical and electrochemical conditions needed for crevice-corrosion to take place, a systematic study on modular hip joints that evaluates several chemical and electrochemical situations under a well controlled geometry is required.
- As mentioned earlier, fretting-corrosion mechanism is known to occur in tribological contact exposed to a corrosive solution such as body fluids under chemical and mechanical conditions. However, the effect of the parameters involved in the degradation caused by this phenomenon is not completely

understood. The elucidation of the key parameters to predict wear rates contribute to the understanding of modular hip joint implants degradation.

- Finally, theoretical approaches to be used as a prediction tool for degradation occurrence (in this case the crevice-corrosion) are needed.

3.1 Goal

The main goal of this work is to assess the degradation mechanism responsible for Trunnionosis through a systematic approach. The focus will be on the two most probable causes namely fretting-corrosion and crevice-corrosion. In addition, this study addresses the parameters that influence the tribofilm build up which constitute the main evidence found in modular hip joint degradation.

To meet the proposed goals, this work splits in two research focus: i) crevice-corrosion occurrence in modular hip joint implants configuration and ii) fretting-corrosion and the parameters interfering in the third body build up.

i) Crevice-corrosion approach

The crevice-corrosion study aims at assessing the occurrence risk of this degradation mechanism in modular hip joints. For this, following tasks are performed.

- To design a system that allows evaluation of several chemical and electrochemical conditions in a configuration imitating the geometrical configuration on the femoral head/neck junction.
- To determine experimentally under which conditions, such as pH and potential, crevice-corrosion can occur in modular hip joint implants configuration.
- To validate the applicability of the IR-Voltage model to crevice-corrosion in modular hip joint implants configurations.

ii) Fretting-corrosion approach

- This fretting-corrosion investigation aims at developing for the first time a predictive model for characterizing fretting-corrosion wear based on the concept of the third body in hip joints through the understanding of specific chemical and mechanical degradation phenomena and relevant parameters. For this, the work will be organized around the following axes:
- To obtain third body layers under different electrochemical conditions in order to characterized their properties.
- To propose a physical model to explain third body build up in order to explain degradation under fretting-corrosion conditions.
- To determine the mechanical compliance effect of the third body on the system.
- To integrate the main electrochemical and mechanical parameters in the development of a model to explain fretting-corrosion degradation.

4 Crevice-corrosion

Previous studies lack of a clear explanation on whether or not crevice-corrosion phenomenon occurs in hip joint implants. In particular, questions have been raised about susceptibility of the specific geometry of modular implants to crevice-corrosion as well as electrochemical and chemical conditions that have to be satisfied for crevice-corrosion to occur. Furthermore, the use of existing theoretical tools to predict crevice-corrosion can contribute to clarify the possible degradation of modular hip joint under this phenomenon.

As a consequence, in this chapter an experimental approach is proposed to clarify under which geometrical, electrochemical and chemical conditions, crevice-corrosion can take place in modular hip joint implants configuration.

4.1 Crevice-corrosion experiments

To evaluate the electrochemical and chemical conditions required for crevice-corrosion to occur, a geometrical configuration was designed to mimic a femoral head/neck junction, where the femoral head is made of a ceramic and the femoral neck is made of Ti6Al4V or CoCr alloy. The configuration offers the advantage of having one non-reactive material in the crevice, which means that the electrochemical signals obtained from the trunnion can be isolated to understand their origin.

Samples with this configuration were evaluated under several electrode potentials and two different solution conductivities. After the experiments, surfaces were examined for evidences of crevice-corrosion.

The experimental set-up is composed of: i) metallic and ceramic samples; ii) the electrochemical cell to control and measure the electrochemical evolution of the system; iii) the electrical assembly and iv) data acquisition adapted to this configuration.

All samples to mimic femoral head/neck, were produced by *Atelier de l'Institut des matériaux* at EPFL.

4.1.1 Materials

To produce trunnion and head samples, real femoral neck and head were characterized. From the real trunnion (also called taper), characteristics such as diameter, length and surface topography were measured (See Table 4-1). A surface thread was done in the taper Table 4-2 shows. From this pattern, peaks, valleys and the amplitude between the peaks were measured and presented in Table 4-1.

Taper samples were made as similar as possible to the real trunnion part. Materials used to make the taper samples were Ti6Al4V and CoCr low carbon alloys.

Small differences were found between the thread made in the sample compared to what was measured in the real trunnion. This may correspond to the tolerances of the machining process. However, these differences should not affect the results of the test. Table 4-1 presents the average of 5 measurements of Rc (Mean height of profile elements) and Rq (Root mean square deviation) values. Amplitude between the peaks of the thread was also measured. This surface characterization was performed using a Laser Scanning Confocal Microscope, Keyence VK-X200 Series 3D. Data analysis was done through the software MultiFileAnalyzer 1.3.0.115. Besides, profile measurements were done with a profilometer UBM Messtechnik, GMBH

Table 4-1. Dimensions and thread profile on trunnion surfaces

| Material/ | Length (mm) | Initial diameter (mm) | Rc (μm) | Rq (μm) | Amplitude (μm) |
|------------|-------------|-----------------------|----------------------|----------------------|-----------------------------|
| Real Taper | 13 | 12 | 29 | 5.7 | 215 \pm 10 |
| Sample | 13 | 12 | 20 | 4.6 | 265 \pm 10 |

The bottom part of the sample was designed with a cylindrical shape, which is not the case for the real piece (see Figure 4-1a-b). This cylindrical part remains outside of the taper/bore interface and increases the area of the cathode, which in turn enlarges the cathode/anode ratio.

In addition, in this cylindrical part, an internal hole was made to ensure the electrical connection as shown in Figure 4-1b. To reproduce the thread on the surface of taper samples, the pattern should end at the same level as the trunnion finishes and changes to a cylinder. Thus, the length of the surface pattern corresponds to the length of the bore creating the crevice, as occurs in the real case. Pattern profile is shown Table 5.2.

Metallic samples were rinsed with water, cleaned in an ultrasonic bath in two steps. Firstly, acetone was used to eliminate traces of grease from the machining. Secondly, samples were cleaned using ethanol.

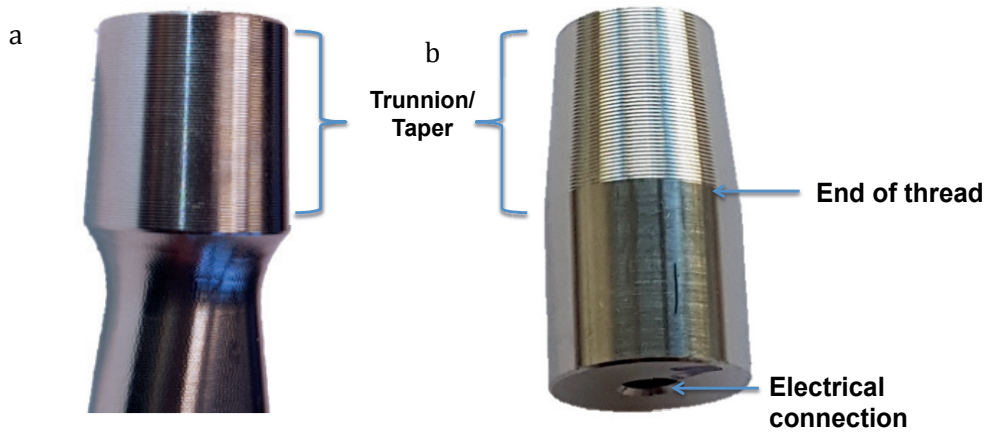


Figure 4-1. Trunnion thread on a) real piece and b) sample

In parallel, a real femoral head was taken as model, no particular surface pattern is observed in the bore. From this modular piece, depth and cavity were reproduced as observed in Figure 4-2. Material used to reproduce the bore inside de femoral head was MACOR®. This material is a glass-ceramic composite composed of 55% fluorophlogopite mica and 45% borosilicate glass. MACOR® was chosen because of its machinability. For the conditions used in this work, the weight loss is expected to be insignificant at pHs used.

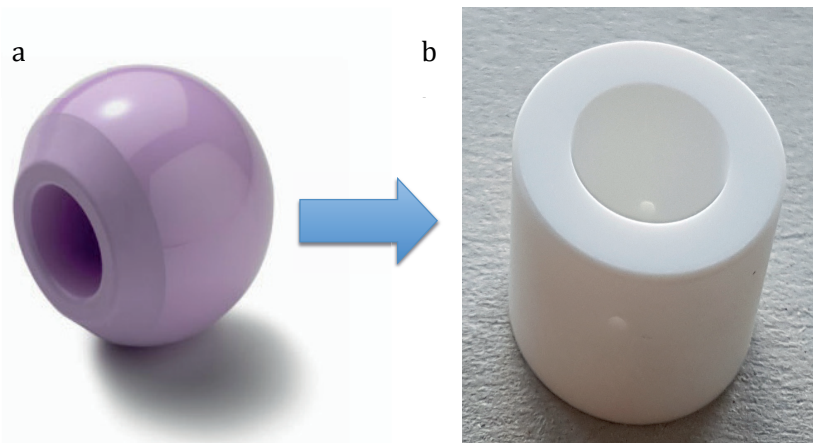

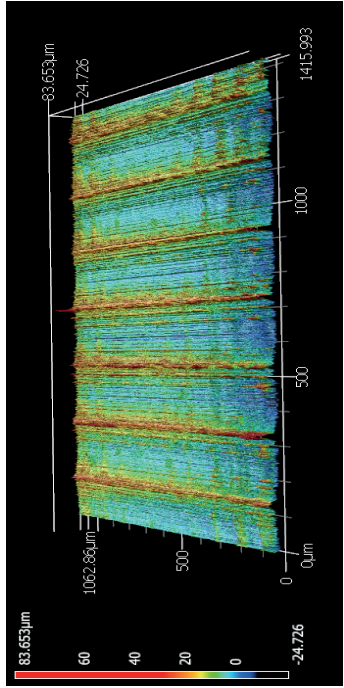
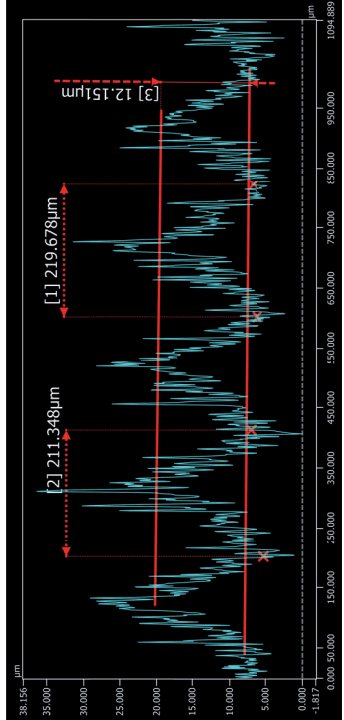

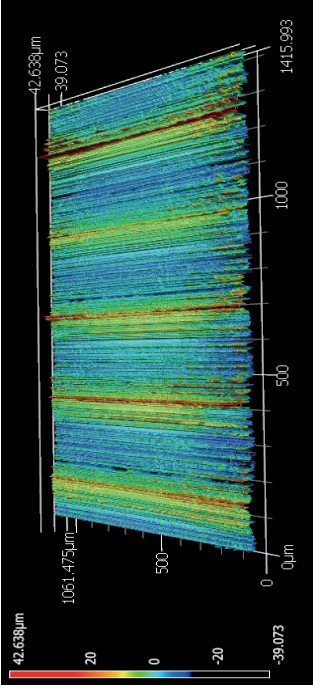
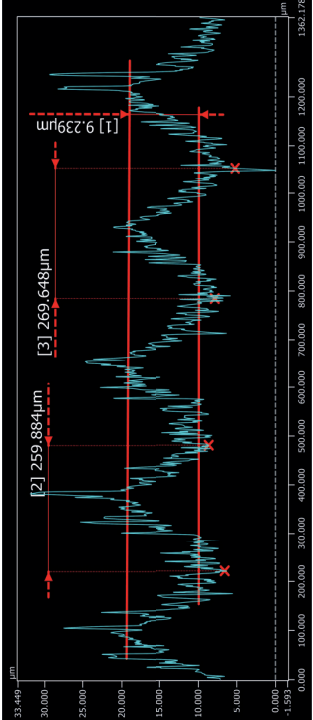


Figure 4-2. a) Real femoral head and b) ceramic sample mimicking the bore

Two cylindrical openings were created on the ceramic sample, through which the electrolyte can pass. Those points were used to measure potentials at different heights of the trunnion.

Ceramic pieces were cleaned with water and soap to eliminate impurities. Next, they were immersed in ethanol in an ultrasonic bath during 1 hour, and dried with compressed air.

Table 4-2. Comparison between real taper and sample surface properties (measurements done using a Laser Scanning Confocal Microscope, Keyence VK-X200 Series 3D)

| Type | Taper image | Thread finishing | Surface pattern profile |
|--|--|---|--|
| <p style="text-align: center;">Real taper</p> |  |  |  |
| <p style="text-align: center;">Sample</p> |  |  |  |

4.1.2 Cell configuration

To complete the system an electrochemical cell made of Poly-(Methyl Methacrylate) (PMMA) was designed. Dimensions of the cell are given in Figure 4-3. The internal diameter of the cell coincides as closely as possible with the external diameter of the ceramic head to decrease the electrolyte leak. In addition, three O-rings are positioned between the ceramic head and the cell to seal the contact and avoid leaks.

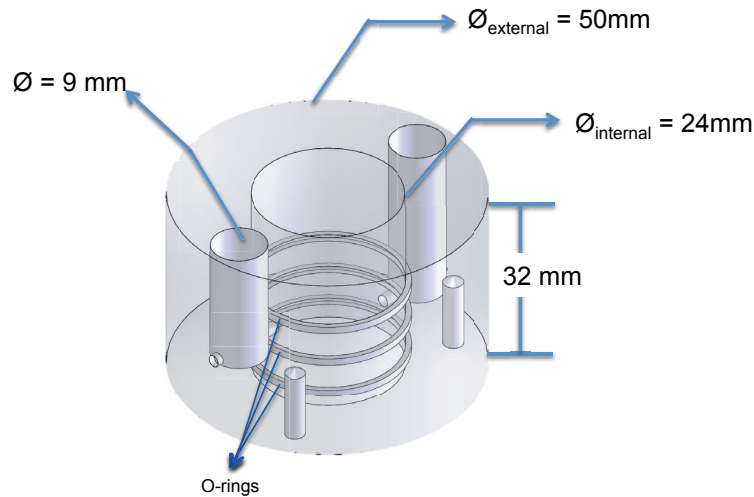


Figure 4-3. Crevice-corrosion cell

Three different potentials can be registered under this configuration. The first one corresponds to the central reference electrode, which measures the difference in potential between the reference and the working electrode. This central reference electrode (CRE) is located outside of the crevice, on the surface. Second and third potentials can be measured at two different heights of the trunnion, once the cell is assembled. The purpose of those measurements is to register the potential drop along the crevice.

As Figure 4-4 and Figure 4-5 show, the cell has two cylindrical lateral openings, which are aligned to the holes made in the ceramic head and connect with them through small channels. Their purpose is allowing to measure the potential of the metallic taper at different heights once the cell is assembled.

Heights where potentials are measured in the metallic taper length are shown in Figure 4-4. Position 1 corresponds to registered potentials at the highest point in the trunnion (4.5 mm from the tip of the crevice mouth), reference electrode used here was called as RE1. Position 2 is related to the deepest point where potential was measured (10mm from the tip of the crevice mouth) with reference electrode RE2.

Two covers complete the cell. One of them is located in the bottom part to align pieces and to close the cell using screws. The top cover avoids evaporation of liquids and its openings help to position the electrodes, see Figure 4-5. Silicone taps were inserted in those openings to decrease evaporation once the electrodes were installed.

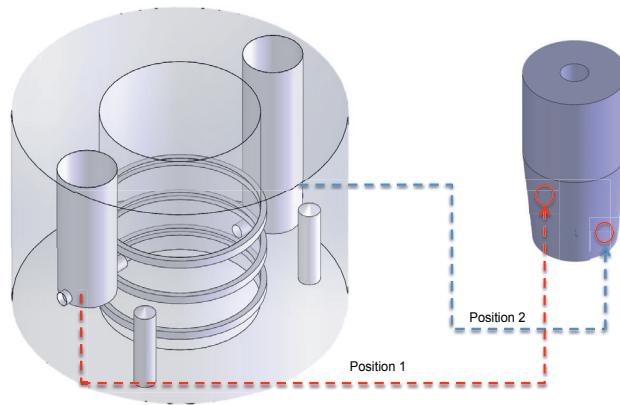


Figure 4-4. Lateral reference electrodes position respect to the cone length

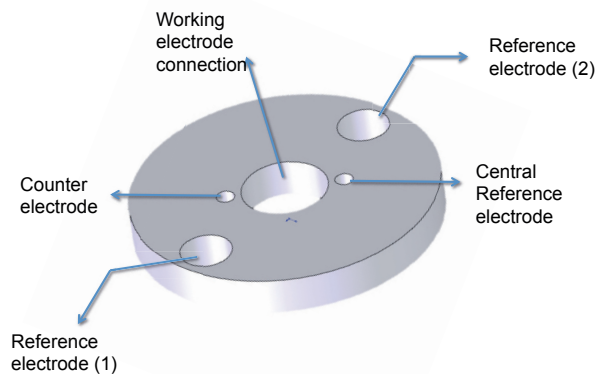


Figure 4-5. Crevice-corrosion cell cover

To carry out each experiment the cell had to be assembled. Every ceramic head was introduced in the PMMA cell. The alignment and the bottom closure must be ensured to fill the cell with the electrolyte. Once the liquid level of the lateral openings and in the ceramic head is the same, the metallic cone was positioned.

To reproduce the fixation made in a normal surgery, every metallic cone was hammered twice with an average force of 300 (N). The counter electrode and the three references electrodes were positioned as well as the working electrode connection as Figure 4-6 shows.

All experiments were carried with Ag/AgCl reference electrodes. All electrodes were calibrated with respect to the central reference one. A platinum wire was used as a counter electrode; this electrode was surrounding the working electrode outside of the crevice and its area was 38 mm².

To corroborate if crevice-corrosion conditions can be produced in the modular femoral head/neck junction, the validity of this experimental approach was based in crevice-corrosion tests carried out on samples made of stainless steel - FeCr15%. The sensitivity of this alloy to crevice-corrosion conditions has been demonstrated in previous study by

Stemp et al [120]. In consequence, metallic trunnions of this material were evaluated under the configuration proposed in this work.

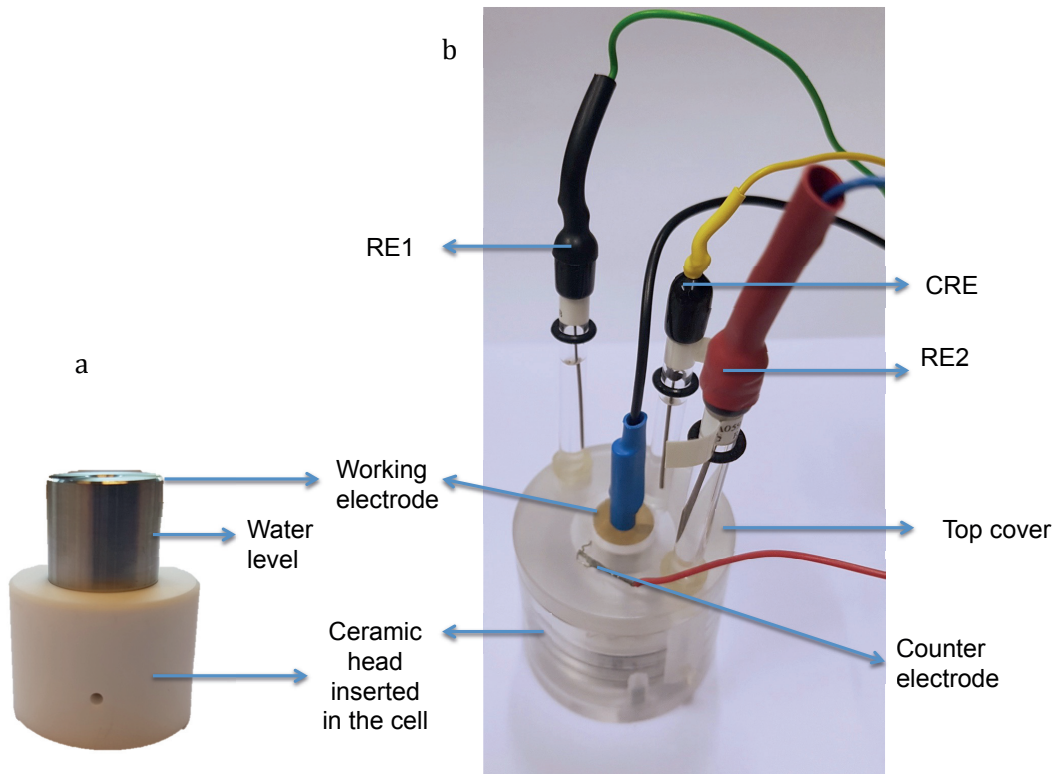


Figure 4-6. a) Taper and bore samples assembled b) Crevice-corrosion cell assembled

Geometrical considerations

Trunnion angle and the bore angle are defined in Figure 4-7. Angle mismatch between those pieces was kept positive as it is recommended for ceramic femoral heads and metallic trunnions.

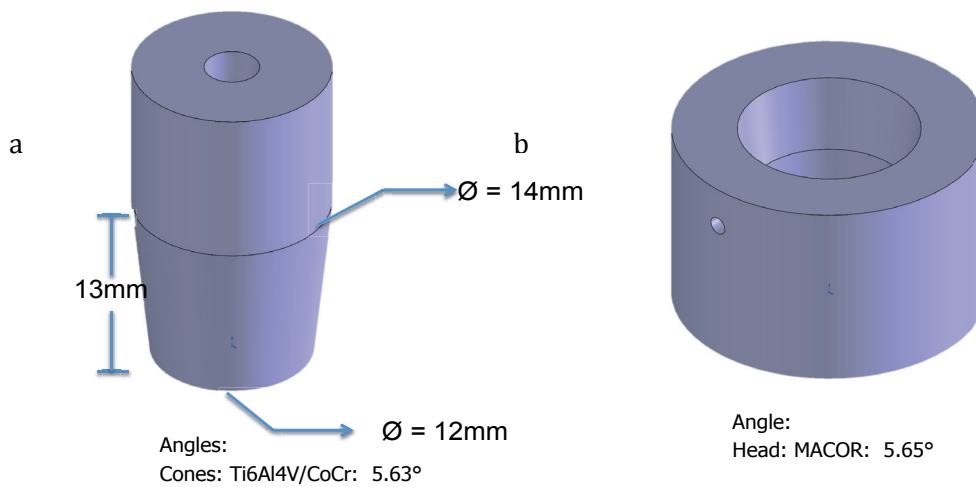


Figure 4-7. a) Design and b) assembly of metallic taper and ceramic head samples.

This angle mismatch creates the gap, which is localized at the tip of the cavity (wider distance), decreases along the length of the cone and disappears where the two pieces are in contact. The gap considered in the model was the widest.

The initial gap between the metallic and the ceramic cone was defined, as the difference in angles of the two cones as Figure 4-8 and the following calculations show:

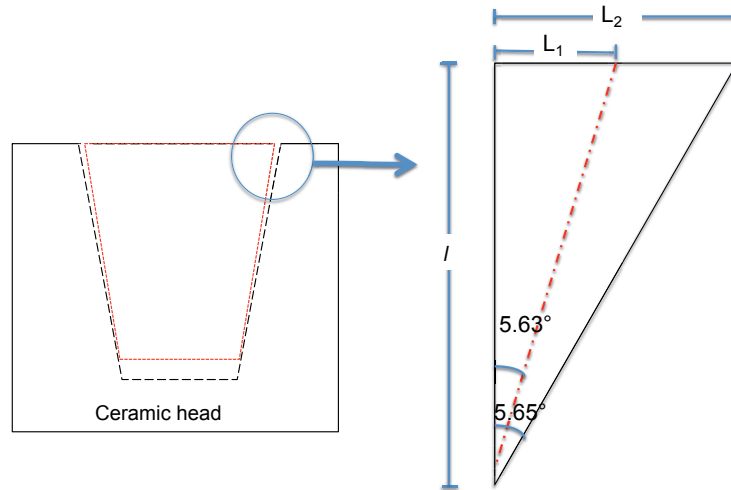


Figure 4-8. Gap geometry

Where,

$$L_1 = l * \tan(5.63^\circ) \quad (23)$$

$$L_2 = l * \tan(5.65^\circ) \quad (24)$$

$$g = L_2 - L_1 \quad (25)$$

In this configuration, initial l value is 13mm. So, the initial gap is about $4.6\mu\text{m}$ (0.02°), which is inside of the tolerances from current trunnion designs found in literature [17]

To mimic the insertion procedure followed during a normal surgery, each metallic cone was hammered into the ceramic piece. Consequently, the initial gap was reduced because of the elastic deformation of the metallic piece and the plastic deformation produced in the peaks of the thread, represented in Figure 4-9.

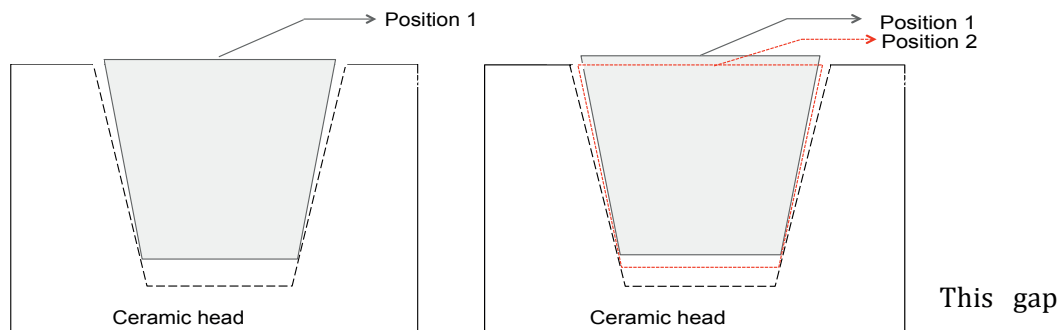


Figure 4-9. Scheme about the taper displacement and gap change a) initial position and b) after being hammered

modification was analyzed for its possible impact on the system; the ohmic drop in the crevice is inversely proportional to the dimension of the crevice gap. This in turn affects the current distribution and therefore the critical distance for having crevice corrosion [47], [69].

Taking this effect into account, the displacement of the metallic cone inside the ceramic had to be measured to define the new length L_1^* and in consequence the final gap. For this purpose 6 insertion tests were done using the three alloys assessed under crevice corrosion configuration for implants. The initial and final (after hammering) height of these two pieces assembled was measured and through a simple geometrical analysis the new gap was defined.

4.1.3 Electrical assembly and data acquisition

The set-up designed for crevice-corrosion experiments is able to measure and acquire data for six cells simultaneously. Data acquisition system was designed to collect potential and current over time.

Potential was applied using an AMEL Potentiostat-Galvanostat (model 549, max. voltage output 10V-12V). From the experiment design, the system had to be able to collect the following data:

- Applied potential: corresponds to the measured potential between the working electrode and the central reference electrode.
- Potential 1: Refers to the measured potential between the working electrode and the lateral reference electrode 1 at position 1.
- Potential 2: corresponds to the measured potential between the working electrode and the lateral reference electrode 2 at position 2
- Current: Potential between the counter and working electrodes was measured. A resistance was installed in order to collect directly the current value.

The internal resistance of the instrument, the solution resistance and the external resistance of the circuit were considered. For Ti6Al4V and CoCr configuration, the value of the external resistance used was 200 K Ω , which gives a precision of 20 μ A in the measurement. For SS FeCr15%, the external resistance used was 10 Ω , which allowed registering the high current values for this system. However, the precision of the system was compromised and reduced to 10mA.

The diagram in Figure 4-10 describes all the connections from the potentiostat to the cells and from the cells to the board installed in a Macintosh PowerMac G4.

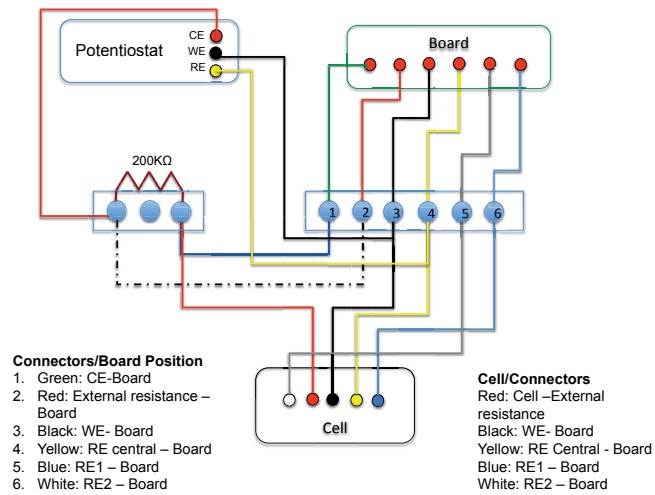


Figure 4-10. Diagram describing potentiostat-cell-board connections

The model used for the card board was NI-6031E from National Instruments with 32 channels in differential, a resolution of 16bits, a maximum frequency of 100kS/s and an input range of $\pm 0.5V$. All the data was collected through a software LabView version 5.1 adapted to the system. Figure 4-11 all the system assembled and working.

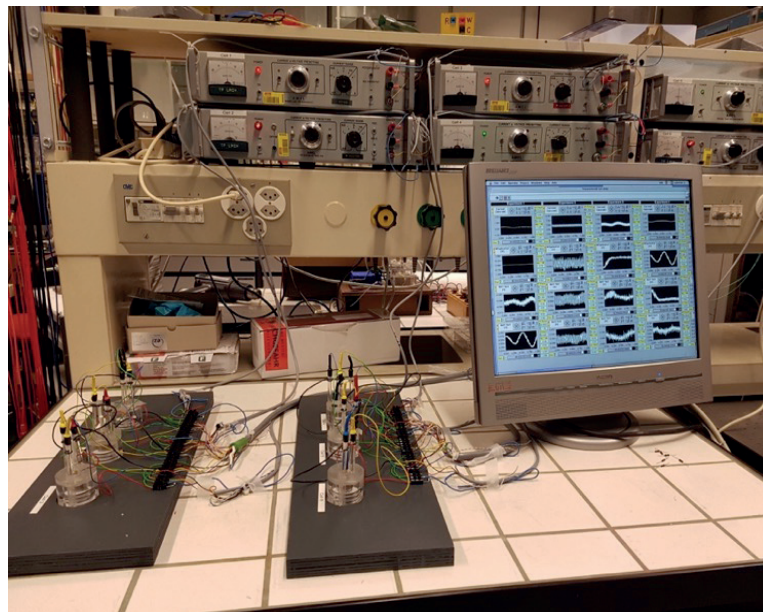


Figure 4-11. Image of the Crevice-corrosion test set-up

4.1.4 Chemical conditions

For the crevice-corrosion experiments on Ti6Al4V and CoCr alloy, NaCl 0.9%wt was chosen as electrolyte to avoid the effect of the solution resistance and include de Cl⁻ ions. At this liquid composition and two pHs of 2.3 and 5.6 were tested. The former pH was adjusted by addition of HCl 0.1M. Solution conductivities are given in Table 4-3. For

experiments where the material evaluated was the SS Fe15%Cr, a sulfuric acid solution 0.05M was used to guarantee the control of crevice corrosion growth.

Table 4-3. Solutions conductivities

| Solution | Conductivity (S/cm) |
|--------------------------------------|--------------------------------|
| NaCl, pH 2.3 | 1.71E-02 |
| NaCl, pH 5.6 | 1.40E-02 |
| H ₂ SO ₄ 0.05M | 2.83E-02 |

To analyze different electrochemical conditions, two different potentials were applied for each pH. To select the applied potentials and to characterize the anodic, cathodic and active zones, polarization curves for the three materials were measured using a typical three electrodes configuration in all solutions at a sweep rate of 2mv/s. Potential ranges studied for each material are indicated in Table 4-4.

Table 4-4. . Potentials scanned and solution pH used for polarization curves

| Material | Solution | pH | Potential Range vs Ag/AgCl (V) |
|-----------------|--------------------------------------|-----------|---|
| CoCr | NaCl 0.9%wt | 2.3 | -1.5 – 1.5 |
| | | 5.6 | |
| Ti6Al4V | | 2.3 | -2.0 – 2.0 |
| | | 5.6 | |
| FeCr 15% | H ₂ SO ₄ 0.05M | 1.5 | -1.2 – 1.5 |

Passive potentials were imposed to ensure the oxide layer formation. Potentials where the oxide layer was not stable were also considered.

Ti6Al4V and CoCr were tested under crevice-corrosion conditions during 4 weeks. For each potential and pH, two cells for every material were evaluated. Daily, solution evaporation was checked and liquid adjustment was done at the top of the samples but also in the channels that connect with the crevice.

4.2 Results

4.2.1 Crevice-corrosion of Stainless Steel - FeCr15%

In the polarization curve presented in Figure 4-12, an active-passive transition is observed around $-0.3V(V_{Ag/AgCl})$. Accordingly, potential chosen for crevice-corrosion experiments was $0.5V(V_{Ag/AgCl})$. At this potential the Stainless Steel (SS) FeCr15% forms a passive layer on the surface.

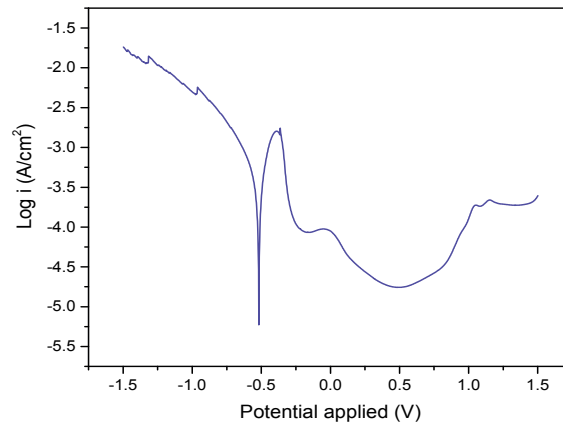


Figure 4-12. Polarization curve of SS FeCr15% in H_2SO_4 0.05M solution

Crevice-corrosion experiments using FeCr15% samples were limited to a maximum duration of 2 days due to the high degradation level reached during this time.

Figure 4-13 corresponds to the potential and current evolution of crevice-corrosion test carried out for less than 20 hours. A potential drop of approximately 1V inside the crevice (RE 1 and RE2) compared to the applied potential (CRE) was registered since the beginning of the experiment. Small increases and instabilities of the potential are registered, even though, no significant changes are observed in the current evolution.

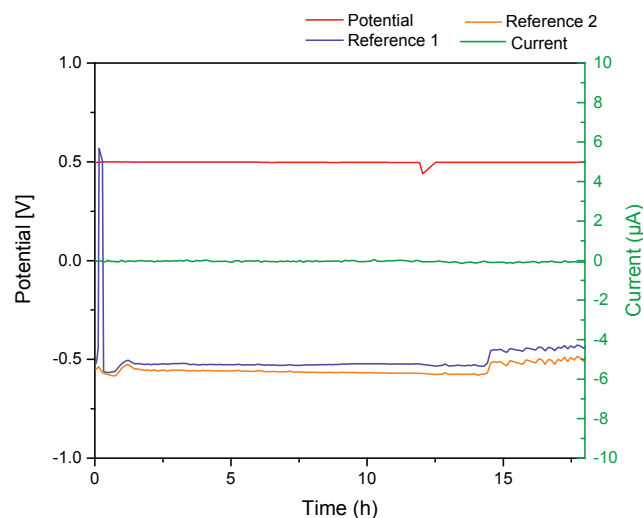


Figure 4-13. Potentials and current evolution of stainless steel FeCr15% sample under crevice-corrosion configuration during 18 hours. Potential applied: $0.5V (Ag/AgCl)$, Solution used: H_2SO_4 0.05M

Crevice-corrosion spots were observed on the thread pattern (Figure 4-14). Those areas correspond to the initial points where material dissolution occurred. However, even if the extension of the damage during the test was not enough to provoke a notable increase in the current, crevice-corrosion takes place. Small areas affected by crevice-corrosion in Figure 4-14 were located around 1mm to 1.5mm from the top of the crevice.

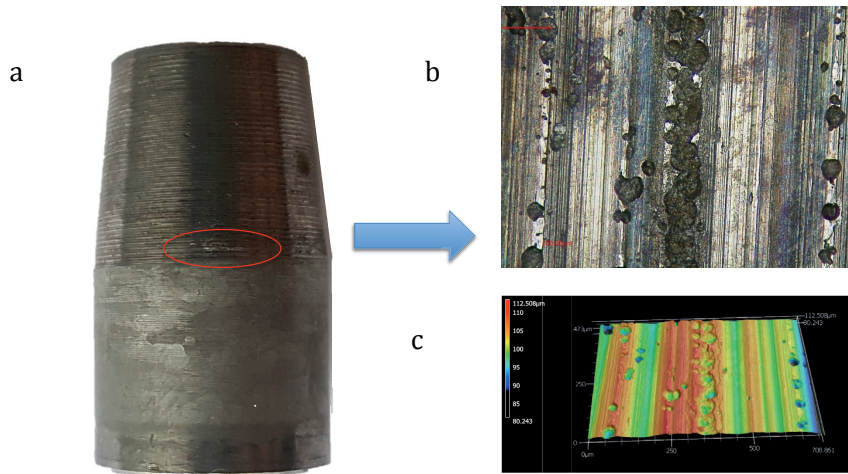


Figure 4-14. Stainless steel cone after 18 hours of test a) cone, b) crevice-corrosion microscope image 10x, c) profile of the defect.

Afterwards, samples were evaluated during 32 and 38 hours. Figure 4-15a corresponds to the potential and current evolution of a sample evaluated under crevice-corrosion conditions during 32 hours, which is shown together with the linear polarization curve. During the first five hours, a potential drop of approximately 1V inside the crevice (RE 1 and RE2) appeared with respect to the applied potential (CRE). Subsequently, both potentials increase and stabilized around -0.2V, which corresponds to the active region as observed in the polarization curve in Figure 4-15b.

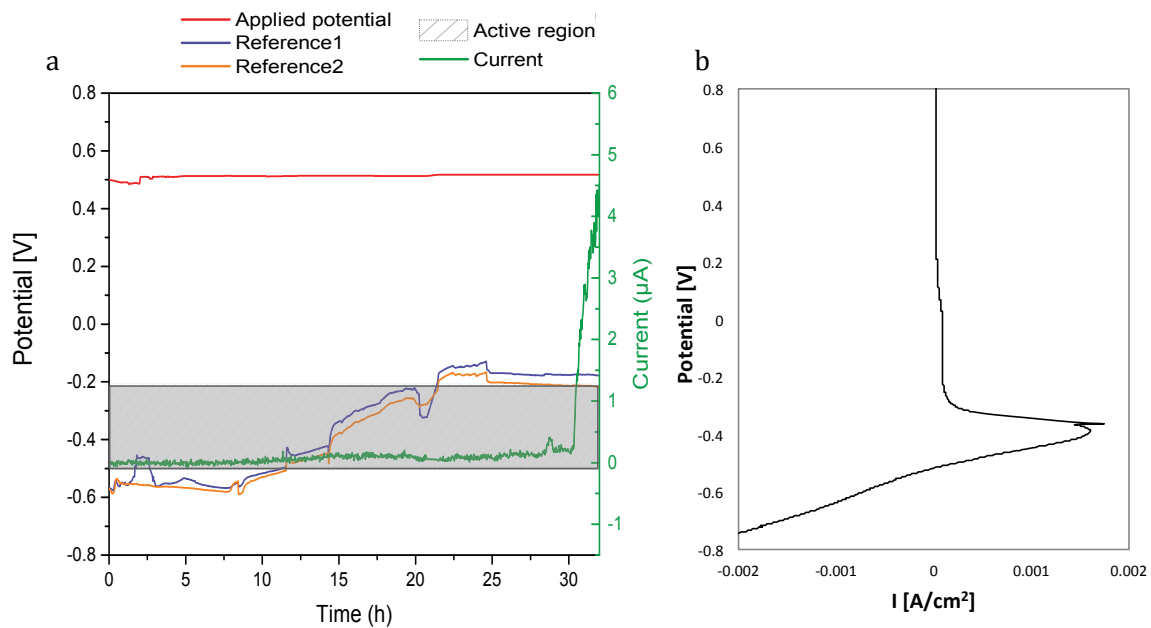


Figure 4-15. a) Potentials and current evolution of stainless steel FeCr15% sample under crevice-corrosion configuration during 32 hours. Potential applied: 0.5V (Ag/AgCl), Solution used: H₂SO₄ 0.05M, b) Linear polarization curve.

As consequence, material dissolution at this potential takes place inside the crevice as observed by the corrosion damage in Figure 4-16, which leads to current increase, represented by the green line.

A big crevice corrosion defect was found when the contact was opened, this crevice is placed in the proximal area of the taper-bore configuration (Figure 4-16 a-d). The pH of the bulk solution increases from an initial value of 1.5 to 3.0 at the end of the experiment. This can be associated with the precipitation of oxide particles in the solution that was observed at the end of the experiment. The limited oxygen transport at the bottom of the crevice can vary with the reduction of the proton (water).

A linear surface profile of the taper was measured to characterize the depth and location of the crevice corrosion (Figure 4-16b). In this profile, the inclination was inverted in the sample holder, in order to cover a major part of the sample. Therefore, a green circle marks the conic part (taper) while the upper part corresponding to the cylinder (outside of the crevice) will be in black. A drop can be noticed in the profile at 1.5 – 2 cm in the proximal distance of the contact. This distance can be defined as the critical distance where crevice-corrosion is going to take place. Figure 4-16c and d show details of the damage in the crevice.

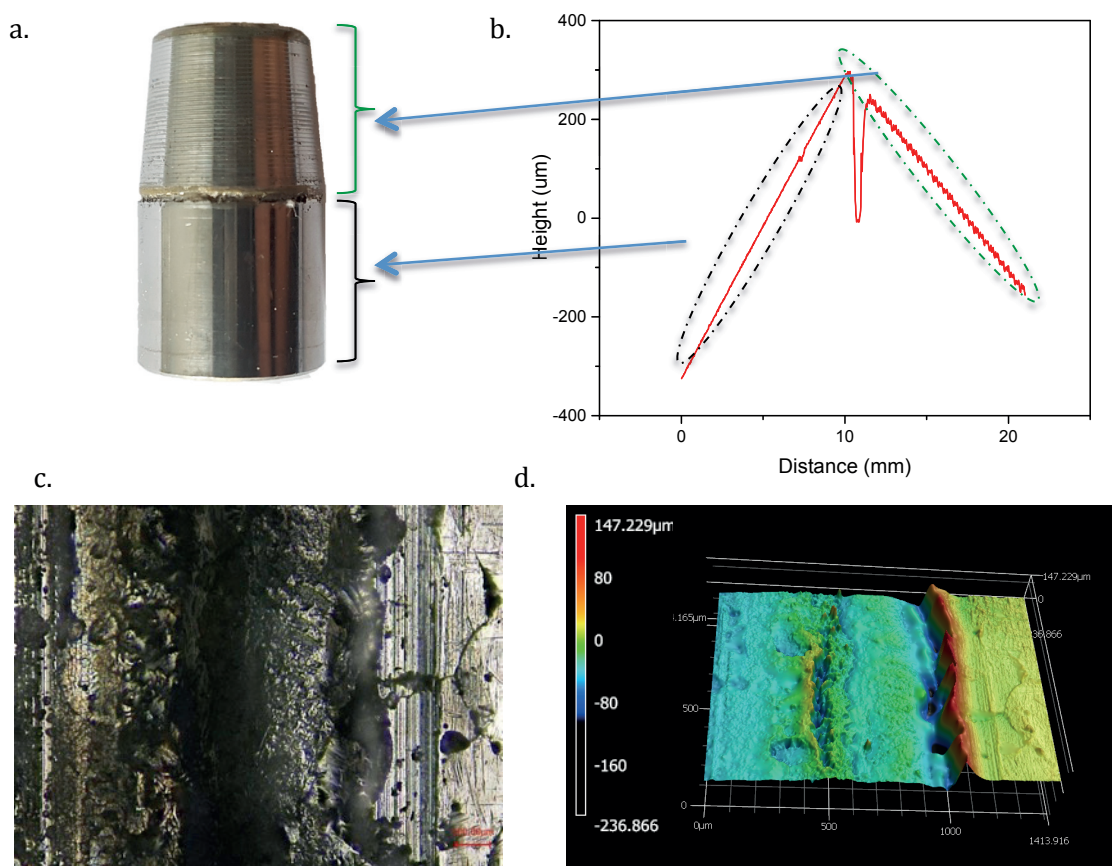


Figure 4-16. Crevice corrosion in FeCr15% taper evaluated during 2 days under crevice-corrosion conditions. a) taper, b) surface profile measured using a UBM scanning laser telefocus profilometer, c) crevice-corrosion defect and d) defect profile measured using a laser confocal microscope, Keyence VK-X200 Series 3D

Crevice-corrosion degradation occurs in sample evaluated during 38 hours in a less extended surface area with respect to sample tested during 32 hours. This difference in the damage can be observed in Figure 4-17.

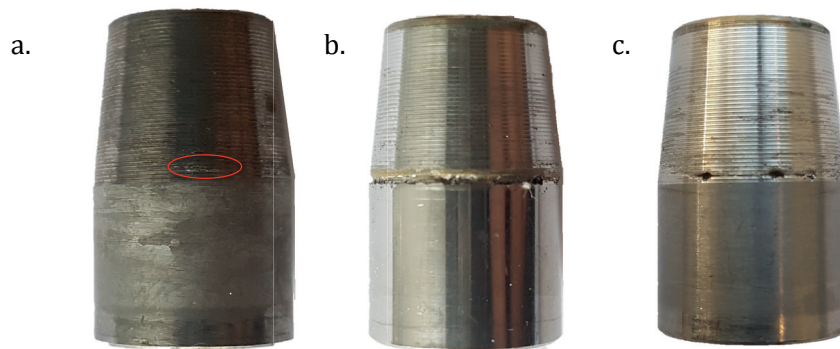


Figure 4-17. Severity of crevice - corrosion degradation on FeCr15% taper in H_2SO_4 0.05M at 0.5V ($V_{Ag/AgCl}$) a) Sample 1 (after 18 hours), b) Sample 2 (after 32 hours) and c) Sample 3 (after 38 hours)

Differences in the level of deterioration can be explained by the potentials measured by RE1 for sample 2 and 3. Contrary to the sample 2, in the experiment carried out during 38 hours, potentials registered by RE1 were lower than the potential applied but higher than the potentials from the active domain, during the first 15 hours as shown in Figure 4-18. After, potentials registered in position 1 decreased to reach active values leading to material dissolution.

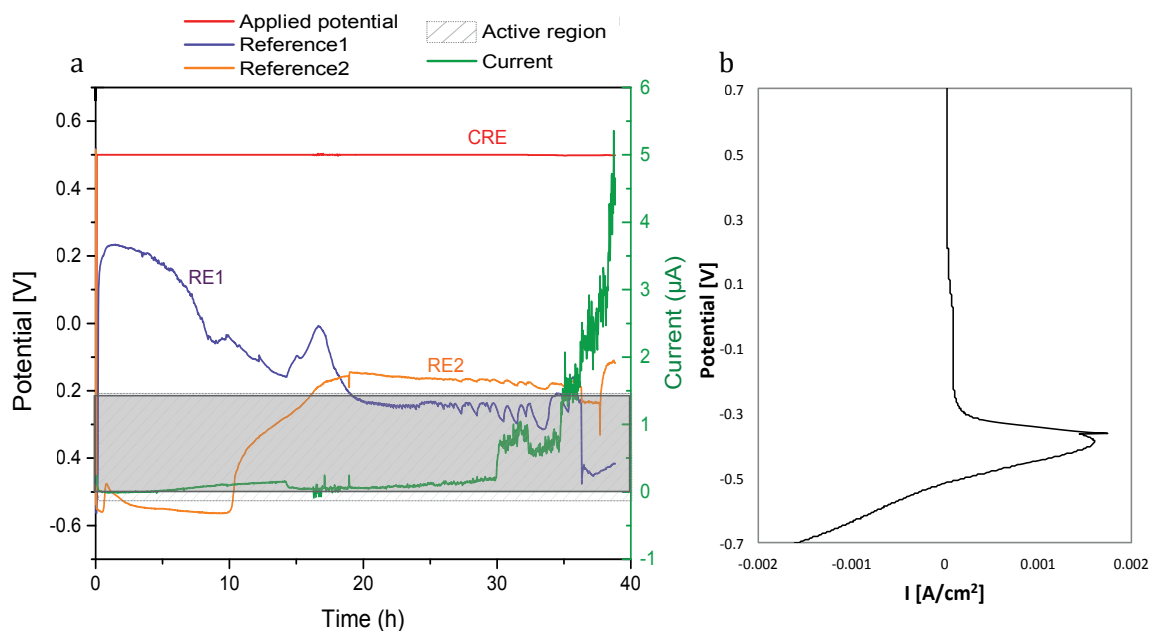


Figure 4-18. a) Potentials and current evolution of stainless steel FeCr15% sample under crevice-corrosion configuration during 38 hours. Potential applied: 0.5V (Ag/AgCl), Solution used: H_2SO_4 0.05M, b) Linear polarization curve.

Moreover, values registered by RE2 for sample 3 are different of those registered for sample 2. In the later case, potential initially dropped almost 1V compared to the potential

applied, however, after 10 hours, this potential increased to more positive values close to the upper limit of the active-passive transition.

Difference in potentials measured between samples can be associated to changes in the position of the RE1 and RE2 with respect to the location where the crevice-corrosion is happening. This difference in the height and potential is a direct consequence of the variation in hammering force during the insertion process.

Current evolution of sample 3 shows stability during a period of 28-30 hours, even though; a slighted increasing though stable rising trend was noticed. Afterwards, current values increased dramatically, which indicates that to initialize crevice-corrosion, potential drop inside the crevice is independent of the current.

Figure 4-19 shows the crevice-corrosion failure in detail for sample 3. Here it is evident that damage has extended from the initial spots around the diameter of the trunnion and has created deep holes as Figure 4-19c -d show.

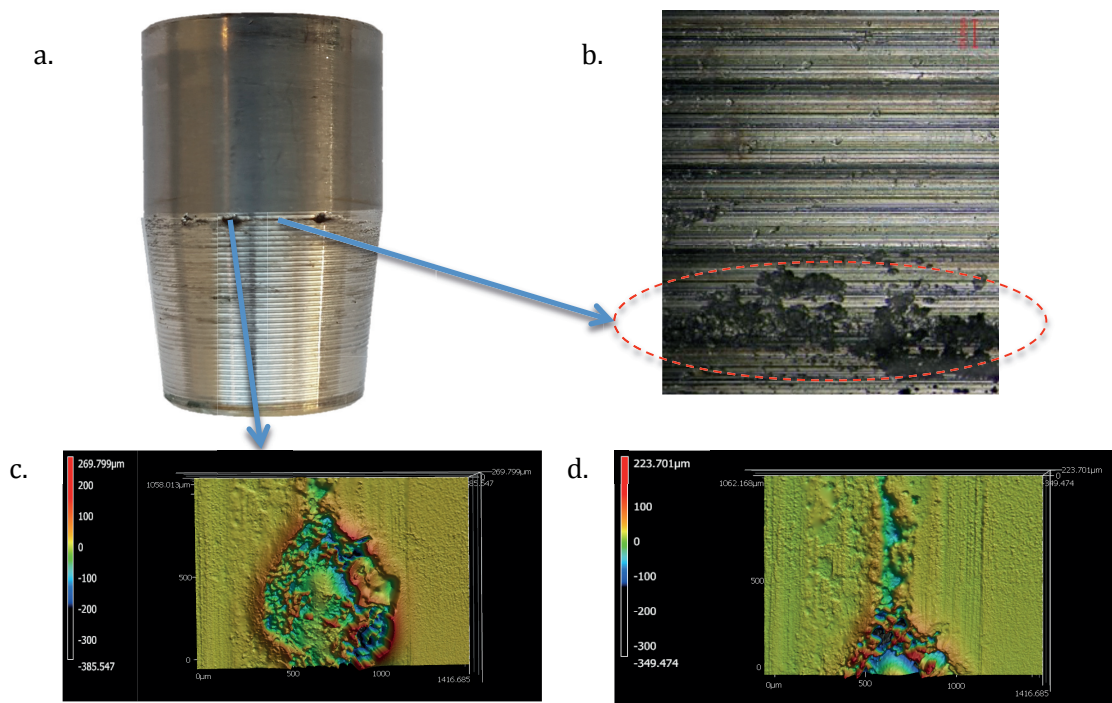


Figure 4-19. Crevice corrosion in FeCr15% taper 2 evaluated during 40 hours under crevice-corrosion conditions. a) taper, b) crevice-corrosion defect, c) and d) zoom in big defects

Finally, the end of the trunnion sample was examined to check if there was any crevice-corrosion at this height. No significant deterioration was found in neither of the two samples. From Figure 4-20a and b show the microscope image and 3D surface topography of the taper end after the test.

From the profile of the thread surface it can be noted that peaks are lower compare to the profile shown in Table 4-1 where a comparison was made between real taper and the designed sample before the experiments. This corresponds to the degradation of peaks during the insertion process.

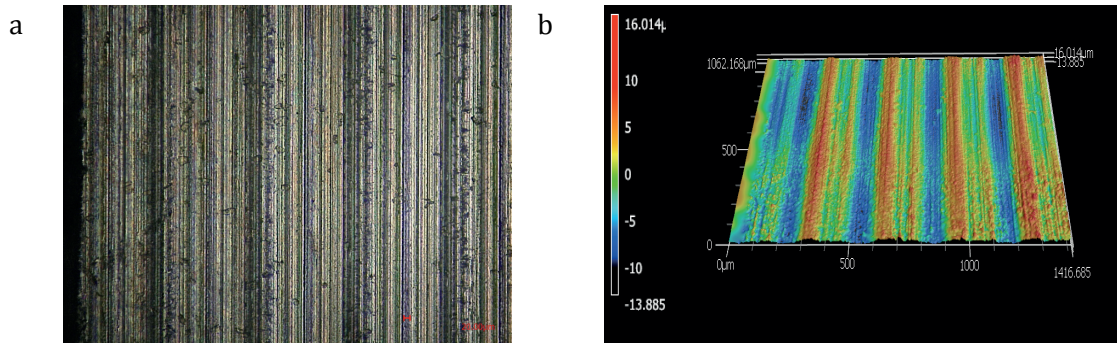


Figure 4-20. a) Microscope image 10x and b) profile of thread surface of FeCr15 % taper end after 40 hours test, in H₂SO₄ 0.05M at 0.5V(V_{Ag/AgCl}).

4.2.2 Crevice-corrosion behavior of CoCr

From the polarization curves measured in solutions with pH 2.3 and 5.6, it is seen that CoCr exhibited a clear plateau (Figure 4-21a and b) where the oxide layer is stable.

Crevice-corrosion experiments for CoCr alloy started with the most conductive solution. Two potentials were chosen: -0.1V (V_{Ag/AgCl}) that corresponds to the anodic region where the material is passive, and 0.5V (V_{Ag/AgCl}), where the oxide layer is unstable.

Because no noticeable effects were found in the experiments carried out in acidic solution, one single electrode potential, -0.1V (V_{Ag/AgCl}), was used for performing tests in the solution with pH of 5.6.

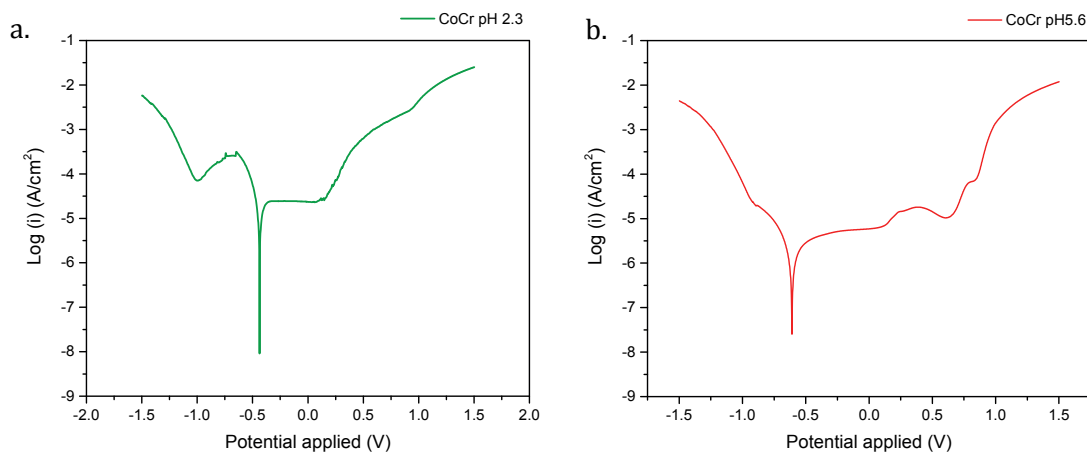


Figure 4-21. Polarization curve of CoCr alloy in NaCl 0.9% a) pH 2.3 and b) pH 5.6.

Figure 4-22 represents current and potential evolution of CoCr under crevice corrosion conditions in pH 2.3 under passive condition. In this case, after 30 days, no significant difference in potentials along the taper distance was registered. Values measured from RE1 and RE2 were almost stable during the whole experiment and very close to the applied potential.

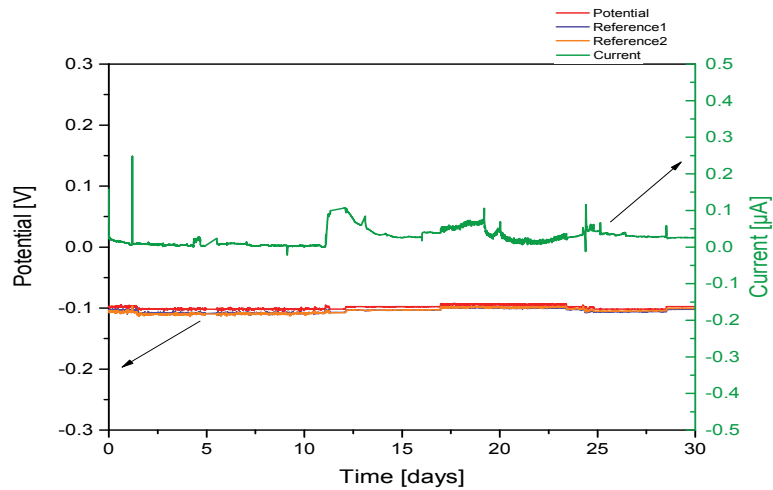


Figure 4-22. Potential and current evolution with time for CoCr in crevice-corrosion configuration in NaCl 0.9%wt pH 2.3. under -0.1V

Furthermore, low current values were registered during the entire test. Some fluctuations lower than $0.1 \mu\text{A}$ were measured, which can be attributed to small potential variations on the electrical system.

For crevice-corrosion experiments carried out at 0.5V no obvious potential drop was measured as Figure 4-23 shows. Potential difference between the potential applied and those registered by RE1 and RE2 do not exceed 20mV.

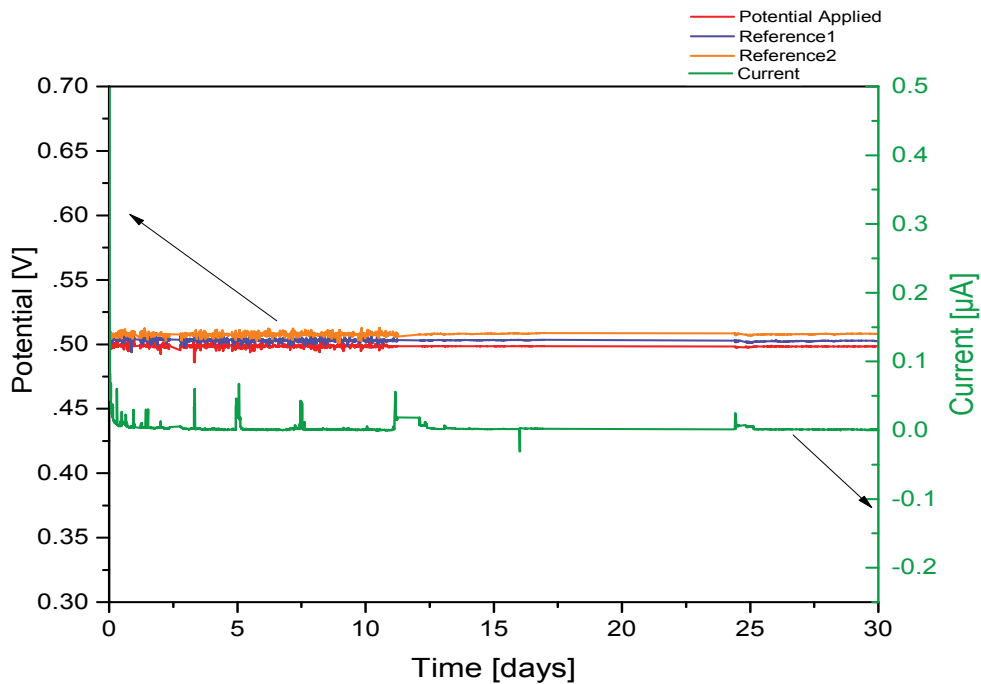


Figure 4-23. Potential and current evolution with time for CoCr under crevice-corrosion configuration in NaCl 0.9%wt pH 2.3. Potentials applied 0.5V ($V_{\text{Ag}/\text{AgCl}}$).

At the very beginning current values were high due to the initial passivation. But they quickly stabilize at values lower than $0.1 \mu\text{A}$ until the end of the experiment. Some

variation were detected and can be attributed to system fluctuations as they are much lower than those registered for depassivation.

In both cases, for passive and transpassive domains, potentials on the surface and inside of the crevice are almost equal. This leads to the conclusion that the electrochemical cell between the surface and the crevice, which is needed to generate crevice-corrosion, was not established.

A similar result was found in the experiments carried out in NaCl 0.9%wt with pH 5.6 as Figure 4-24 shows. Potential difference between the surface and RE1 and RE2 were very small (less than 20mV) during the entire experiment.

Small variations in current (lower than $0.2\mu\text{A}$) were recorded, positive and negative peaks are abrupt but they recover to stable current. These variations are also attributed to normal fluctuations of the system.

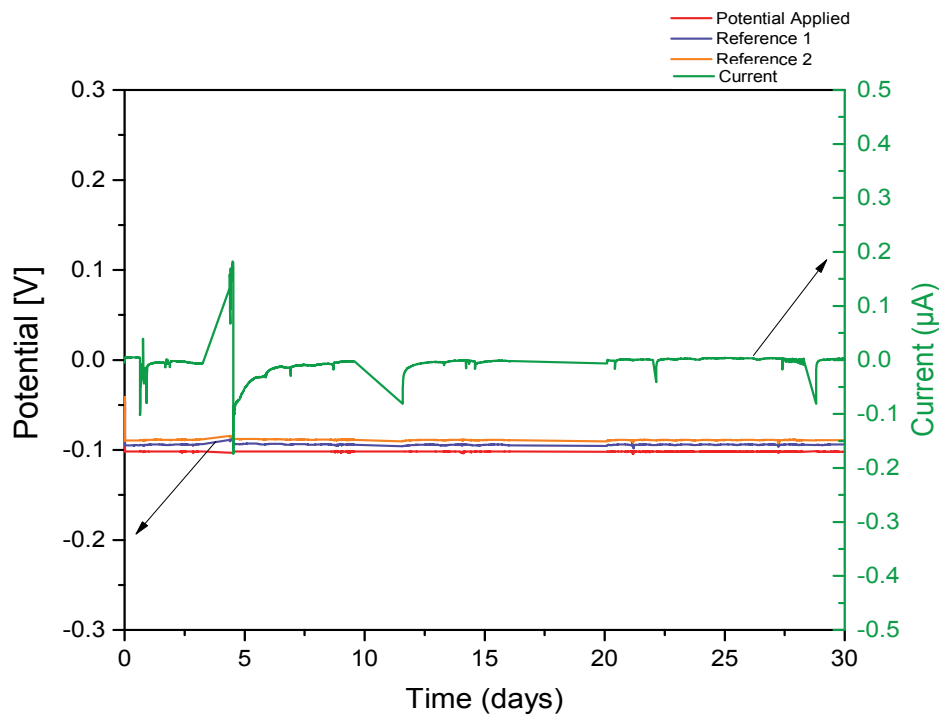


Figure 4-24. Potential and current evolution with time for CoCr under crevice-corrosion configuration in NaCl 0.9%wt pH 5.6. Potential applied -0.1V ($V_{\text{Ag}/\text{AgCl}}$).

Once the test was finished after 30 days, the contact was open for all the samples. None of them presented any defect or damage related to crevice corrosion. As Figure 4-25a and b can corroborate, no significant change was found on the samples.

The thread finishing and the surface in general did not suffer alterations by crevice-corrosion. However peaks heights are again different from the profile before testing. This is because of the insertion of the metallic taper by pressure.

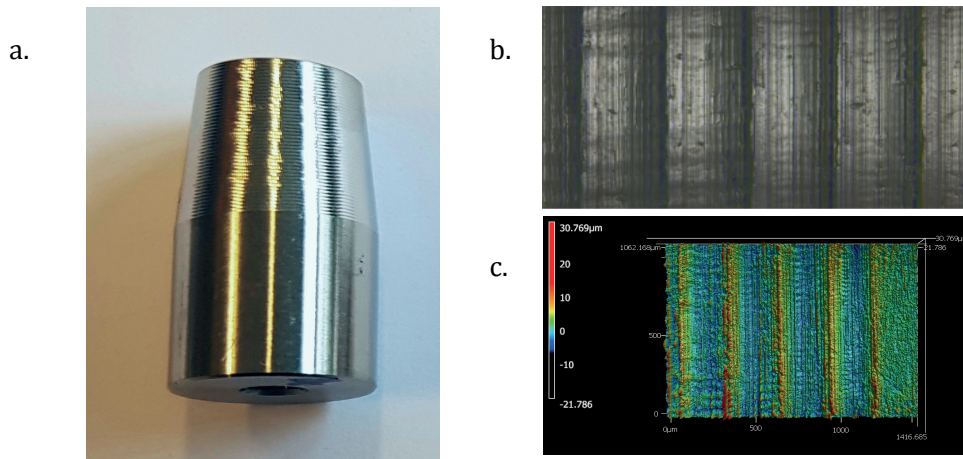


Figure 4-25. a) CoCr taper b) surface image and c) surface profile after 1 month under crevice-corrosion conditions. Potential applied $-0.1V (V_{Ag/AgCl})$. Solution NaCl 0.9% pH 2.3

4.2.3 Crevice-corrosion behavior of Ti6Al4V

Polarization curves carried out for Ti6Al4V in NaCl 0.9% pH 2.3 and 5.6 (Figure 4-26a and b) show almost the same large potential range where this alloy is passive. Therefore, passive potentials as 0.3V and 0.5V ($V_{Ag/AgCl}$) were chosen.

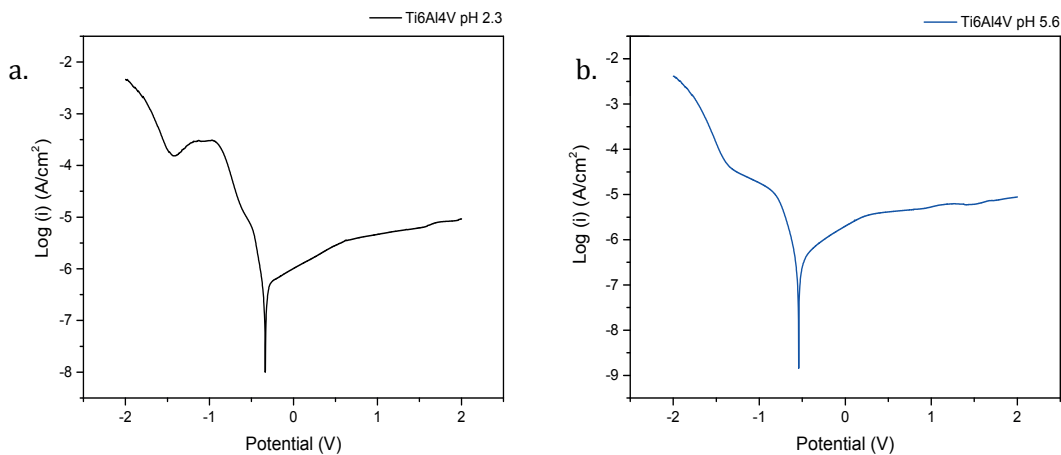


Figure 4-26. Polarization curve of Ti6Al4V alloy in NaCl 0.9% a) pH 2.3 and b) pH 5.6

As titanium oxide layer thickness strongly depends on the applied potential [46], the integrity of this layer under crevice-corrosion conditions has been questioned under conditions where the layer is less thick. Therefore, additional experiments were carried out under cathodic potential and close to the corrosion potential, E_{Cor} in NaCl 0.9%wt pH 2.3, under the harshest conditions in order to identify if crevice-corrosion takes place when the oxide film is thinner than under passive potentials.

Ti6Al4V presented a similar behavior to the CoCr alloy. In Figure 4-27 the current and potential evolutions under anodic conditions are represented for both solutions, NaCl 0.9% pH 2.3 and pH 5.6.

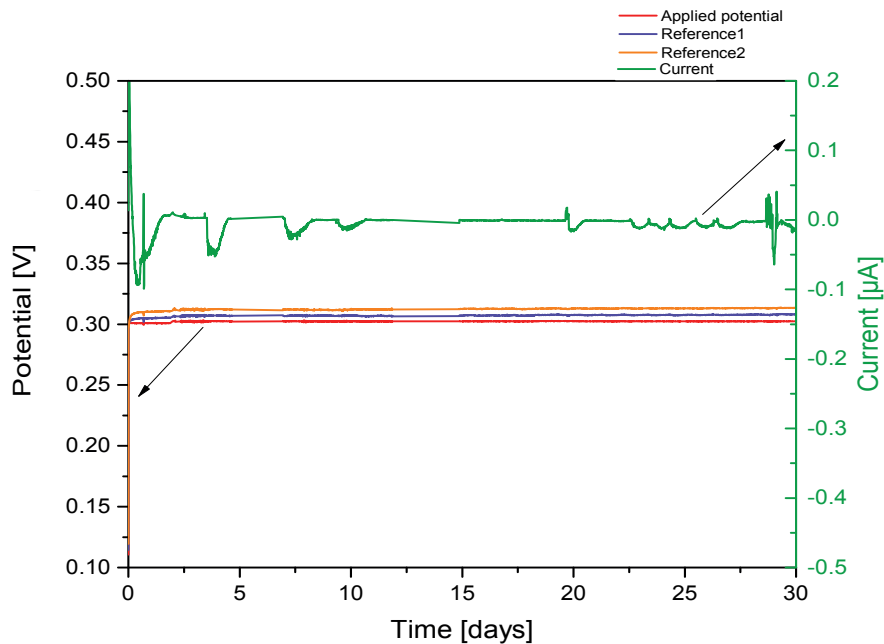


Figure 4-27. Potential and current evolution with time for Ti6Al4V under crevice-corrosion configuration in NaCl 0.9%wt pH 2.3. Potentials applied a) 0.3V ($V_{Ag/AgCl}$).

In acidic solution, the dissimilarity in potentials registered at different heights is negligible. Potentials measured along the taper was kept for one month without significant perturbations in potential, that means, no region in the configuration reached a potential that could destabilize the oxide layer. However, current evolution had some fluctuation over time. The first current peak registered could be consequence of the passivation generated by the applied potential and then oxide layer formation. Subsequently, once the oxide was formed, the current stabilized. After, some variations were observed (lower than $0.05\mu A$) that can be attributed to fluctuations in the system.

A similar behavior was reported for potential evolution of the system evaluated in NaCl 0.9%wt with pH 5.6 as Figure 4-28 shows. Neither in this case, significant potential drop was measured along the crevice. The small difference between the potential measured in the surface and in the bottom of the crevice did not exceed 20 mV during the whole test. Current fluctuations lower than $0.05\mu A$, even at the beginning of the test, were less noticeable.

Figure 4-29 shows no evidence of crevice-corrosion along the taper once the experiment was finished after 30 days. Surface topography measurements in Table 4-1, specially the thread finishing on the taper shows no significant changes.

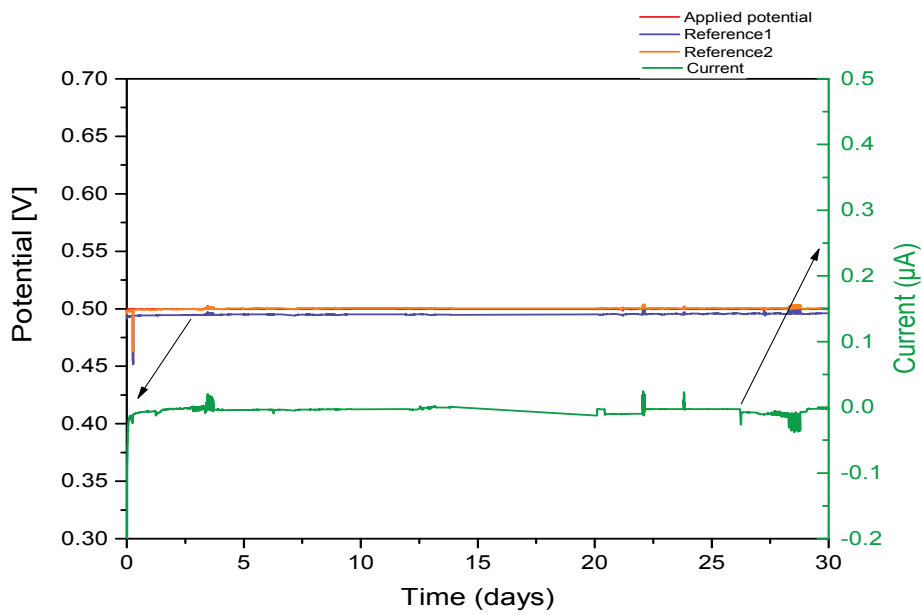


Figure 4-28. Potential and current evolution with time for Ti6Al4V under crevice-corrosion configuration in NaCl 0.9%wt pH 5.6. Potentials applied a) 0.5V ($V_{Ag/AgCl}$).

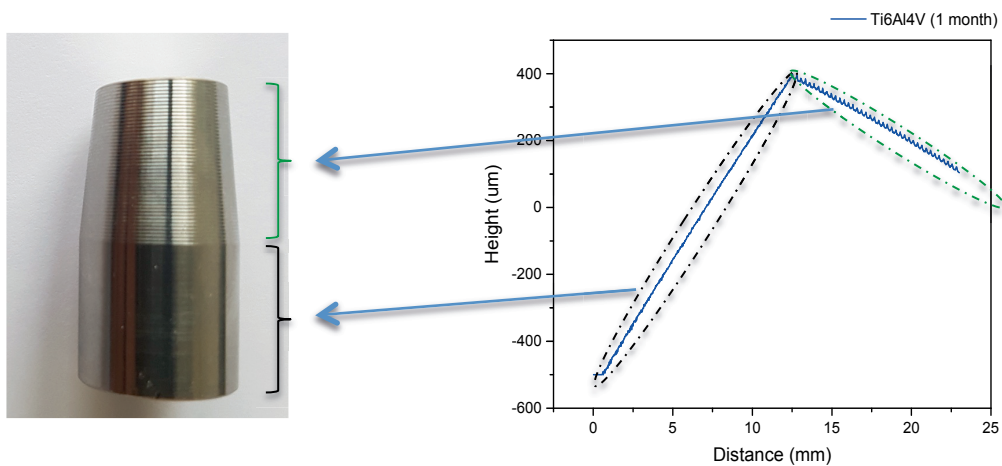


Figure 4-29. Ti6Al4V taper b) surface image and c) surface profile after 1 month under crevice-corrosion conditions. Potential applied: 0.3V ($V_{Ag/AgCl}$). Solution: NaCl 0.9% pH 2.3

Likewise, potential and current evolutions registered from experiments carried out at -0.5V ($V_{Ag/AgCl}$) are presented in Figure 4-30. At this potential that was close to E_{COR} , differences of 20mV and 50mV were measured during the whole experiment RE1 and RE2, respectively. However, this decrease is constant along the test. No significant change in current was remarked.

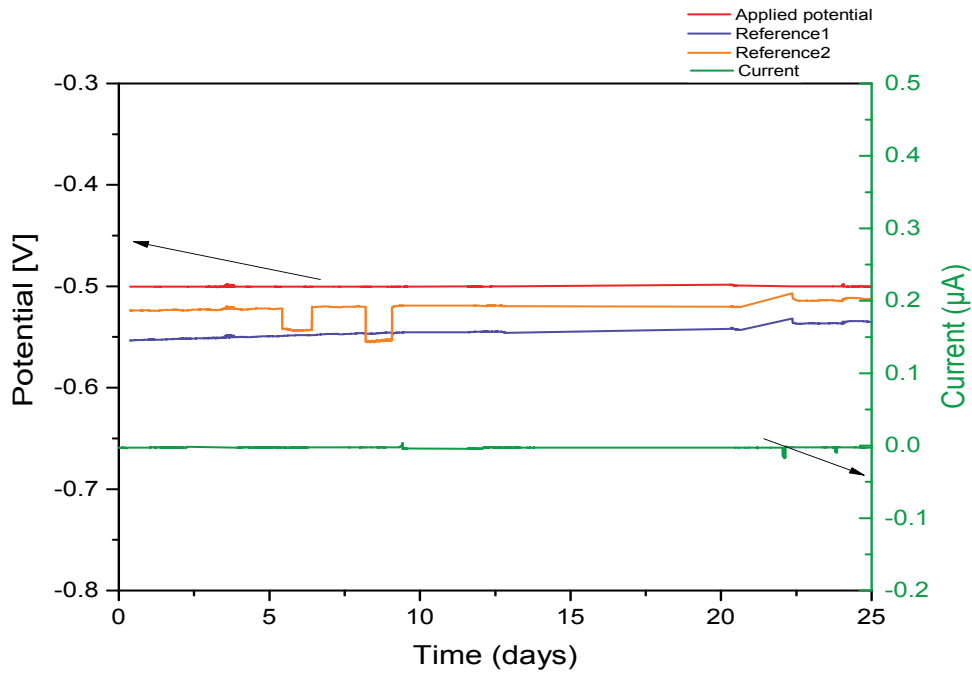


Figure 4-30. Potential and current evolution with time for Ti6Al4V under crevice-corrosion configuration in NaCl 0.9%wt pH 2.3. Potential applied: $-0.5\text{V (V}_{\text{Ag/AgCl}})$.

The experiment carried out at -1V is represented by the potential and current evolution in Figure 4-31. In this case, no crevice-corrosion effect was observed from the current, neither a significant potential difference along the taper even though was registered during the whole measurement.

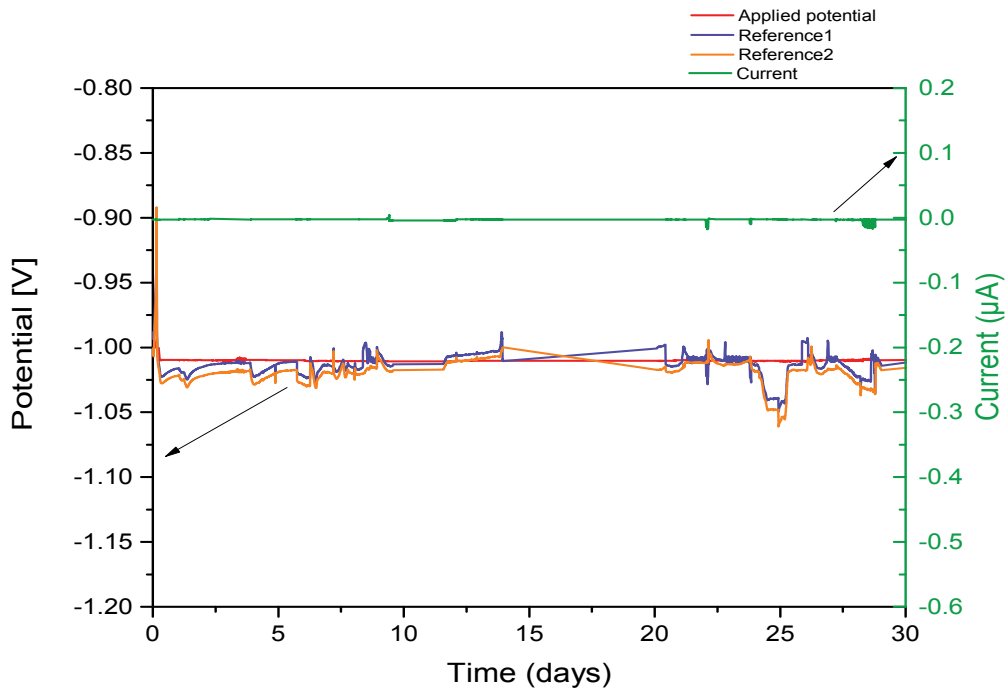



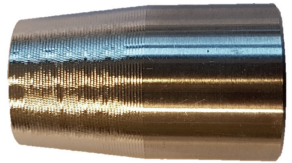

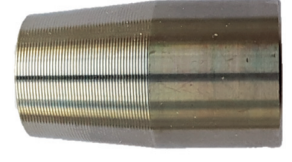
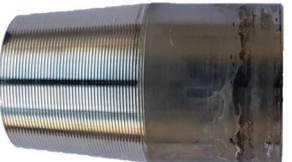
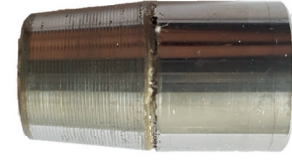
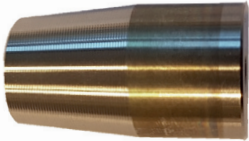

Figure 4-31. Potential and current evolution with time for Ti6Al4V under crevice-corrosion configuration in NaCl 0.9%wt pH 2.3. Potentials applied $-1\text{V (V}_{\text{Ag/AgCl}})$.

Samples evaluated under -0.5V and -1V are shown in Table 5-5. No affected areas by crevice-corrosion were found. Some conical parts (outside of the crevice) showed yellow spots that probably correspond to some counter electrode reaction but nothing on the cone thread finishing that corresponds to crevice-corrosion was observed.

4.2.4 Summary of results

- The developed crevice-corrosion experimental set-up reproduces the geometry of typical trunnions found in hip joint with a ceramic head.
- Under this configuration, Fe-Cr 15% stainless steel suffered, as expected, of evident crevice-corrosion in sulphuric acid.
- However, all the observations presented above, demonstrated that Ti6Al4V and CoCr samples kept their passive behavior under different chemical and electrochemical conditions in the crevice-configuration proposed in this work. Therefore they do not undergo crevice-corrosion under the present experimental conditions mimicking hip joints trunnions.

Table 4-5. Taper samples evaluated under the crevice-corrosion configuration during one month according to potential applied and pH solution.

| Acid Solution - pH 2.3 | | | | | | |
|---------------------------|--|---|---|---|---|---|
| CoCr | | Ti6Al4V | | | FeCr* | |
| -0.1V |  |  |  |  |  |  |
| Neutral Solution - pH 5.7 | | | | | | |
| CoCr | | Ti6Al4V | | | | |
| |  |  | | | | |

5 Crevice-corrosion model

Predicting tools able to determine under which geometrical, chemical and electrochemical parameters biomedical alloys undergo crevice-corrosion in a modular hip joint configuration are needed. In this chapter, an existing model predicting crevice-corrosion occurrence is analyzed and validated to be used in modular hip joint configuration. Finally, experimental and theoretical results are compared to validate the proposed approach.

5.1 Crevice corrosion model applied to FeCr15% system

Besides the experimental approach, IR-voltage model was considered as an appropriate tool to predict theoretically the occurrence of crevice-corrosion. However, the applicability of this model to modular hip joint configuration must be verified.

The verification of the model was done based on the obtained results from crevice-corrosion experiments carried out using FeCr15% samples, where crevice-corrosion occurred and a critical distance was identified. Meanwhile, estimation for Ti6Al4V and CoCr alloys is presented to identify under which conditions these biomedical alloys can suffer crevice corrosion.

To apply the model, current values from the crevice were extracted from the test. The current value used in the model (anodic current) was calculated by subtracting the cathodic current from the average current recorded during the test. Although, the cathodic current in the cell is unknown, estimation of this value was done based on the polarization curve. To calculate the cathodic current, the linear part of the cathodic polarization curve (logarithmic scale) close to E_{cor} was interpolated according to Tafel method and extrapolated to the selected test potential. The obtained current density was multiplied to the area immersed in the solution outside of the crevice in order to obtain the cathodic current at test potential. As the current from the crevice-corrosion test in the FeCr15% is dominated by the dissolution, the cathodic current is considered negligible, which is not the case for biomedical alloys test.

Likewise, experimental values of solution conductivity, crevice length and gap were used to verify the applicability of the model to this configuration.

Taking into account the terms in expression (8) or in its simplified version (9) in Chapter 4, some modifications according to the test had to be done. Those adjustments are explained below:

- i_{pass} was taken directly from the current density measurement at the beginning of the test. During the first few seconds, when the potential is applied, the passive layer is formed. This value was considered more adjusted to the material passivation process under the crevice – corrosion configuration.
- For an average hammering impingement of 0.040mm inside the cone, the new gap was defined as 0.63 μm .
- For FeCr15% the ratio i_{pass}/i_{max} is equal to 0.011, which is lower than 0.05 and consequently, the simplified model was used to calculate d_c according to equation (8). The parameters used to calculate the critical distance for FeCr15% under this configuration are listed in Table 5-1

Crevice length (13mm) and gap (0.6 μm) are the same values for all the materials since those values come from the cell design.

Table 5-1. Experimental electrochemical parameters used for critical distance calculation for FeCr15% in H_2SO_4 at 0.5V.

| Parameters | Values for Fe/Cr 15% |
|---------------------------------|-----------------------|
| E_{pass} (V)* | -0.3 |
| i_{pass} (A/cm ²) | 0.02×10^{-6} |
| I (A) | 5.4×10^{-6} |
| σ (S/cm) | 2.83E-02 |
| E_{ap} | 0.5 |

The critical distance, d_c , calculated through IR crevice–corrosion model is 0.11 cm, which is very close to the value found experimentally for this stainless steel evaluated in the crevice-corrosion configuration.

In conclusion, the IR crevice – corrosion model is a valid tool to predict critical distances in the crevice-corrosion configuration proposed by this work, and subsequently, to the modular hip joint configuration

5.2 IR crevice – corrosion model in biomedical alloys

Results obtained from biomedical alloys in the crevice-corrosion configuration show the resistance of the two alloys to the deterioration caused by this mechanism. As in the previous calculation of d_c some assumptions have to be done to get an estimation.

E_{pass} is an important parameter for crevice-corrosion conditions as mentioned earlier. Nevertheless, the determination of this value for biomedical alloys such as CoCr and Ti6Al4V is not straightforward, since these materials are spontaneously passive. Therefore reasonable ranges for this potential were defined according to experimental results and literature data.

Three criteria were checked to define a passive potential range: the first one corresponds to active-passive transition in the polarization curve while the second one corresponds to potentials from Pourbaix diagrams where the first oxides appear for the predominant element of the alloy and give pH. Finally, studies from the literature where active-passive transition was studied were taken into account even if those values correspond to a more severe condition.

I_c values were determined experimentally; they correspond to the anodic current estimated as was indicated in 5.1.

5.2.1 IR-Voltage model parameters

To apply the IR-Voltage model to biomedical alloys, some consideration were done:

- Even though, the i_{pass}/i_{max} ratio cannot be verified directly, because the active-passive transition was not clear in the polarization curve. The ratio was checked for Ti and CoCr alloys in other media [25], [81], [128] where clear active-passive zones were observed. In general, i_{pass}/i_{max} ratios values were lower than 0.05, which means that it is reasonable to use also the simplify expression.
- i_{pass} values were taken as previous from the experimental results when the potential is imposed under the crevice – corrosion configuration.
- Crevice-corrosion gap considered was the value determined experimentally from the geometry mimicking hip joint trunnion after hammering impingement (0.63 μm).

5.2.2 CoCr alloys

For CoCr alloys, polarization curves measured presented in Figure 4-2 show a peak from -0.7V to -0.6V (vs Ag/AgCl₂), especially for the more acidic medium. This value is close to the potential (-0.8V vs SHE) where the chromium oxides are found in acid media, according to Pourbaix diagrams of Cr [128]. In this case, the element that gives the passivity to the alloy is chromium. Likewise, Kaesche [25] reported a clear active-passive transition for Cr in 1N H₂SO₄, with a passivation potential (E_{pass}) value of -0.4V (vs SHE) and a passivation current density of $i_{pass} < 140 \mu\text{A cm}^{-2}$. If this i_{pass} is considered, the criteria i_{pass}/i_{max} could be satisfied and the critical distance can be calculated through equation (8).

Taking into account that the surface area immersed in the solution but outside the crevice is 3.08 cm² and the cathodic current density from the polarization curve, anodic currents are reported in Table 5-2.

Table 5-2. Anodic current to calculate critical distance for CoCr in NaCl 0.09%wt at 0.5V according to the solution pH

| pH | $i_{cathodic}$ (10^{-7} . A/cm ²) | $I_{cathodic}$ (10^{-7} . A) | $I_{measured}$ (10^{-7} . A) | I_{anodic} (10^{-7} . A) |
|-----|---|------------------------------------|------------------------------------|----------------------------------|
| 2.3 | -1 | -3.0 | 0.2 | 3.2 |
| 5.6 | -0.7 | -2.1 | 0.37 | 2.5 |

Based on the parameters presented in the Table 5-3, Figure 5-1(a-b) shows that the critical distances for having crevice-corrosion in CoCr tapers are above 48.7 mm in acidic media and above 51.1 mm in pH 5.6. As observed, the critical distance change as a function of the passivation potential, critical distances for CoCr under pH 5.6 reach values around 1 cm for E_{pass} values corresponding to systems under high concentrated acid solutions, which is unlikely occurring in the modular joint.

Table 5-3. Electrochemical parameters used for critical distance calculation for CoCr in NaCl 0.09%wt at 0.5V as a function of the pH solution.

| Parameters | pH 2.3 | pH 5.6 |
|---------------------------------|-----------------------|-----------------------|
| E_{pass} (V vs Ag/AgCl) | -1 to -0.6 | -1 to -0.6 |
| i_{pass} (A/cm ²) | 1.73×10^{-5} | 5.87×10^{-9} |
| I (A) | 3.2×10^{-7} | 2.5×10^{-7} |
| E_{ap} | -0.1 | -0.1 |

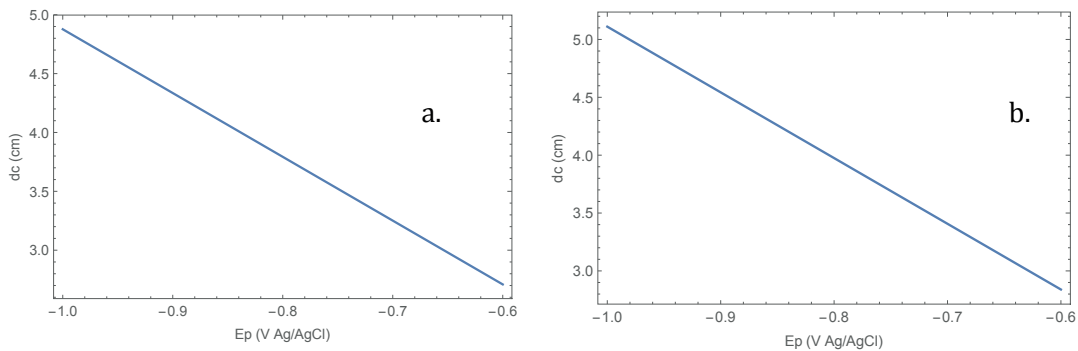


Figure 5-1. Critical distance as a function of the passivation potential of CoCr under Crevice Corrosion conditions in NaCl 0.9%wt a) pH 2.3 and b) pH 5.6. Potential applied: -0.1V ($V_{Ag/AgCl}$)

5.2.3 Ti6Al4V alloy

E_{pass} estimations for Ti6Al4V samples were done using Pourbaix diagram and data for Ti from the literature. Pourbaix diagram for Titanium [128], reports the first oxide species TiO at -1.8V (vs SHE) for pH over 5 while the transition to TiO₂ is between -0.4V and -0.6V (vs SHE) for acidic and basic solution. Likewise, an E_{pass} of -0.6V (vs SHE) for pure Ti in 0.5N, 1N, 3N and 6N H₂SO₄ is reported by Kaesche [25] while an E_{pass} close to 0V (vs Satd KCl) was found by Hosseini et al[81] for concentrations of 1M, 5M, 9M, 11M and 13 M of H₂SO₄. They also reported i_{max} from $1 \times 10^4 \mu A \cdot cm^{-2}$, then, the ratio between i_{pass}/i_{max} indicates that d_c can be calculated through equation (8).

Analogous process than those described before to calculate the anodic current were done for Ti6Al4V tests (Table 5-4).

Table 5-4. Anodic current to calculate critical distance for Ti6Al4V in NaCl 0.09%wt at 0.5V as a function of the pH solution.

| pH | $i_{cathodic}$ ($10^{-9} \cdot A/cm^2$) | $I_{cathodic}$ ($10^{-9} \cdot A$) | $I_{measured}$ ($10^{-9} \cdot A$) | I_{anodic} ($10^{-9} \cdot A$) |
|-----|--|---|---|---------------------------------------|
| 2.3 | -1 | -3.1 | 9.6 | 13 |
| 5.6 | -0.1 | -0.31 | 2.8 | 3.1 |

Possible critical distance for Ti6Al4V samples were calculated based on parameters listed in Table 5-5 for the electrolytes with pH 2.3 and pH 5.6. In all cases, critical distances calculated for both pH under passive condition are over 95 cm as Figure 5-2(a -b) indicate.

As it has been reported, in general, synovial fluid's pH is around 7 [55]. Accordingly, critical distances expected under real conditions would be close to the value obtained for pH 5.6. However, in the most optimistic case, where the E_{pass} is 0V reported for systems under high concentrated acid solutions, this distance for Ti6Al4V tapers should be around of 228 cm.

Table 5-5. Electrochemical parameters used for critical distance calculation for Ti6Al4V in NaCl 0.09%wt according to the solution pH

| Parameters | pH 2.3 | pH 5.6 |
|---------------------------------|----------------------|-----------------------|
| E_{pass} (V vs Ag/AgCl) | -1.8 to 0 | -1.8 to -0 |
| i_{pass} (A/cm ²) | 2×10^{-7} | 1×10^{-6} |
| I (A) | 1.3×10^{-8} | 3.11×10^{-9} |
| E_{ap} | 0.3 | 0.5 |

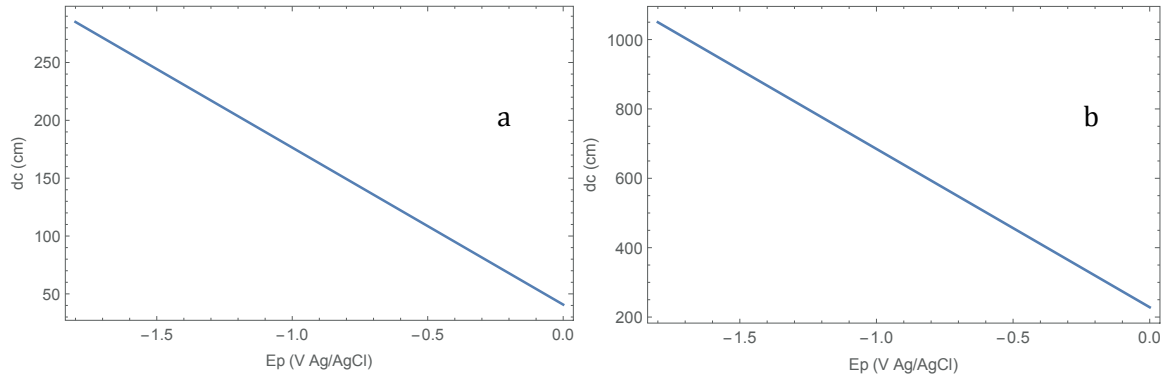


Figure 5-2. Critical distance as a function of the passivation potential of Ti6Al4V under Crevice Corrosion conditions in NaCl 0.9%wt a) pH 2.3, potential applied: 0.3V and b) pH 5.6, potential applied: 0.5V ($V_{Ag/AgCl}$)

5.3 Model extrapolation

In addition, an extrapolation of the model was done considering the following combined effects on the critical distance: the passivation potential together with the conductivity, the passivation potential with the crevice gap and finally, the combined effect of conductivity and crevice gap.

For the first case, the conductivity range considered was between the values for water (5×10^{-8} S/cm) and seawater conductivity (5×10^{-2} S/cm). Passivation potential range was kept between -1 to -0.6V for CoCr and between -1.8 and 0V for Ti6Al4V. For each material those extrapolations were done considering the highest anodic current value registered in the crevice-corrosion tests, even though this current corresponds to solutions pH 2.3.

Later, the combined effect of E_{pass} and crevice gap was done using the same values ranges than before and crevice gaps from 4×10^{-6} cm to 6×10^{-5} cm, which correspond to the mismatch angle accepted by the industry [15] and the value used in this work.

Finally, the effect of the conductivity together with the crevice gap was evaluated using ranges mentioned in the experimental conditions.

5.3.1 CoCr alloy

Model extrapolation as a function of solution conductivity and passivation potential is presented in Figure 5-3. According to this graph, crevice-corrosion takes place in distances shorter than 15mm (which is the length of the taper indicated by the green plane intercepting the graph) for the whole E_{pass} range for solution's conductivity values lower than 3×10^{-3} S/cm. At those values, the high solution resistance favors potential drop inside the crevice, leading to crevice-corrosion. However, those values are half of the lowest value reported for synovial fluids (6×10^{-2} S/cm).

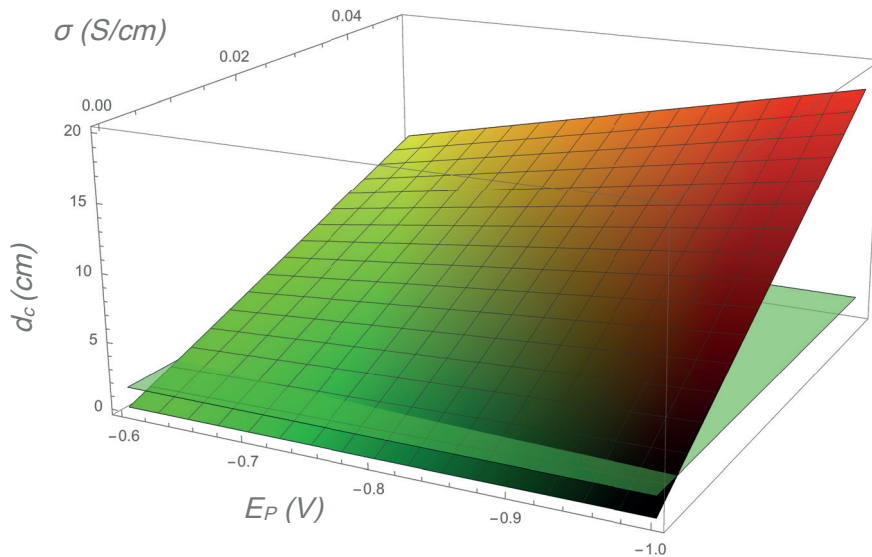


Figure 5-3. Crevice-corrosion critical distances for Ti6Al4V as a function of passivation potential and conductivity under modular head/neck configuration.

The combined effect of the passivation potential and crevice gap is graph on the critical distance is shown in Figure 5-4. To obtain critical distances shorter than 1 cm, the solution conductivity value was to be fixed in 0.01S/cm. In this case, the model predicts that under short distances ($<3 \times 10^{-5}$ cm) crevice-corrosion can occur under passivation potential values of high concentrated acid solutions.

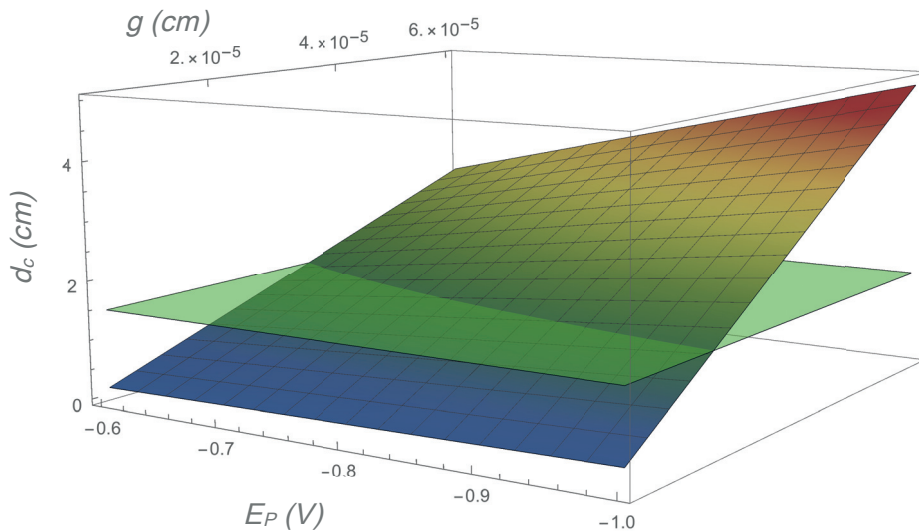


Figure 5-4. Critical distance for CoCr as a function of passivation potential and crevice gap Configuration: modular head-neck, material CoCr

Finally, to analyze the combined effect of the conductivity and the crevice gap on the critical distance an extrapolation was done as observed in Figure 5-5. Critical distances lower than 1cm are reached in all gap range only when the conductivity is lower than the 1.5×10^{-3} cm conductivity, which is lower than the value reported for synovial fluids [55].

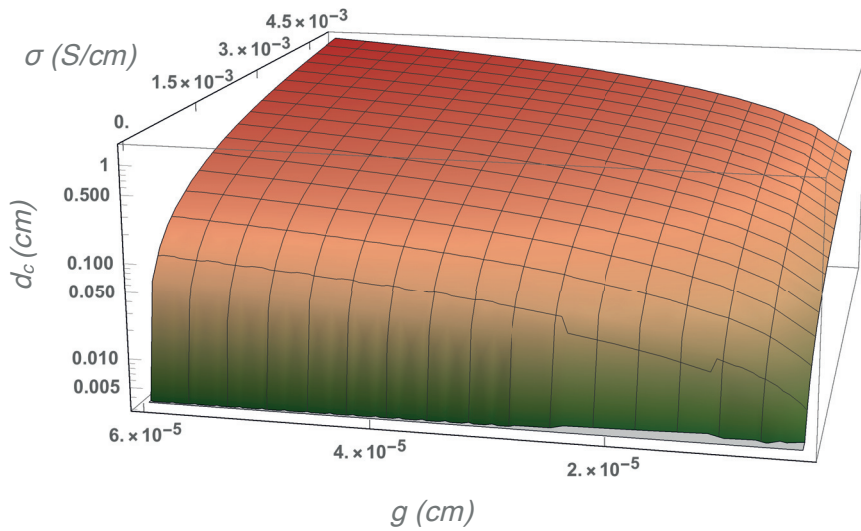


Figure 5-5. Critical distance as a function of conductivity and gap. Conductivity: 5×10^{-6} to 5×10^{-3} (S/cm), gap: 6×10^{-5} to 4×10^{-6} (cm). Configuration: modular head-neck, material CoCr

5.3.2 Ti6Al4V

Analogously to the predictions presented above, the combined effect of conductivity and passivation potential on the critical distance are presented in Figure 5-6. The effect of these two parameters does not have a visible effect at 15mm, which is the length of the taper indicated by the green plane that in this case it does not intercept the graph. In consequence, to have a closer look to the area of interest a zoom was done as Figure 5-7 shows. Critical distances are shorter than 1cm for lower conductivities than 1×10^{-6} S/cm.

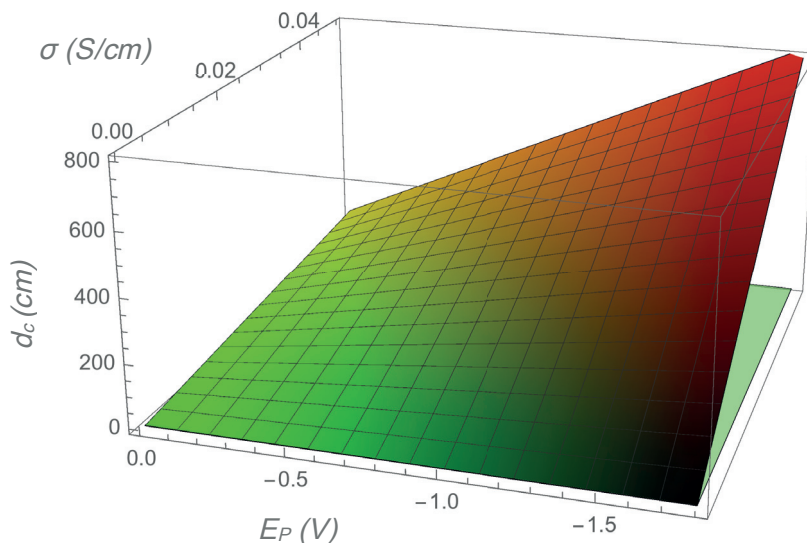


Figure 5-6. Crevice-corrosion critical distances for Ti6Al4V as a function of passivation potential and conductivity under modular head/neck configuration.

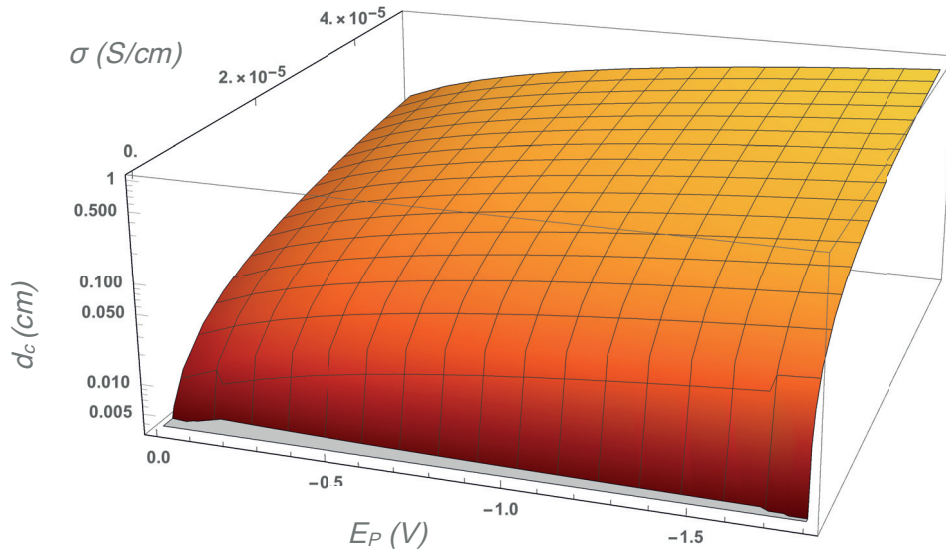


Figure 5-7. Critical distance as a function of passivation potential and conductivity. Conductivity range 5×10^{-8} to 5×10^{-6} (S/cm). Configuration: modular head-neck, material Ti6Al4V

Moreover, the second combined effect analyzed, crevice gap and passivation potential, on the critical distance is presented in Figure 5-8. In this graph, critical distances reached 3m. However, the effect of those parameters cannot be distinguished even though a plane intercepts the curve at 15mm due to the minimum critical distance is 30mm. Those values are obtained when the gap is lower than $1 \times 10^{-6} \mu\text{m}$ and for the higher passivation potentials around 0V, which is the condition for expositions to high concentrated acid solutions.

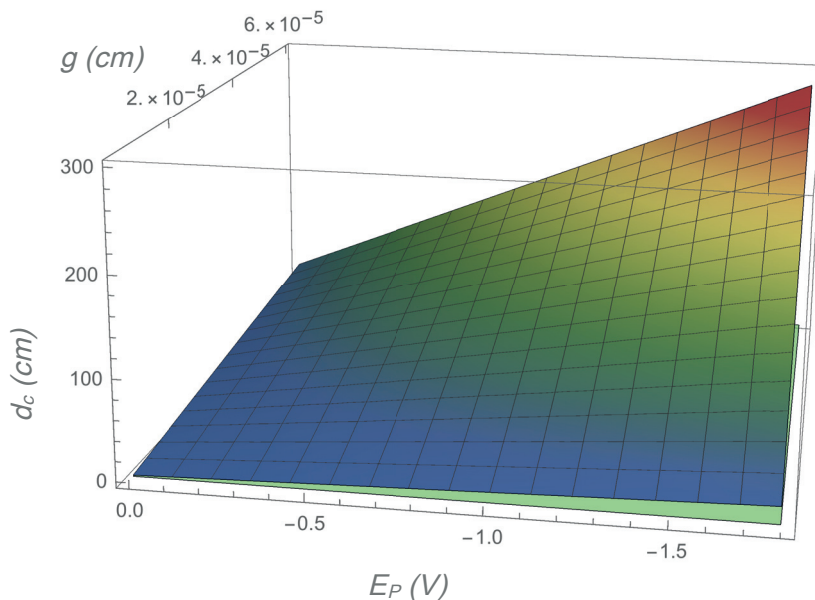


Figure 5-8. Crevice-corrosion critical distances for Ti6Al4V as a function of passivation potential and crevice gap under modular head/neck configuration.

Likewise, the critical distance for Ti6Al4V alloys as a function of the conductivity and gap shows that crevice-corrosion can occur in all the range of crevice gaps Figure 5-9. However, conductivity has to be equal to the deionized water conductivity.

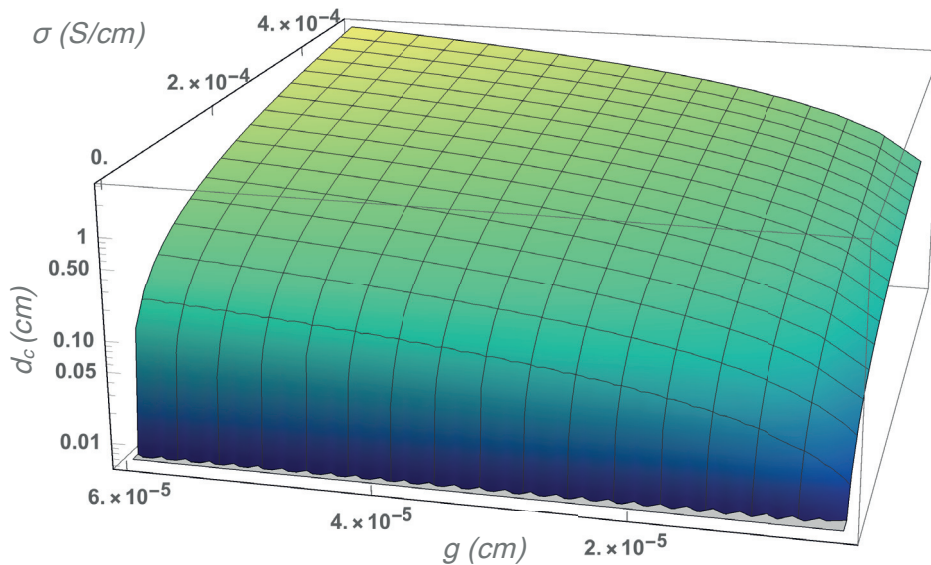


Figure 5-9. Critical distance as a function of conductivity and gap. Conductivity: 5×10^{-8} to 5×10^{-6} (S/cm), gap: 6×10^{-5} to 4×10^{-6} (cm). Configuration: modular head-neck, material Ti6Al4V

Despite of the possibility for crevice-corrosion to occur, still the critical distances calculated in all cases are higher than the trunnion dimensions.

These 3D graphs are useful tools that allow the determination of critical distances in systems where the effect of two critical parameters is considered. According to the model predictions, critical distances shorter than 1cm can be found under the combined effect of conductivity and potential as well as conductivity and crevice-gap as long as the conductivity is lower than 5×10^{-3} S/cm, which corresponds to the conductivity of sea water, and the passivation potential take values reported in literature for high concentrated acid solutions.

Based on the experimental and model results, modular hip joint configuration is a suitable geometry to crevice-corrosion occurrence. However, passivity of CoCr alloy and Ti6Al4V alloy is not affected under this geometrical configuration in a wide range of potential applied and under different pHs. There is no chemical surface activation to generate the potential cell. In other words, biomedical alloys such as Ti6Al4V and CoCr unlikely fail by crevice-corrosion conditions.

Furthermore, the IR-Voltage model adapted to the hip joint trunnion geometries is a useful tool to predict under which electrochemical (E_{ap} , E_{pass}), chemical (σ) and geometrical (g , l) conditions crevice-corrosion occurs.

5.3.3 Summary

- The IR-voltage model could accurately predict the occurrence of crevice-corrosion at a defined depth d_c as measured in the experiments.
- The model also predicts the insensitivity of CoCr and Ti alloys to crevice-corrosion in the tested set-up as observed experimentally.
- Application of the crevice-corrosion model to the limit conditions found in hip joints with ceramic heads lead to the conclusion that crevice-corrosion is mostly unlikely.

6 Fretting-corrosion experiments

Fretting-corrosion is accepted as one of the main mechanisms responsible for degradation in modular hip joint implants. Similarities on tribofilms found in retrieval studies and fretting-corrosion *In-Vitro* tests confirm that the prediction of fretting-wear rates and most important the influence of well defined parameters requires the development of a model based on well identified mechanism. This chapter presents the results of a fretting-corrosion study of Ti6Al4V alloy aimed at identified relevant chemical and mechanical mechanisms and their influence on wear. These results will serve as basis for developing the model presented in the next chapter.

6.1 Instrumentation and materials.

In-Vitro experiments were carried out in a fretting-corrosion tribometer developed by Barril et al and described in [56]. Rig configuration consists of a rigid structure, where the load is applied through the compression of a spring, which stiffness is 9.81Nmm^{-1} . Normal and tangential force applied on the system are measured using a force sensor Kistler 9251A. The displacement is imposed through a piezo-actuator, values are imposed through a voltage value fixed from LabView software in a relation $1\text{V} - 10\ \mu\text{m}$. The system is triggered to record transients and mean values at the same position, which usually is fixed at half of the displacement. In addition, an electrochemical cell is adapted to the tribometer and connected to a potentiostat to measured electrode potential and current. Average coefficient of friction and current reported are taken from the mean values taken every minute during the rubbing in the region of sliding. In the case of the average current value, the base current (current produced by the potential applied but not by the rubbing) is subtracted, since this effect does not correspond to the tribochemical action.

Material used to carry out experiments was Ti6Al4V alloy (provided by Godfellow, England) of an elasticity module of 106-114 GPa. The material was received as rods of 20 mm diameter and cut in disk of 3 mm of thickness. Surface roughness for all samples was fixed at $R_a > 0.05\ \mu\text{m}$. Alumina balls of 5mm radius and $R_q < 0.02$ were used.

After the test, surface analysis to identify the morphology of the wear track was done using a Scanning Electron Microscope Scanning (SEM), Zeiss GEMINI 300 scanning microscopy at high vacuum environment. All images were done using an acceleration voltage of 3 kV and a working distance of 6 mm.

Chemical composition in the wear track was obtained using Auger Electron Spectroscopy (AES), AUGER PHI 680 spectrometer. The acceleration voltage in the electron gun was 10 keV with a primary current of 1 μ A. Wear tracks were sputtered using Ar ions of 2keV energy on a raster of 2x2 mm or 1x1 with a sputter rate of 5 nm/min. Software used to process profiles was Multipack 9.5.

Total wear volume was measured using a 3D White Light Interferometer Smart-WLI and processed with MountainsMap® Imaging Topography version 7.0.

Micro-hardness measurements were performed using a Micro-hardness Leitz Miniload 2. A load 25 gr was applied during 15 seconds to make the indentation.

Every sample analysed by means of those techniques were cleaned after fretting-corrosion tests with distilled water and ethanol in an ultrasonic bath for one hour and half.

6.2 Experimental conditions

Fretting-corrosion tests were carried out using a tribometer shown in Figure 6-1a. The geometrical configuration used was ball on flat as represented in Figure 6-1b. All fretting-corrosion experiments were carried in NaCl 0.9%wt solution at room temperature. For the tribochemical cell, a reference calomel electrode was used (all potentials are given respect to this RE) as well as one platinum counter electrode of area 214.3 mm²

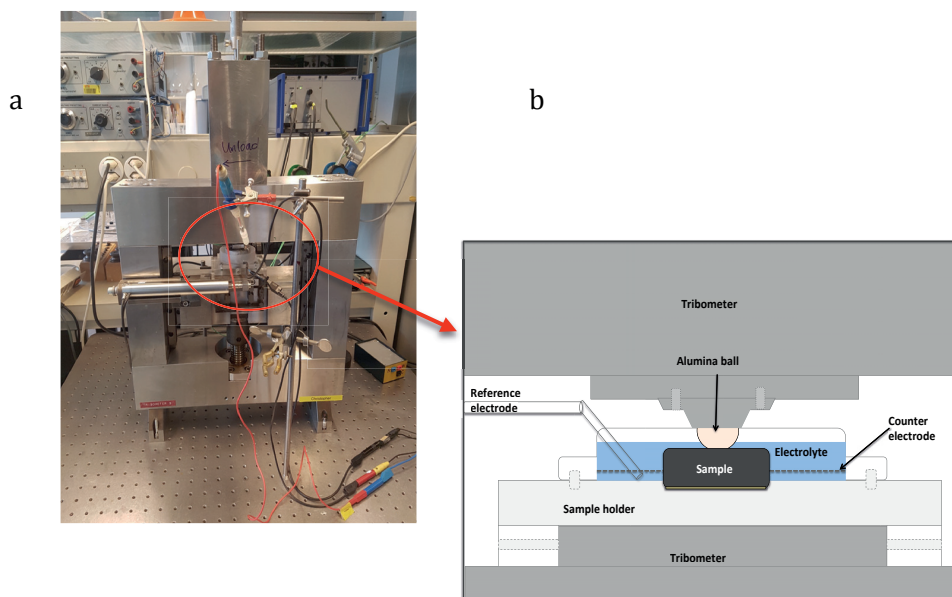


Figure 6-1. a) Fretting-corrosion tribometer, b) detail of the configuration used.

Based on previous studies where third body layers were produced (See chapter 2.2), two potentials, one anodic at 0.5V and one cathodic at -1V, were chosen. These differences in potential allow analyzing the effect of the electrochemical conditions on the third body characteristics and properties. Parameters imposed were equal in both cases: normal force (F_N) 10N, frequency 1Hz, rubbing time 3600s and amplitude displacement 50 μ m.

An additional test at 0.5V was performed with the same parameters except the normal force, which value was 30N. This experiment was performed to analyze the role of the normal load over the third body layer.

Once the contact and the load were fixed, potential was imposed during 30 min to homogenize the potential surface. Subsequently, the amplitude displacement was imposed. Variation in the normal force, tangential force, potential, displacement and current were registered during the whole experiment.

6.3 Results

To illustrate results obtained from the fretting-corrosion test Figure 6-2, Figure 6-3 and Figure 6-4 show the fretting-corrosion loops, the coefficient of friction (COF) as well as the current evolution for the Ti6AL4V/Al₂O₃ couple evaluated under a normal force of 10N and applied potential of 0.5V. Figure 6-2a-c present fretting loops evolution for systems evaluated at cathodic and anodic (under two different normal load) conditions. Every experimental condition was evaluated at least in duplicate; average results of COF and current listed in Table 6-1 correspond to the average values obtained between samples. Differences in the mechanical accommodation between experiments under different conditions are observed.

Figure 6-2a shows the fretting loops evolution for experiments carried out under an applied normal force of 10N at 0.5V. As observed, different elastic and plastic accommodation took place during the test. Initially, a friction force plateau is observed, which indicates that during the first cycles, the material was being worn significantly. Subsequently, there was a decreasing in the sliding and it seems that there was more elastic accommodation although in the final part of the experiment the loops are widened until reaching the initial size. These loop transitions correspond to the evolution observed in the coefficient of friction presented in Figure 6-3a. Increments in the COF at the beginning and at the end of the cycles were registered as observed in Figure 6-3a. Those variations correspond to changes in the fretting regime along the test.

In comparison, fretting loops obtained for the experiments carried out under 10N of normal load at -1V. Figure 6-2b shows the evolution of the mechanical accommodation under these conditions. In comparison with the system under passive potentials, more elastic accommodation is observed in the fretting loops slope. In consequence, volume of the worn material from the system evaluated under cathodic conditions must be lower. In addition, a small difference was found as well in the effective displacement, which is determined by the amplitude of the loop. It affects directly the fretting sliding

velocity reported in Table 6-1. The sliding velocity of the system is proportional to the ratio between the effective slip distance and the time for one stroke [57]. With respect to the COF evolution, a decrement was noticed for experiments performed at -1V (Figure 6-3b). Since the rubbing started, the COF was stable, which corresponds to the mechanical evolution found in loops Figure 6-2b, where none transition was observed.

Finally, a total different mechanical behavior was observed for fretting corrosion systems at anodic condition (0.5V) under higher normal load, 30N. No sliding is observed in fretting loops but the stick regime with high elastic accommodation dominates in Figure 6-2c. In this case, tangential force is lower than the normal force. Then, the ball indented the substrate surface and does not move enough to reach the sliding regime in one part of the contact. As a consequence, the effective amplitude displacement is shorter than those obtained for experiments carried out under 10N either in passive or cathodic condition. In addition, the COF registered values did not correspond to the sliding proportion of the movement, which means that it can not be compared with those taken for 10N under anodic and cathodic condition.

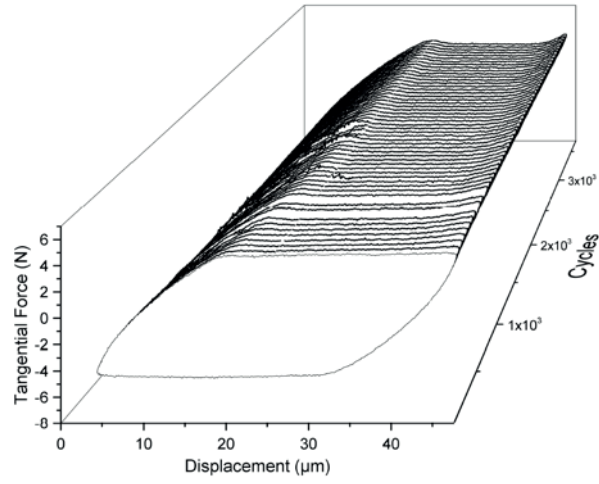
Likewise, current evolution observed in Figure 6-4 shows the initial peak corresponding to the onset of the potential. The subsequent peak of current is related to the onset of rubbing. The increment in the current is caused by the corrosion reactions (material dissolution) and the wear accelerated corrosion taking place during the rubbing.

Typically, in fretting-corrosion experiments this increment remains until the movement stops. Current values during the rubbing time are reported in Table 6-1 for every condition and they are used in the calculation of the chemical wear based on equation 12 (except in the tests at applied cathodic potential in which the measured current is negative as observed in Figure 6-4b). At -1 V, even though there is wear accelerated corrosion and material oxidation, the negative current is dominated by a superimposed cathodic reaction (water reduction).

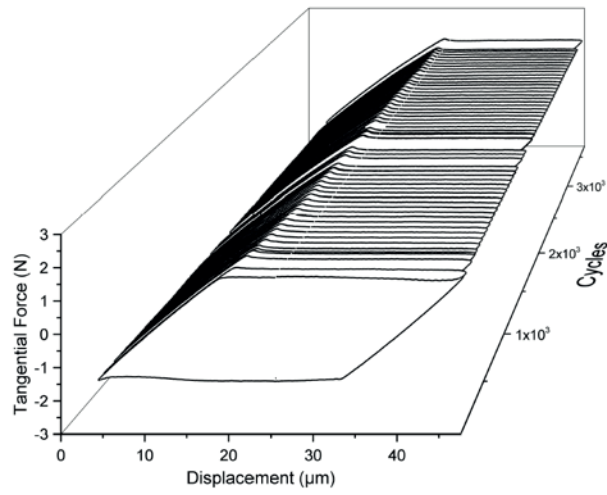
As expected, higher currents were reported for experiments carried out under applied normal force of 10 N at 0.5 V (Figure 6-4a). As was noticed from the fretting loops, sliding deformation occurs during the rubbing, which is the main source of current. In consequence, it is expected that the material surface of the samples presents higher wear compared to the others.

Current values registered under anodic conditions at higher load (30N) are lower compared to the current measured at 10N, Figure 6-4. Even though, a significant increase in the current was observed when the potential was applied, but no changes were noticed with the onset of rubbing due to the absence of sliding during the mechanical accommodation. This agrees with previous studies where changes in current were related to sliding regimes [108].

a



b



c

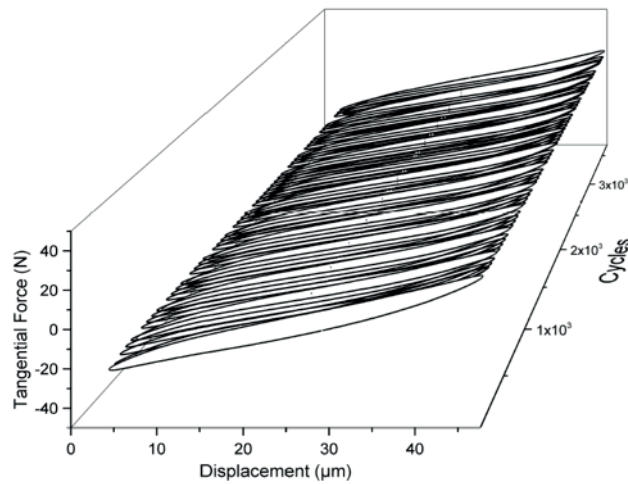


Figure 6-2. Fretting-corrosion loops Ti6Al4V/ Al_2O_3 couple for samples evaluated under a) normal force 10N at 0.5V, b) normal force 10N at -1V and c) normal force 30N at 0.5V. Experimental conditions: amplitude displacement 50 μm , frequency 1Hz in NaCl 0.9%wt.

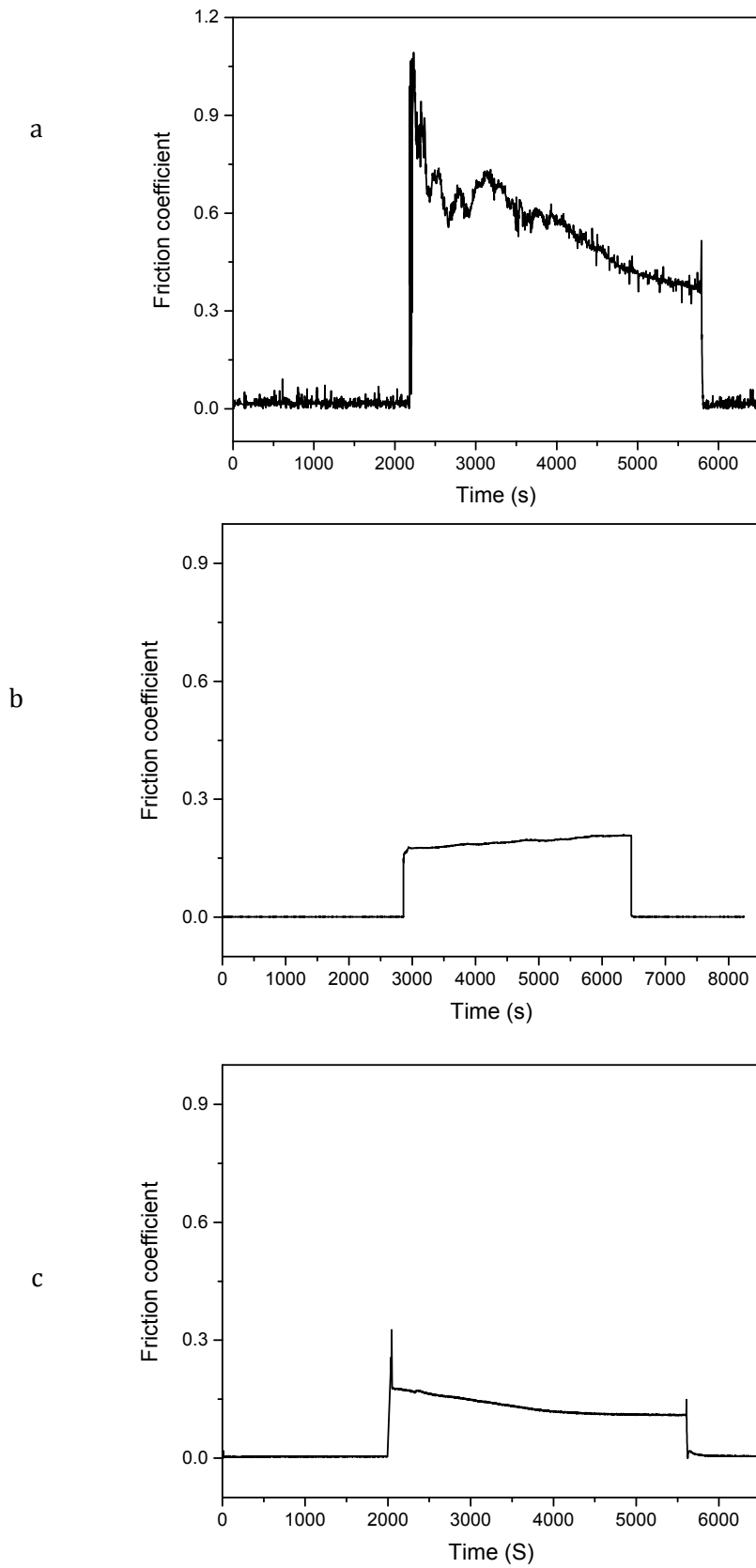


Figure 6-3. Coefficient of friction of Ti6Al4V/Al₂O₃ Ti6Al4V/Al₂O couple for samples evaluated under a) normal force 10N at 0.5V, b) normal force 10N at -1V and c) normal force 30N at 0.5V. Experimental conditions: amplitude displacement 50μm, frequency 1Hz in NaCl 0.9%wt.

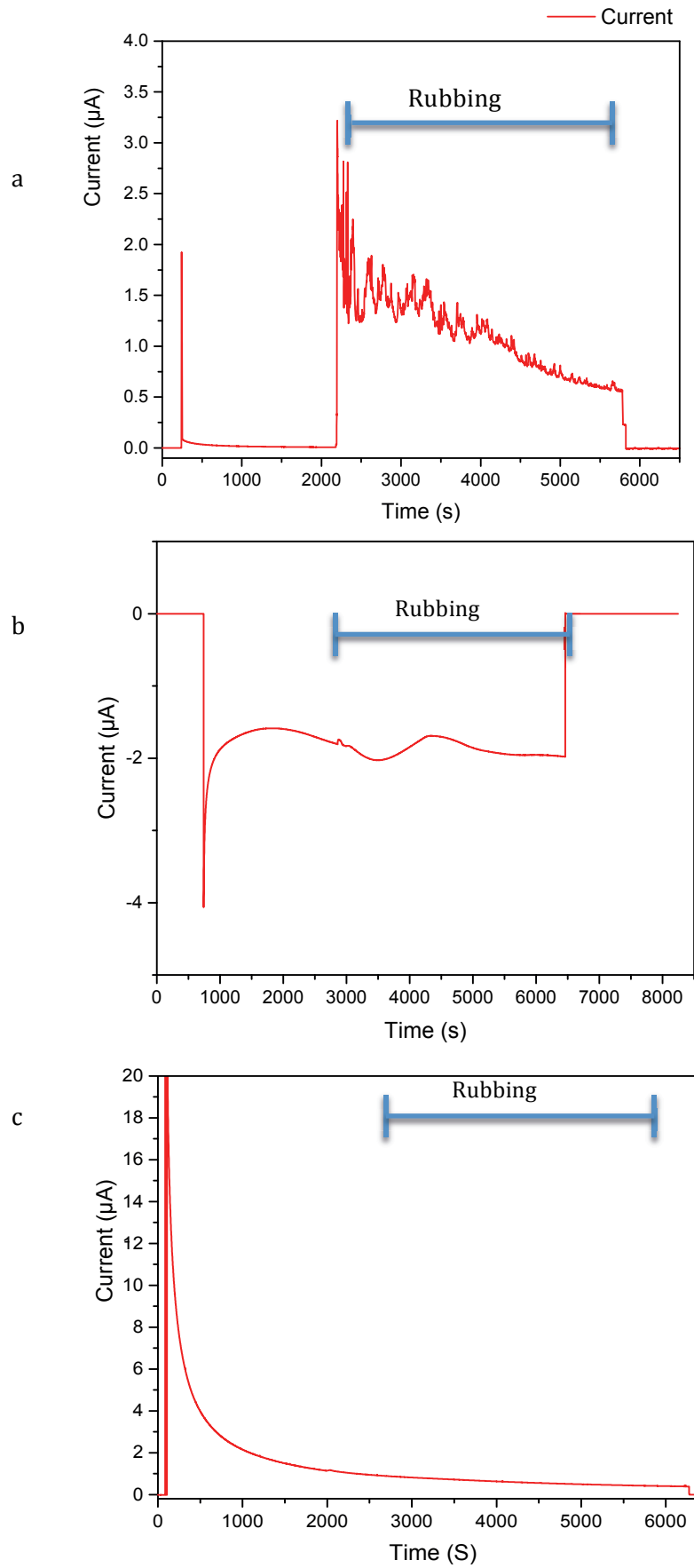


Figure 6-4. Current evolution during a fretting-corrosion test of Ti6Al4V/ Al_2O_3 couple for samples evaluated under a) normal force 10N at 0.5V, b) normal force 10N at -1V and c) normal force 30N at 0.5V. Experimental conditions: amplitude displacement $50\mu\text{m}$, frequency 1Hz in NaCl 0.9%wt.

Finally, material volume worn during the fretting test was measured on the wear track by interferometry. The profilometer images of the wear track from the three experiments are presented in Figure 6-5a-c.

Wear tracks obtained under a normal force of 10N at passive condition were bigger than those obtained under cathodic conditions, as was expected. This indicates that wear during the same time was higher under the anodic condition (0.5V) as data from the total volume worn confirmed.

No significant wear is observed in the samples tested under anodic conditions at 30N, which corresponds to the behavior reported in Figure 6-2c, where no sliding was observed.

Clearly, wear tracks are noticeable different for the three conditions evaluated. However, to understand and analyze in a detailed approach differences on the contact area between the cathodic and the anodic condition, surface analysis needed to be done. The condition under 30N was not checked because the wear was not significant compared to results under 10N.

Finally, Table 6-1 presents a summary of the experimental conditions and observables.

Table 6-1. Fretting-corrosion experiments observables

| Parameter | 0.5V | | -1V |
|--|-----------------|-------------------|-----------------|
| Normal force, F_N (N) | 10 | 30 | 10 |
| Effective displacement (μm) | 25 \pm 2 | 2 \pm 0 | 20 \pm 6 |
| Sliding velocity (m/s) 1×10^{-05} | 5.0 | 0.4 | 4.0 |
| COF | 0.55 \pm 0.06 | 0.095 \pm 0.045 | 0.21 \pm 0.09 |
| Current (μA) | 1.24 \pm 0.23 | 0.27 \pm 0.001 | -1.46 \pm 0.5 |
| Chemical wear (cm^3) 1×10^{-07} | 1.25 | 0.00272 | - |
| Total wear (cm^3) 1×10^{-08} | 13,3 \pm 2.6 | 15.5 \pm 0.04 | 1.07 \pm 0.29 |

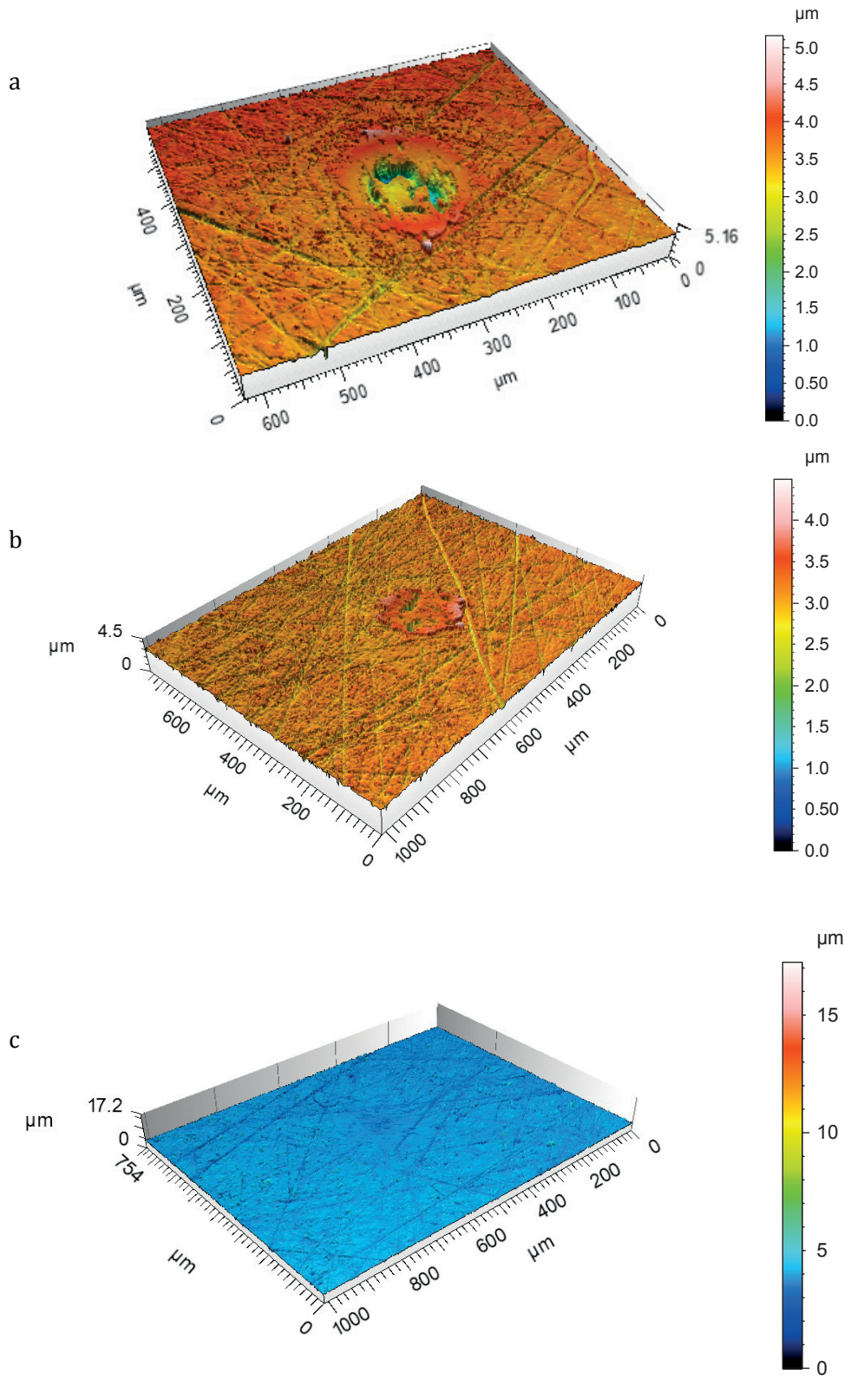


Figure 6-5. 3D image of the wear track after fretting-corrosion test of Ti6Al4V/Al₂O₃ couple for samples evaluated under a) normal force 10N at 0.5V, b) normal force 10N at -1V and c) normal force 30N at 0.5V. Experimental conditions: amplitude displacement 50μm, frequency 1Hz in NaCl 0.9%wt.

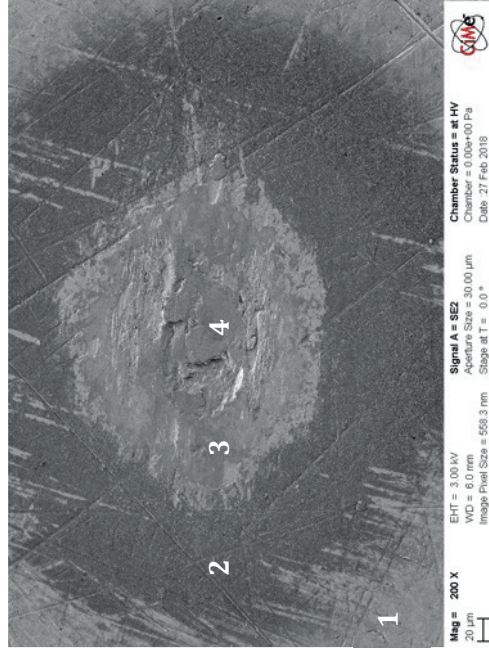
6.4 Surface characterization

6.4.1 Anodic conditions (0.5V)

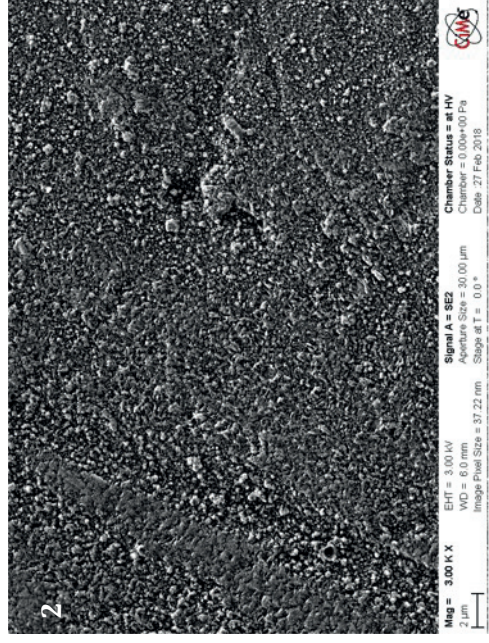
Surface characterization of the wear track from the fretting-corrosion experiments is presented in Figures 6-6 a-d. From the wear track overview it is observed that an important part of material has been removed. Besides four regions can be identified as observed in Figure 6-6a. The difference between those regions is discussed below.

The first zone corresponds to the base material, which was not exposed to fretting-corrosion and between this area and the wear track a sort of ring is noticed (2nd region). SEM image (Figure 6-6b) focused in this region reveals that this dark ring is formed by small debris particles ejected from the contact.

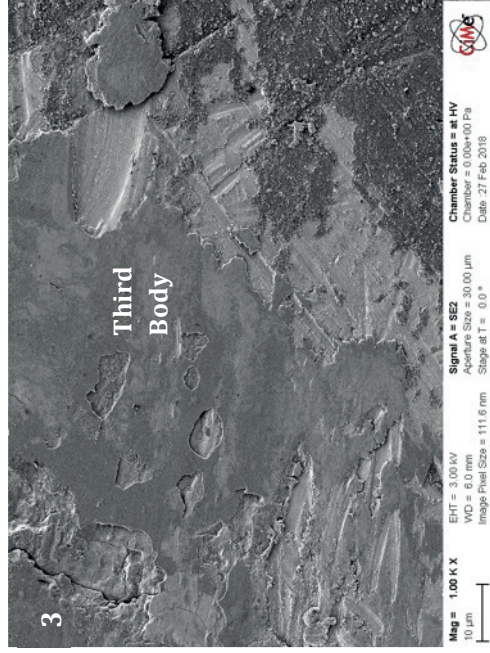
A closer examination on the wear track revealed the presence of a deformed and smeared thin third body layer in the most external parts of the wear track (region 3) as well as in the center, where the region 4 is located. Figure 6-6c-d shown the tribofilm formed on the surfaces, as well as some spots where the alloy is exposed (third body free) and debris particles. Indeed, a big particle detached is observed in the upper part of Figure 6-6c. One particle of this size is fragmented and broken while rubbing in progress, which generated smaller debris particles that either are ejected from the contact or remain on it to be re-incorporated to the third body layer by deformation and mixture with material on the surface.



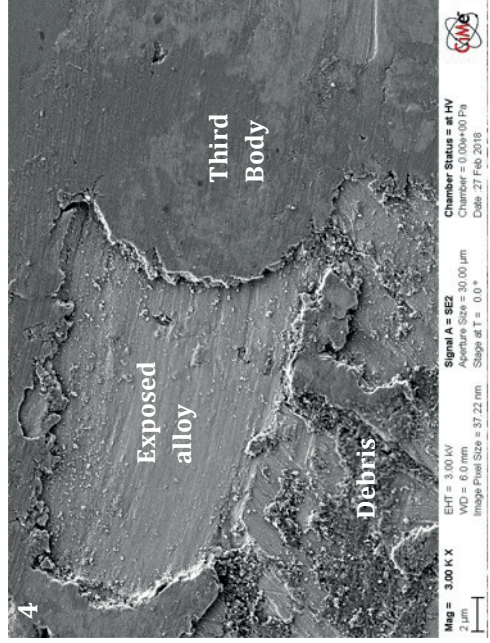
a



b



c



d

Figure 6-6. SEM images of a) a wear track after fretting-corrosion test, b) debris particles, c) third body layer and d) third body layer and debris particles inside of the wear track. Experimental conditions: normal force 10N, amplitude displacement 50µm, and frequency 1Hz in NaCl 0,9%wt at 0.5V.

Subsequently, to characterize the thickness of these layers, 3D profilometry was done inside the wear track. To determine the thickness in the area shown in Figure 6-7, vertical distance was measured from the surface the areas with respect to the third body and the vertical distance from the surface, where the third body is, to the exposed alloy. The difference between those distances corresponds to the layer thickness. From Table 6-2, values obtained from the third body thickness at 0.5V are approximately between 1 μ m and 2.2 μ m).

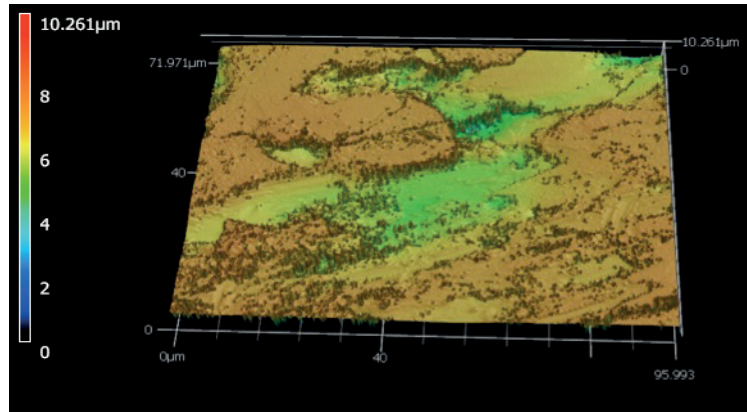


Figure 6-7. Wear track 3D image after fretting-corrosion test. Experimental conditions: normal force 10N, amplitude displacement 50 μ m, and frequency 1Hz in NaCl 0.9%wt at 0.5V.

Table 6-2. Vertical distance from the top of the surface to third body layer and to the exposed alloy inside the wear track. Conditions: normal force 10N, amplitude displacement 50 μ m, and frequency 1Hz in NaCl 0.9%wt at 0.5V.

| Measured point | Vertical distance from the surface (μ m) | | |
|--|---|------|------|
| | From the surface to the exposed alloy | 2.37 | 3.94 |
| From the surface to the third body layer | 1.31 | 1.79 | 1.74 |

Furthermore, a chemical characterization of the third body layer and debris particles was done by Auger analysis. An area of 2x2mm was sputtered during 20 min with an approximated rate of 5 nm/min. Chemical composition of selected points is listed in Table 6-3 together with three profiles to graphically illustrate the differences (Figure 6-8a-c) among eleven points indicated in Figure 60a. Three types of areas can be distinguished: Oxidized third body points 1 to 4, metallic third body points 5 and 6 and debris particles (point 7 to 11).

Finally, to obtain a proportion of the oxidized and metallic particles in the third body, Auger mapping was done in the same area. Figure 6-9b and Figure 6-9c correspond to Oxygen and Titanium map, respectively. As observed, regions rich in oxygen where the third body is more oxidized (around 60% of the area evaluated) can be discriminated

from those regions where the friction film is metallic after 100nm of sputtering. Furthermore, a second Auger map done on the wear track of a second sample evaluated under same conditions. Figure 6-10 a-d shows the oxygen evolution map as a function of the sputter depth. As observed after 50 min of sputtering at 5 nm/min and 50 additional min at 20 nm/min, oxygen was still found in some areas of the third body.

Table 6-3. Atomic concentration of third body layer and debris particles in the wear track after sputtering.

| Profile Composition | | Point | O% | Ti% |
|---------------------|--|-------|----|-----|
| Oxidized third body | | 1 | 59 | 41 |
| | | 2 | 67 | 33 |
| | | 3 | 50 | 50 |
| | | 4 | 57 | 43 |
| Metallic third body | | 5 | 8 | 92 |
| | | 6 | 7 | 93 |
| Debris particles | | 7 | 33 | 68 |
| | | 8 | 38 | 62 |
| | | 9 | 44 | 57 |
| | | 10 | 55 | 45 |
| | | 11 | 55 | 45 |

Figure 6-8. Profiles composition of a) oxidized third body, b) metallic third body and c) debris particles

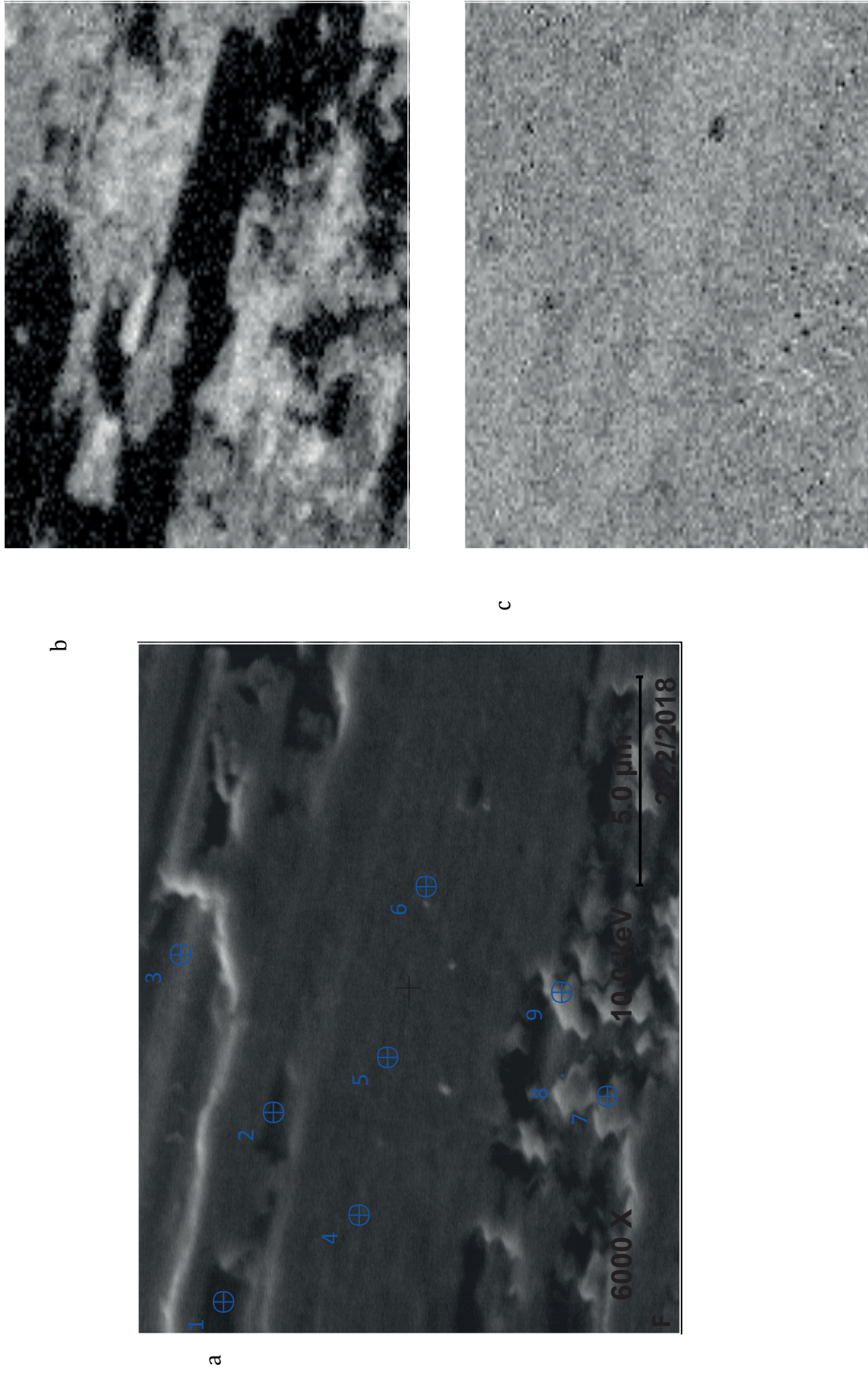
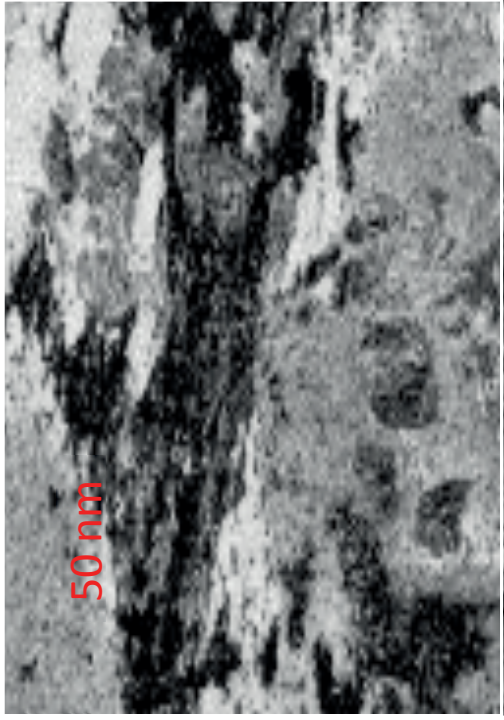
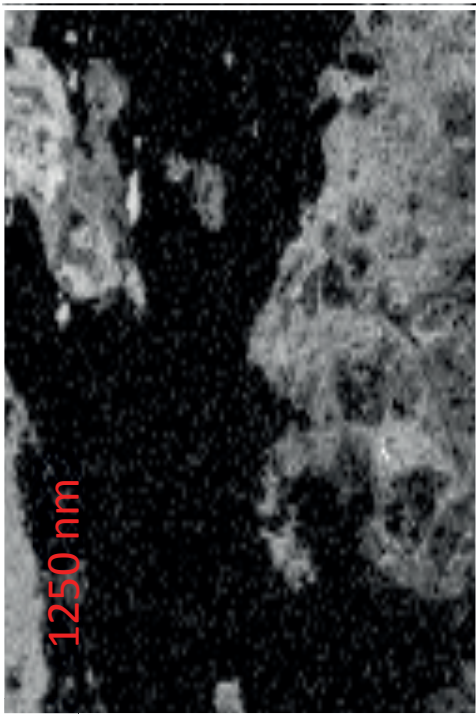


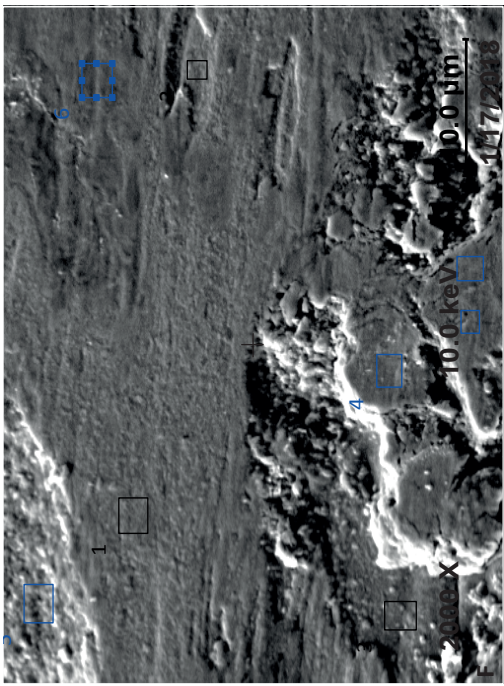
Figure 6-9. a) SEM micrograph of a third body layer and debris particles inside of a wear track. Auger maps of the area b) Oxygen, c) Titanium. Experimental conditions: normal force 10N, amplitude displacement 50μm, and frequency 1Hz in NaCl 0.9%wt at 0.5V.



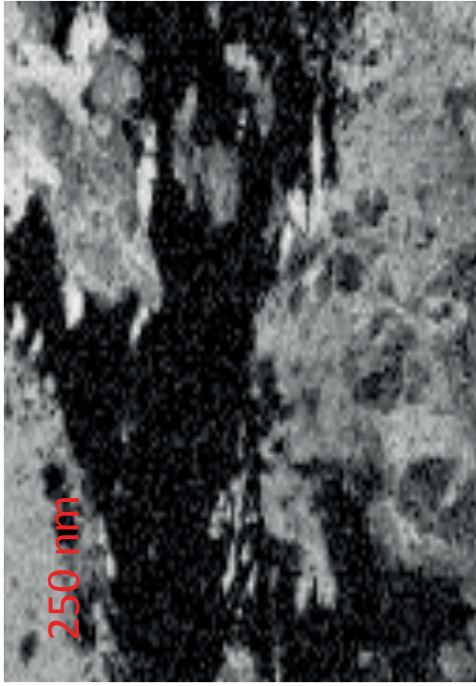
b



d



a



c

Figure 6-10. SEM micrograph of the oxygen map of the third body layer inside of a wear track. Those Auger maps are function of the sputter depth a) original surface, at b) 50 nm, c) 250nm and d) 1250nm

6.4.2 Cathodic conditions (-1V)

Characterization of samples evaluated under fretting-corrosion in cathodic condition reveals the formation of a third body layer as it was reported above for anodic conditions. In spite of the similarities between layers formed in both conditions such as the presence of debris particles outside and inside the contact some difference on the morphology and in the characteristics of the layer were found.

As observed in Figure 6-11a, a dark ring was found also outside of the contact. However, the thickness of that ring and the distance to the contact is lower compared to the debris ring formed under anodic conditions. This difference lies in the amount of material worn from the contact, being significantly lower under the cathodic condition.

Furthermore, a thicker third body layer is formed at -1V as observed in Figure 6-11c and Figure 6-11d compared to the layer generated under anodic condition. While in that case the thin layer was clearly smeared and deformed, the third body observed under cathodic condition is also deformed but some cracks are observed.

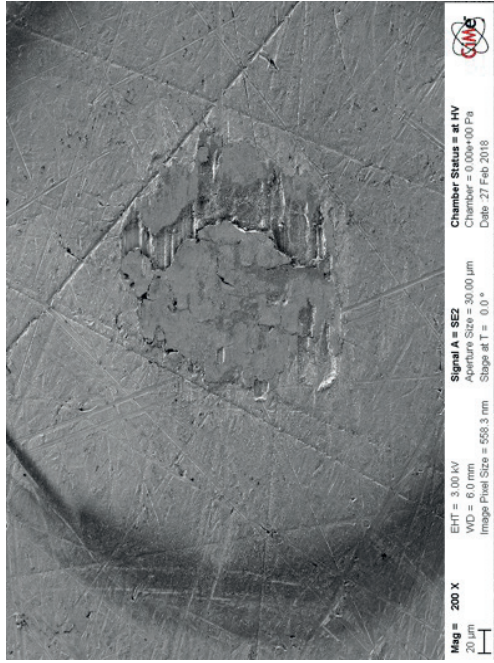
In general, the morphology of the third body layer under cathodic conditions differs from the observations under anodic conditions. Not only in the thickness but also in the failure mode. Third body edges are sharp compared to those observed under anodic conditions that seems to be more smeared.

From experiments at -1V, debris particles are also observed inside the wear track. However, they seem to be in lower proportion compared to the anodic condition.

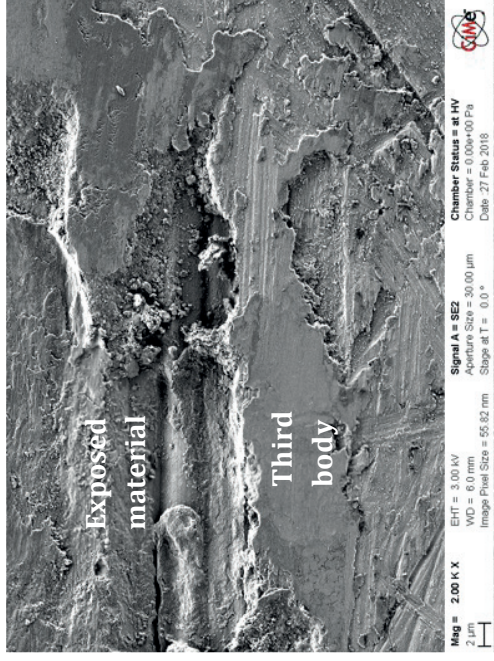
Measurements of layer thickness were done following the same procedure as described earlier for anodic conditions. In the wear track shown in Figure 6-12, height differences between the lowest points where the substrate is exposed and the third body layers (Table 6-4) indicate that the thickness of this tribofilm is above 2.5 μm (3.3 μm to 2.7 μm), which is higher compared to values obtained in layers obtained under anodic conditions.

Table 6-4. Vertical distance from the top of the surface to third body layer and exposed alloy inside the wear track from samples evaluated at -1V.

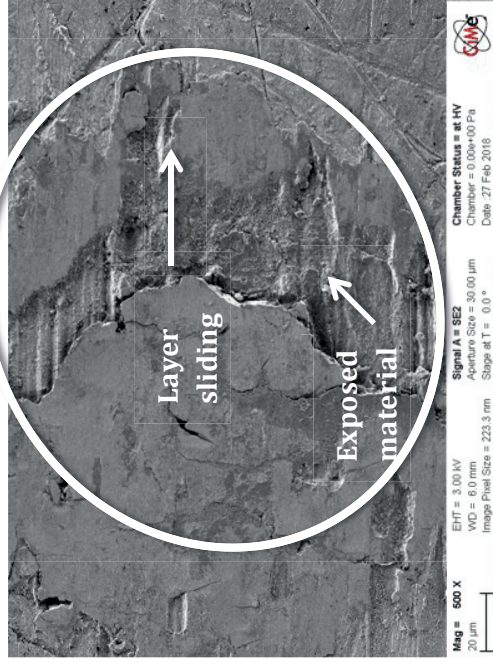
| Measured point | Vertical distance from the surface (μm) | | |
|------------------|--|------|------|
| Exposed alloy | 4.21 | 3.67 | 4.09 |
| Third body layer | 1.39 | 0.42 | 1.35 |



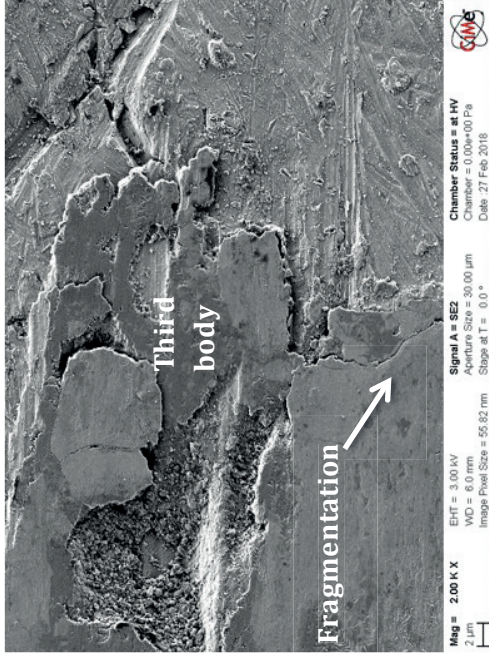
a



b



c



d

Figure 6-11. SEM images of a) a wear track after fretting-corrosion test, b) debris particles, c) third body layer and d) third body layer and debris particles inside of the wear track. Experimental conditions: normal force 10N, amplitude displacement 50µm, and frequency 1Hz in NaCl 0.9%wt at -1V.

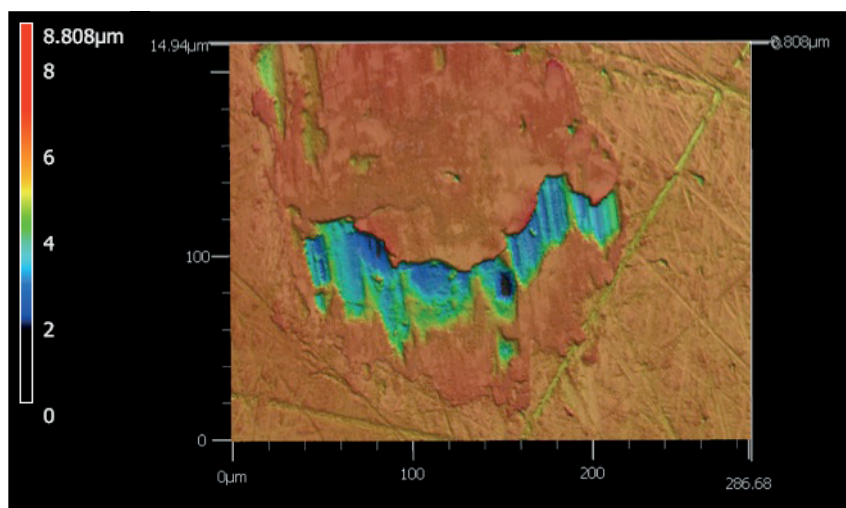
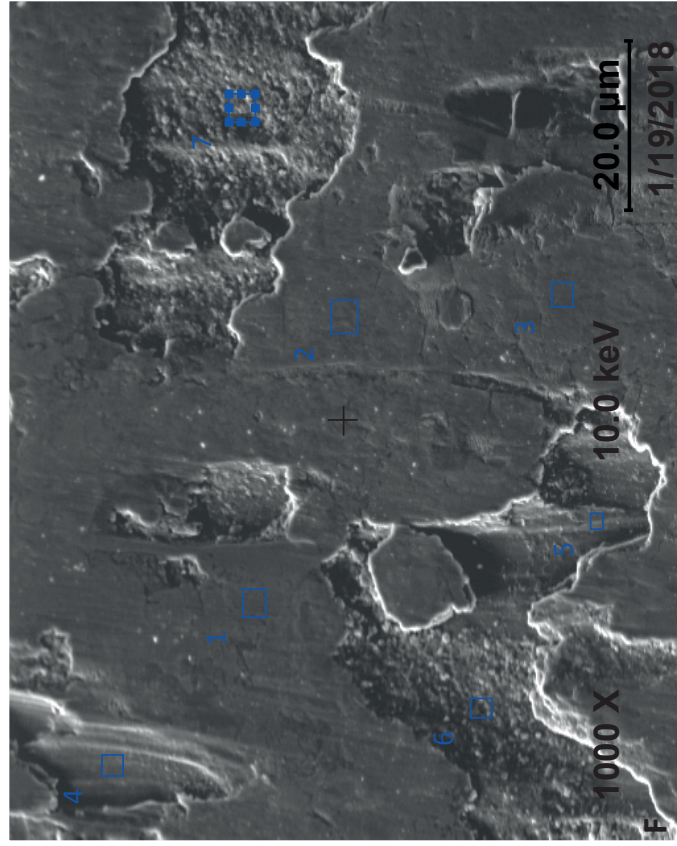


Figure 6-12. Wear track 3D image after fretting-corrosion test. Experimental conditions: normal force 10N, amplitude displacement 50 μ m, and frequency 1Hz in NaCl 0.9%wt at -1V.

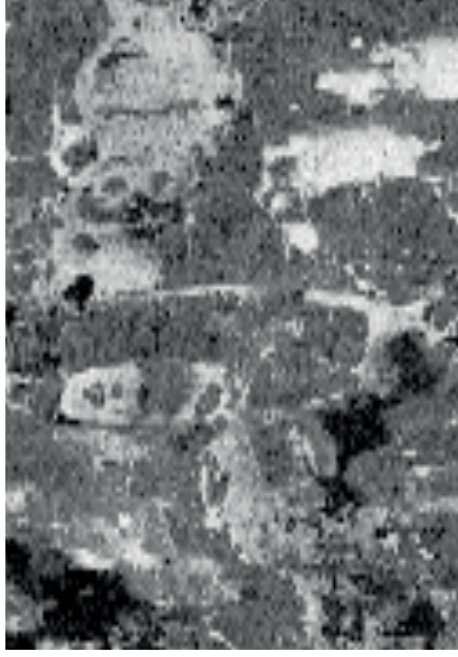
Auger profiles were carried out in 6 points on the third body layer and on the debris regions indicated in Figure 6-13a. All points taken on the third body layer (points 1 to 3) exhibit a certain oxidation degree. The chemical composition of the debris (points 4 to 6) shows that those particles are also oxidized. Values are presented in Table 6-5 together with one profile to graphically illustrate the elements proportion in depth (Figure 6-14).

In addition, Auger mapping was done on the layer, Figure 6-13b and c, showing the extension of the oxidized third body. Not defined metallic third body area was found, which differs from the third body formed under anodic condition where both third bodies, oxidized and metallic, were found. Under these considerations, it is suggested that at -1V, particles worn from the substrate remain a longer time in the contact getting a more homogenous oxidation degree and thicker third body film under cathodic conditions compared to the layer formed at anodic conditions.

a



b



c



Figure 6-13. a) SEM micrograph of a third body layer and debris particles inside of a wear track. Auger maps in the area b) Oxygen, c) Titanium. Experimental conditions: normal force 10N, amplitude displacement 50μm, and frequency 1Hz in NaCl 0.9%wt at -1V.

Table 6-5. Atomic concentration of third body layer and debris particles in the wear track

| Area | | Point | Ti% | O% |
|---------------------|--|-------|-----|----|
| Oxidized third body | | 1 | 55 | 40 |
| | | 2 | 55 | 40 |
| | | 3 | 55 | 38 |
| Debris particles | | 4 | 52 | 40 |
| | | 5 | 60 | 35 |
| | | 6 | 50 | 41 |

Figure 6-14. Profiles composition of a) oxidized third body, b) metallic third body and c) debris particles

Finally, micro-hardness measurements were done on wear tracks. Micro-hardness values obtained inside of the wear track are listed in Table 6-6 corresponding to the third body layers formed under cathodic and anodic conditions. The differences in the micro-hardness depending on the prevailing electrochemical conditions can be associated to the oxidation degree of the third body, which is higher for third body layers produce in cathodic potentials.

Table 6-6. Micro-hardness test inside the wear track after fretting-corrosion test respect to the applied potential vs SCE

| Potential applied (V) | Microharness (HV) | |
|-----------------------|-------------------|-------|
| 0.5 | 126.8 | 111.2 |
| -1 | 140.2 | 149.2 |

6.4.3 Acting mechanisms

Differences in chemical composition, failure morphology, thickness and mechanical properties of the third body may have a direct relation to the wear rate of both systems. At 0.5V, a higher amount of material is worn and ejected from the contact, in consequence even if a third body layer is formed, it is quickly worn. On the contrary, under cathodic conditions, material accumulates and forms a thicker layer. Therefore, the question can be focused on which are the differences in the phenomena causing this dissimilarity in the wear rate. Probably, the difference lies on the effect of the applied potential on the particle oxidation degree, which in turn could affect the surface energy of those particles and therefore they agglomeration or wear.

SEM images presented in Figure 6-15a and b show broken particles next to third body layers obtained from Ti6Al4V sample tested under fretting-corrosion conditions in 0.9%wt NaCl solution at 0.5V_(Ag/AgCl) and -1V, respectively. However, currently it is not possible to distinguish between the particles proportion is ejected from the contact and the amount that are reincorporated. Surface images show that the proportion of the particles re-deposited on the wear track is considered negligible compared to total wear (dark ring around the wear track).

In addition, several studies [129]–[132] have reported changes in the surface energy and in the charge of titanium surfaces with respect to the formed oxide, particle size or surface characteristics. Then, small differences in the particles (size, oxidation degree, surface energy, among others) could make them being ejected from the contact. The study of debris particles properties is beyond the objective of this work. However, this evidence can motivate future studies about the physical characteristics of particles, such as surface energy or repulsion forces, produced under different electrochemical conditions. This would contribute to explain the difference in the amount of material that is ejected from the contact.

In addition, some clue about the role of thick layers is given in Figure 6-11c. Let's focus in the highlighted region with a white circle. In the central part, a part of the substrate material is exposed and surrounded by a third body layer at the left and the right side. Broken edges of the lateral layers seem to match perfectly (see borders pointed with the white arrow). It suggests that during the rubbing, the third body layer could slide over the metal exposed, and then a metal on metal sliding contact is produced. This can be a hypothesis about the evolution of the COF registered in this sample.

Furthermore, with respect to the failure mode and based on SEM images, the third body edges of samples evaluated under -1 V seem to be sharper, which suggests that the third body layer formed under cathodic conditions may be harder as also confirmed by the microhardness measurements performed inside the wear track

Experimental results showed that mechanical and electrochemical parameters govern the third body layer properties. The nature of this tribofilm plays a role in the tribochemical

behavior of systems under fretting-corrosion conditions, which constitutes a step forward towards the understanding of deterioration in modular hip implants caused by fretting-corrosion

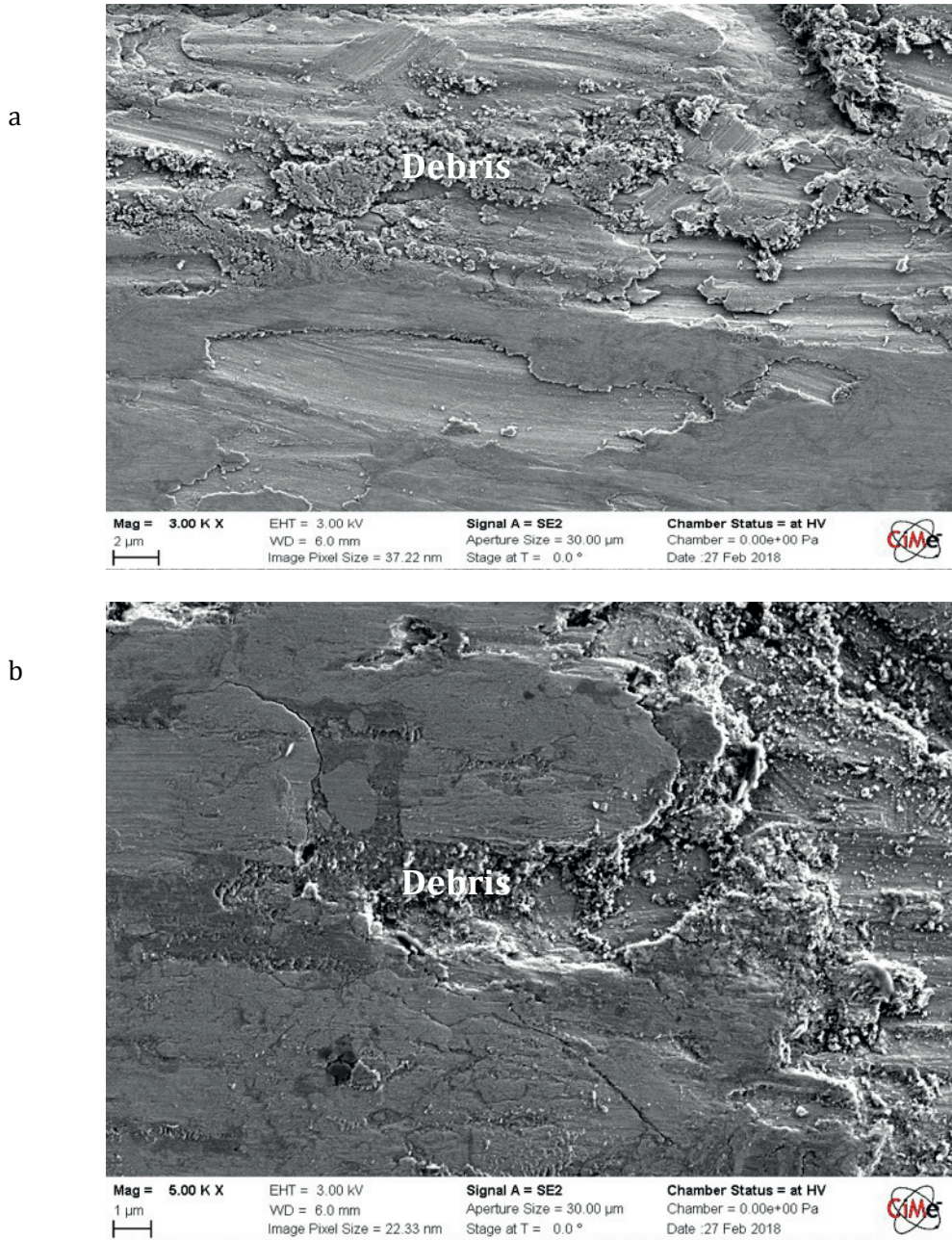


Figure 6-15. Third body layer and debris particles on the wear track of Ti6Al4V sample after fretting-corrosion test under a) 0.5V and b) -1V. Experimental conditions: Normal force 10N; amplitude displacement 50 μ m; frequency: 1Hz and applied.

7 Third body model

Based on experimental results presented in previous chapter, mechanical and chemical conditions govern third body properties. Indeed, it was observed a clear difference in the oxidation degree, thickness and hardness between layers generated under different electrochemical conditions. Then, the next description step consists in the proposition of a theoretical frame, which integrate electrochemical and mechanical parameters that influence the third body build up. A third body model is proposed in this chapter adapted to fretting-corrosion conditions. In addition, predictions of total wear rate are obtained from the model and compared with results from In-Vitro fretting corrosion.

7.1 Physical model

The model proposed in this work is inspired by the model proposed by Guadalupe et al [62] reviewed previously in chapter 2.3.3. Flows are associated to the role that plays the composition in the properties of the third body layer so in the tribocorrosion behaviour of the system. The effect of the third body layer on the wear rate was investigated by Barril et al [57], [58]. They found that wear rates were higher under anodic than in cathodic polarization condition.

According to experimental results obtained in chapter 6, the build up process, properties and the role that the body play in the contact are function of several mechanical and electrochemical factors. To illustrate the third body build up process, a physical model is proposed in Figure 7-1(a-c).

Initial state: A ball on flat fretting configuration under small amplitude movements, load and in presence of an electrolyte are under a tribochemical process. Due to the rubbing, metallic and oxidized particles from bulk material and the passive layer, respectively, are detached.

Third body layer formation: Under fretting conditions, the contact area is a confined space where those particles get trapped into the interface, being exposed to wear,

corrosion and deformation. This deformation and mixture of those particles drives to a third body layer formation as Figure 7-1b shows.

Third body layer deformation: Once the layer is formed is also subjected to the mechanical action, which produces crack propagation and fragmentation (Figure 7-1c) as was observed in experimental results.

These fragmented particles either are ejected from the contact or are reincorporated to the third body. Therefore, particles leaving the contact are considered worn material while the particles that remain in the contact are called the *redeposition*. Figure 7-1d described these material flows.

Third body layer oxidation: Besides the mechanical process, the third body gets oxidized as well. Those metallic particles in the third body film get in contact with the electrolyte and become in oxidized particles, changing the initial proportion of metal/oxide in the layer. In consequence, electrochemical reactions taking place inside the third body have to be considered as well.

As observed in the experimental results, the third body layer (also known as friction films) modifies the velocity and normal force distribution in the contact. It means that a brittle and rigid friction film (cathodic) modifies the distribution of the applied force in a different proportion than a soft layer (anodic); in consequence wear rates can be different.

In previous studies [62], [133] the mechanical effect of the third body in the system was considered and defined as the attenuation factor. Although, it is known that this effect depends on the third body layer thickness, which in turn depends on the electrochemical conditions, none mechanical expression has been found to describe this attenuation factor.

According to the physical model described above, a model describing wear is proposed in this chapter. This model is based on material flows, which in turn take into account critical mechanical and electrochemical parameters. This wear is related directly with the third body build up process. In addition, an expression to calculate the mechanical effect of the third body in the system in terms of the mechanical properties of this layer is also developed.

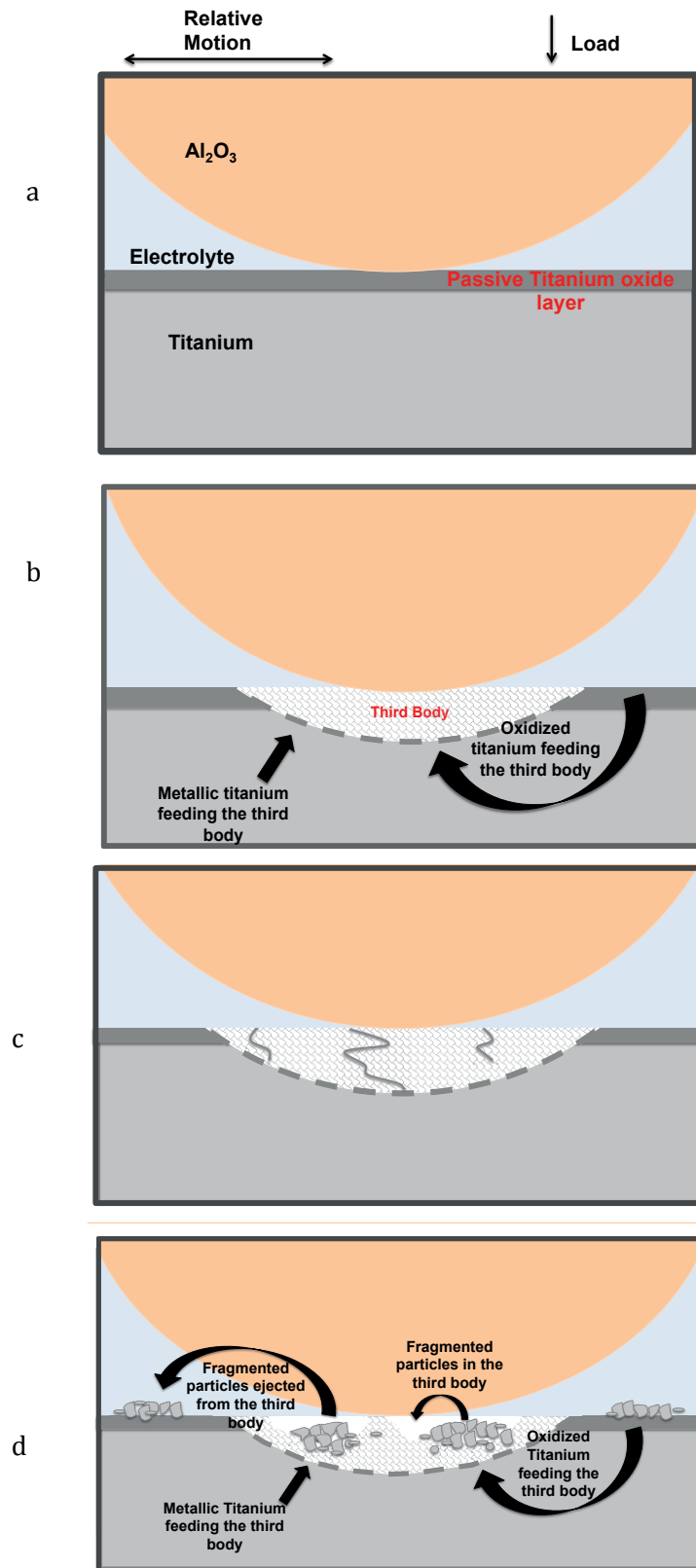


Figure 7-1. Third body formation a) Initial state, b) Third body layer formed in the interface by metallic and oxidized particles, c) fragmentation, d) third body evolution.

7.2 Compartments and flows

Four compartments are defined, which are the state variables of the system describing the total mass of the different materials of the system. For instance, C_1 is related to the total mass of the metallic substrate, C_2 is the compartment related to the metallic particles in the friction film, C_3 is the compartment that contains oxide particles in the friction film and C_4 is the metal particle concentration in the electrolyte or the re-deposition compartment. Because the compartment C_1 can be considered infinitely large compared with the size of the friction film. It can be considered as infinite source of metal particles.

Assuming these considerations, the model for third body physical system proposed is presented in Figure 7-2, where material compartments can be related through mass flows, which in turn are described by well established laws.

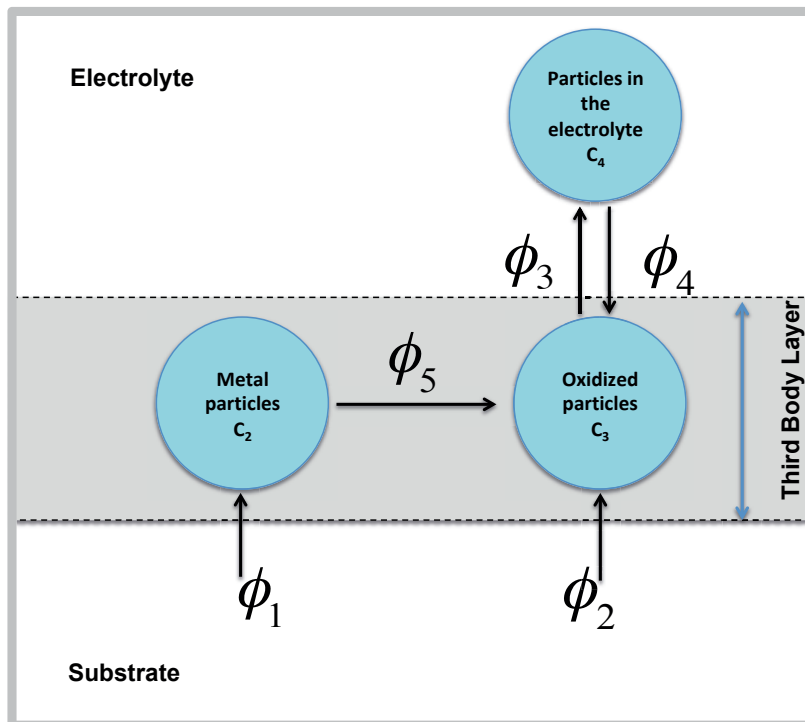


Figure 7-2. Schematic representation of the mass flow balance in the third body layer

Material flows from substrate to third body layer ($C_1 \rightarrow C_2 + C_3$):

Once rubbing starts, metallic and oxidized material particles are detached from the substrate. ϕ_1 and ϕ_2 represents these materials flows respectively that the third body.

- ϕ_1 , corresponds to metal particles removed from the substrate by mechanical wear and follows Archard's law. As a consequence this material flow has a proportional relation with the normal force (F_N); metal density (ρ_{met}); the sliding velocity under

fretting conditions (v_s), and to K_1 which is a proportionality constant (wear rate constant of the metallic material) and an inverse relation to material hardness (H). Two additional considerations should be done: Firstly, under fretting sliding velocity corresponds to the effective distance divided by the time that takes one stroke. Secondly, as the removal material from the substrate is affected once the third body layer is formed, an additional term taking into account this mechanical compliance effect should be introduced. This is called **stress transmission factor (STF)**. This factor represents the alteration of the maximum stress transmitted to the substrate as a function of the third body layer thickness and must depend of the mechanical properties of the layer.

$$\phi_1 = K_1 \cdot \rho_{met} \cdot v_s \cdot \frac{F_N}{H} \cdot STF \quad (26)$$

- ϕ_2 is the oxidized material detached from the substrate due to the wear accelerated corrosion, which is defined by equation (27), v_s the sliding velocity, M_r is the molecular weight, n is the metal oxidation state and F is the Faraday constant. In addition, this flow is related to the passivation charge density (Q_p) and the stress transmission factor STF . Finally, K_2 in the expression correspond to a proportionality constant of the wear rate constant of the oxidized material.

$$\phi_2 = K_2 \cdot \frac{M_r}{n \cdot F} \cdot Q_p \cdot v_s \cdot \left(\frac{F_N}{H} STF \right)^{1/2} \quad (27)$$

Material flows from the third layer to the electrolyte ($C_2+C_3 \rightarrow C_4$):

- ϕ_3 is the mass flow leaving the contact from the third body in form of wear. Therefore, as observed in equation 28 this flow follows also Archard's law. Then the proportional effect of the normal force, the sliding velocity and the inverse proportion with hardness are considered. However, as this material flow is ejected from the third body, oxide density ρ_{ox} , oxide stoichiometric relation (r_{ox}), the third body hardness (H_{TB}) as well as the proportion of oxidized particles in the third body w_3 are introduced in this expression to consider the effect of this layer on the total wear. Finally, a proportional constant is included; K_3 corresponds to the wear rate coefficient, which value must be close to the total wear rate of Ti alloys.

$$\phi_3 = \frac{K_3}{H_{TB}} \cdot \rho_{ox} \cdot r_{ox} \cdot v_s \cdot F_N \cdot w_3 \quad (28)$$

As mentioned before, the third body is a mixture of metallic particles (compartment C_2), which fraction is w_2 , and oxidized particles (compartment C_3) represented by the fraction w_3 , relationship between them is given by equation 29. According to Auger analysis in chapter 6, all material ejected from the contact is oxidized.

$$w_2 + w_3 = 1 \quad (29)$$

- ϕ_4 represents the fragmented material particles broken because of the third body deformation. Those particles do not leave the contact and they reincorporate to the layer again. This flow is a portion of the total wear (ϕ_3). Then, these particles reincorporation can be written as the probability of being ejected or to remain in the contact, which is potential dependent as equation 30 shows.

$$\phi_4 = K_4 \cdot \phi_3 \cdot P(E) \quad 0 < x < 1 \quad (30)$$

However, based on the experimental results presented in chapter 6 (SEM images), the proportion of material redeposited on the surface is considered negligible in relation to the total wear. Therefore, ϕ_4 is neglected.

Material flows inside third body layer ($C_2 \rightarrow C_3$):

- ϕ_5 , represents the chemical oxidation of metal particles inside of the friction film. It follows the wear accelerated corrosion law and it is considered proportional to the metal particles proportion (w_2) in the third body layer. The amount of metal particles in the third body limits the amount of material that can get oxidized.

$$\phi_5 = K_5 \cdot \frac{M_r}{n \cdot F} \cdot Q_p \cdot v_s \cdot \left(\frac{F_N}{H_{TB}} \right)^{1/2} \cdot w_2 \quad (31)$$

From this model, chemical volume rate and total volume rate the system can be obtained as observables and described by equation 32 and 33. Chemical volume rate can be calculated by the sum of the flow of material subjected to wear-accelerated corrosion phenomena of the bulk material and the flow, which represents the oxidation of the metallic particles inside the third body. While the total volume rate is the material that leaves the contact.

$$V'_{chem} = \phi_2 + \phi_5 \quad (32)$$

$$V'_{Tot} = \phi_3 \quad (33)$$

7.3 Mass balance

The dynamics of this system can be described by a set of ordinary differential equations in order to interpret the third body phenomenon through a mass flow process. Then, the evolution of the mass compartments C_2 , C_3 and C_4 are described by equation 34 to 36.

$$\frac{dC_2}{dt} = \phi_1 - \phi_5 \quad (34)$$

$$\frac{dC_3}{dt} = \phi_2 - \phi_3 + \phi_5 \quad (35)$$

$$\frac{dC_4}{dt} = \phi_3 \quad (36)$$

The friction film generated between two materials in contact under a tribochemical action evolves with time as is defined by equations 34 and 35.

Along the time, the third body formed reaches a constant thickness where the proportion of material feeding the layer is equal to the proportion of material being ejected from the contact (equation 37).

$$\phi_3 = \phi_1 + \phi_2 \quad (37)$$

Therefore, the sizes of the compartments C_2 and C_3 are constants over time. This stage is known as the **steady state** and equations 38 and 39 can be written as:

$$\phi_2 + \phi_5 - \phi_3 = 0 \quad (38)$$

$$\phi_1 - \phi_5 = 0 \quad (39)$$

7.4 Model calibration

To solve these equation systems to obtain total wear and chemical wear rate, six parameters related to the substrate and to the third body needs to be calculated. Those parameters are: K_1 , K_2 , K_3 , K_5 , Q_p and STF . Then, in order to get those unknowns values, the model calibration was divided in two steps

- **Parameters related to substrate:** To calculate the passivation charge density Q_p and wear rate constants K_1 and K_2 , data from the literature was used.
- **Parameters related to the third body:** To obtain STF , K_3 and K_5 a set of experimental data from a specific fretting-corrosion condition carried out in *In-Vitro* condition described in chapter 6 was used.

In both cases, the steady state was assumed.

Calculation of parameters relative to the substrate

7.4.1 Passivation charge density

The passivation charge density, Q_p , is the charge needed for the electrochemical formation of the protective oxide layer on the metal surface by unit area. Considering that a uniform oxide layer is formed on the metal with a thickness d_{ox} , the volume, V_{ox} , and the mass, m_{ox} , of the oxide layer can be defined as;

$$V_{ox} = d_{ox} \cdot A \quad (40)$$

$$m_{ox} = \rho_{ox} \cdot V_{ox} \quad (41)$$

The number of moles forming the oxide layer, n_{ox} , can be calculated if the composition is known:

$$Q = n_{(mol\ Ox)} \cdot z \cdot F = \frac{m_{ox}}{M_{ox}} \cdot z \cdot F = \frac{\rho_{ox} \cdot V_{ox}}{M_{ox}} \cdot z \cdot F \quad (42)$$

Where the M_{ox} is molecular weight of the oxide. Using the Faraday's law, which relates the charge transferred in an electrochemical process and the mass transformation, it is possible to define the passivation charge density as:

$$n_{(mol\ Ox)} = \frac{m_{ox}}{M_{ox}} \quad (43)$$

Where, $n_{mol\ ox}$ is the oxide mol number (mol), z is valence number of ions in the oxide and F is the Faraday's constant (C eq.). Finally, the passivation charge density is defined as:

$$Q_p = \frac{Q}{A} = \frac{\rho_{ox} \cdot d_{ox}}{M_{ox}} \cdot z \cdot F \quad (44)$$

For practical reasons, an area (A) of 1 cm² was considered and TiO₂ as the oxide formed. To calculate the oxide thickness (equation 45) as a function of the potential, a linear

growth is assumed with a rate of 2nm/V [134]. The intercept was calculated based on the oxide thickness data as a function of the potential (P) reported by Verges [134]. Calculated oxide thicknesses are listed in Table 7-1.

$$d_{ox}(nm) = 2 \left(\frac{nm}{V} \right) \cdot P(V) + 5(nm) \quad (45)$$

Table 7-1. Titanium oxide thickness and passivation charge as a function of potential (V_{SHE}).

| Potential | -1V | 0.3V | 0.5V | 1V |
|---------------------------|--------------------|----------------------|--------------------|--------------------|
| d (cm) | 3×10^{-7} | 5.6×10^{-7} | 6×10^{-7} | 7×10^{-7} |
| Q_p (Cm ⁻²) | 61.2 | 114 | 122 | 142 |

7.4.2 Proportionality constants K_1 and K_2

Constants K_1 and K_2 are associated to metallic material worn from the substrate in absence of third body layer. Then, equations 38 and 39 are reduced to:

$$\phi_2 - \phi_3 = 0 \quad (46)$$

$$\phi_1 - \phi_3 = 0 \quad (47)$$

From a literature search, Galliano et al [119] work was chosen. In this work a Ti6Al4V/Al₂O₃ couple was evaluated in a ball on flat configuration under sliding tribocorrosion test, none third body layer was observed after 1 hour of test as was indicated in the surface analysis reported.

Therefore, K_1 and K_2 were determined using Galliano et al [119] data listed in Table 7-2 to feed equations 32-33, 46 and 47. These equations were solve using the software Wolfram Mathematica 11.

Calculated values for K_1 and K_2 are **1.46x10⁻³** and **2.15**, respectively.

Table 7-2. Parameters used to calculate K_1 and K_2 . Galliano et al [119]

| Parameter | Value |
|------------------------------------|-----------------------|
| F_N (N)* | 2 |
| H (N/m ²)* | 3.17×10^9 |
| Sliding speed (ms ⁻¹)* | 1.28×10^2 |
| Potential (V)* | 0.3 |
| Q_p (C.m ⁻²) | 114 |
| V_{Tot} (cm ³) | 2.52×10^{-5} |
| I (A) | 7.9×10^{-5} |

Calculation of parameters relative to the third body

7.4.3 Stress transmission factor

In order to determine the mechanical effect of the third body on the system, the stress transmission factor was developed.

$$STF = \frac{\sigma_{interface}}{\sigma_{surface}} \quad (48)$$

This factor is defined as the ratio between the maximum shear stress in the third body/substrate interface ($\sigma_{interface}$) and the shear stress contact in the surface ($\sigma_{surface}$). Stresses were calculated through a MATLAB code following the von mises yield criterion [135], [136], which allow to analytically determine all the components of the tensions in any point of a semi-space for a contact of a sphere sliding on a plane. This criterion is a combination of Hertzian stresses and the stresses under sliding given a unique value for all the stresses acting. The maximum stress varies as a function of the third body thickness, therefore the stress transmission factor also change with it.

Shear stresses represented in Figure 7-3a were calculated for the ball on flat configuration used for Ti6Al4V/Al₂O₃ couple in the fretting-corrosion experiments described in chapter 6.

As the Von Misses stress is calculated taking into account the mechanical properties of the materials couple and the coefficient of friction, theoretical values for Ti6Al4V and Al₂O₃ properties were assumed, such as the elastic modulus and Poisson ratio (115GPa, 0.34 for Ti6Al4V; 350GPa, 0.21 for Al₂O₃). COF values were taken from values obtained during experiments (Table 6-1). Accordingly, the STF was calculated for three COF under two loads, which corresponds to the experimental values registered under cathodic conditions (-1V, F_N=10N) and anodic conditions (0.5V, F_N=10N and 30N).

Figure 7-3a represents the distribution in the vertical plane below the point of contact (as sketched in Figure 7-3b shows) and in the direction of the movement to the right.

Maximum shear stresses (marked on the Figure 7-3a with a red cross) according to the depth are calculated. This depth is the equivalent of third body thickness. Therefore, maximum stresses values respect to the third body layer thickness are listed in Table 7-3.

As presented in the sketch, the thickness 0 corresponds to the material surfaces and the colored lines represent the isometric stresses around the contact area. Maximum stresses are localized in the top and decrease as a function of the depth. Horizontal axe corresponds the distances to the contact point, which is localized in 0.

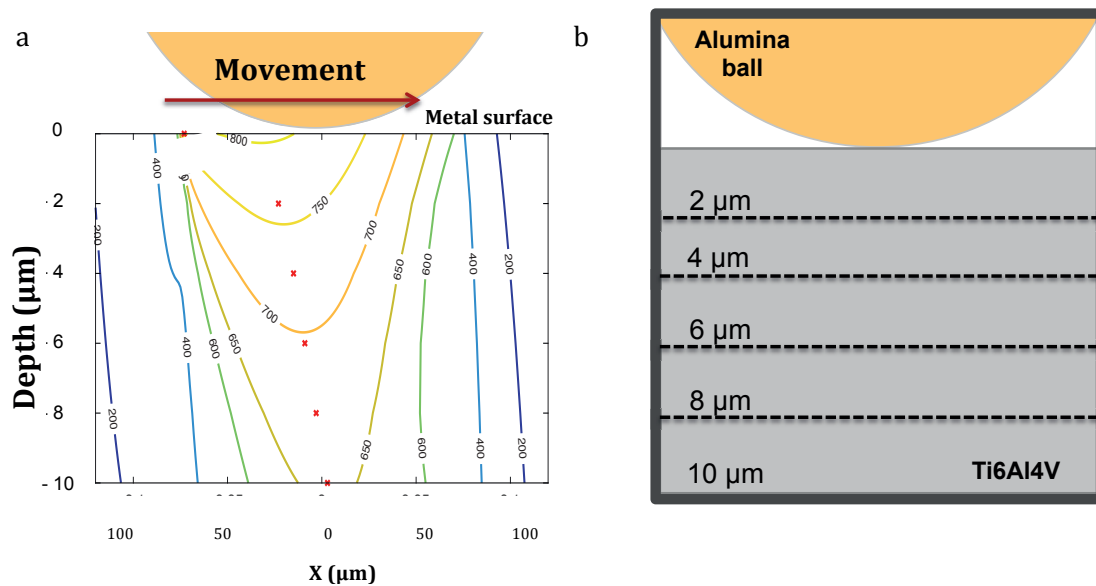


Figure 7-3. Contour of shear stresses in a Al_2O_3 /Ti6Al4V ball on flat configuration a) vertical stress distribution b) schematic representation of the contact for which tensions were calculated

From values in Table 7.3, the STF under fretting-corrosion conditions is represented in Figure 7-4. The STF calculated for the system under cathodic conditions and anodic conditions at the highest loads increases after the first two micrometers (curve green and purple). The shear stress distribution changes dramatically when the COF is lower than 0.25, which corresponds to theory, maximum stresses at lower COF are registered in the bulk material [137].

Table 7-3. Maximum stress calculated by the Von Misses criterion respect to the third body thickness

| Thickness (μm) | Von misses stress (MPa) | | |
|-----------------------------|-------------------------|----------|---------|
| | 10N/0.5V | 30N/0.5V | 10N/-1V |
| 0 | 812 | 1166 | 377 |
| 2 | 761 | 1116 | 333. |
| 4 | 724 | 1076 | 339 |
| 6 | 696 | 1041 | 352 |
| 8 | 673 | 1012 | 367 |
| 10 | 656 | 987 | 382 |

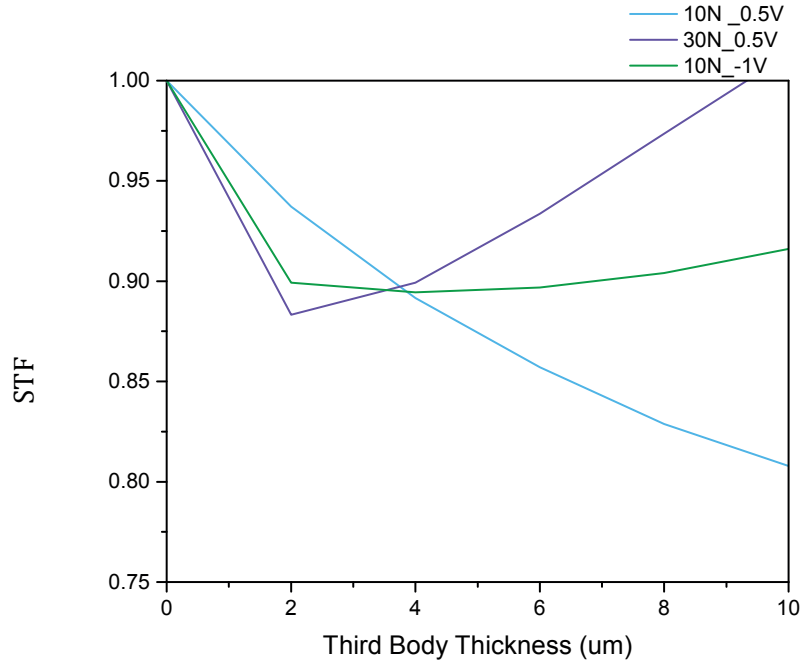


Figure 7-4. Stress transmission factor as a function of the third body thickness

7.4.4 Determination of unknown parameters K_3 and K_5

Finally, to calculate K_3 and K_5 values w the differential equation system presented in equations 38 and 39 had to be solved. Replacing flow expression in those equations, they can be rewritten as following:

$$K_2 \cdot \frac{M_r}{n \cdot F} \cdot Q_p \cdot v_s \cdot \left(\frac{F_N}{H} \cdot STF \right)^{1/2} + K_5 \cdot \frac{M_r}{n \cdot F} \cdot Q_p \cdot v_s \cdot \left(\frac{F_N}{H} \right)^{1/2} \cdot (1 - w_3) - \frac{K_3}{H_{TB}} \cdot \rho_{ox} \cdot r_{ox} \cdot v_s \cdot F_N = 0 \quad (49)$$

$$V'_{chem} = K_2 \cdot \frac{M_r}{n \cdot F} \cdot Q_p \cdot v_s \cdot \left(\frac{F_N}{H} \cdot STF \right)^{1/2} + K_5 \cdot \frac{M_r}{n \cdot F} \cdot Q_p \cdot v_s \cdot \left(\frac{F_N}{H_{TB}} \right)^{1/2} \cdot (1 - w_3) \quad (50)$$

Data from the experimental results were taken to calculate K_3 and K_5 values, the condition chosen had to be well described conditions and observables as well as a third body build-up. According to these requirements, experimental data from fretting-corrosion test carried out under a normal force of 10N at 0.5V was used. Those values are listed in Table 7-4 as well as the values of the calculated parameters presented above.

Calculated values K_3 and K_5 are 3.7×10^{-15} and 3.7 for respectively.

K_3 value, which is the third body wear rate values were confronted to values reported in literature for Ti and Titanium oxide wear rate. Due to the third body layer is a mixture of metallic and oxidized particles, K_3 values should be similar to values reported in Table 7-5 as it is the case.

Finally, K_2 value, which corresponds to the amount of material available for oxidation, it means in metallic state in the friction film. Its value should be close to the value for the substrate, it means the calculated K_2 .

Table 7-4. Experimental data and material properties used to calculate K_3 and K_5

| Parameter | Experimental values |
|--|------------------------|
| Potential (V) | 0.5 |
| Normal force, F_N (N) | 10 |
| Sliding velocity (m/s) | 9.0×10^{-5} |
| Total volume rate (Kg/s) | 1.72×10^{-13} |
| Chemical wear rate (Kg/s) | 1.54×10^{-13} |
| t (s) | 3600 |
| M (g/mol) | 48 |
| n | 4 |
| F (C/mol) | 96500 |
| ρ_{metal} (g/cm ³) | 4.43 |
| H (N/m ²) | 3.17×10^{-9} |
| H_{TB} (N/m ²) | 1.19×10^{-9} |
| V_s (m/s) | 1.28×10^{-2} |
| F_n (N) | 10 |
| Q_p (C/m ²) | 122.5 |
| ρ_{oxide} (g/cm ³) | 4.23 |
| K_1 | 1.46×10^{-3} |
| K_2 | 2.15 |
| STF | 0.94 |
| W_2 | 0.40 |

Table 7-5. Wear rate for different Titanium Alloys.

| Author | Year | Wear Rate (mm ³ /Nm) |
|--|------|---|
| A.F. Yetim [138] | 2010 | 1x10 ⁻¹⁰ - 4.5x10 ⁻¹² |
| K.M. Chen, Y. Zhou, X.X. Li, Q.Y. Zhang, L. Wang, S.Q. Wang [139] | 2015 | 1.5x10 ⁻¹⁵ - 6.5x10 ⁻¹⁵ |
| K. Aniołek, M. Kupka, A. Barylski, G. Dercz [140] | 2015 | 4x10 ⁻¹² - 1x10 ⁻¹³ |
| G. D. Revankar, R Shetty, S. S. Raoc, V. N. Gaitonde [141] | 2016 | 3.2x10 ⁻¹³ - 5x10 ⁻¹³ |
| Q.Y. Zhang, S.Q. Wang, Y. Zhou, K.M. Chen, L. Wang, X.H. Cui [142] | 2016 | 3x10 ⁻¹⁵ - 1.5x10 ⁻¹⁴ |

Finally, the calibrated mass flows are presented in the following equations.

$$\phi_1 = 1.46 \times 10^{-3} \cdot \rho_{met} \cdot v_s \cdot \frac{F_N}{H} \cdot STF \quad (51)$$

$$\phi_2 = 2.15 \cdot \frac{M_r}{n \cdot F} \cdot Q_p \cdot v_s \cdot \left(\frac{F_N}{H} STF \right)^{1/2} \quad (52)$$

$$\phi_3 = 3.7 \times 10^{-15} \cdot \rho_{ox} \cdot r_{ox} \cdot v_s \cdot F_N \cdot w_3 \quad (53)$$

$$\phi_5 = 3.7 \cdot \frac{M_r}{n \cdot F} \cdot Q_p \cdot v_s \cdot \left(\frac{F_N}{H} \right)^{1/2} \cdot w_2 \quad (54)$$

7.5 Model prediction

Once all parameters are defined, chemical volume wear rate and total volume wear rate could be predicted for a system under fretting corrosion conditions. Data from an independent study was taken to compare the prediction of the model to experimental data.

Third body layers were obtained by Barril et al [57], [58], [108] work, using a ball on flat configuration for Ti6Al4V/Al₂O₃ couple. In this study, parameters and observables were in detail described for different loads and electrochemical conditions. Calculation were made with parameters reported by the author [108] and listed in Table 7-6 and the STF value was taken from a curve calculated with the COF reported in this study

Table 7-6. Experimental data from Barril et al [108]

| Parameter | 0.5V | | | | -1V | -1V |
|--|---------------------|-----------------------|----------------------|----------------------|---------------------|----------------------|
| F_N (N) | 10 | | 30 | | 10 | 10 |
| Amplitude displacement (μm) | 50 | 100 | 50 | 100 | 50 | 100 |
| Sliding velocity (m/s) | $8. \times 10^{-5}$ | 1.80×10^{-4} | 5.0×10^{-5} | 1.5×10^{-4} | $4. \times 10^{-5}$ | 1.3×10^{-4} |
| Total wear ($\times 10^{-13}$ Kg/s) | 0.55 | 1.2 | 9.84 | 6.76 | 0.25 | 0.86 |
| | 2 | 4.5 | | | 1.6 | 0.35 |
| Chemical wear ($\times 10^{-13}$ Kg/s) | 0.73 | 1.60 | 0.79 | 5.48 | - | - |

Total wear volume rate was calculated for two amplitude displacements and two potentials, Figure 7-5. The model follows the effect of the amplitude displacement and electrochemical condition. However, predicted values are one order of magnitude higher than the total wear reported. Difference in values can correspond to dissimilar stiffness in the system. If the stiffness is higher the contact is closed, as consequence more particles get trap into the contact and third body layers are thicker. In addition, if the particles remain longer in the contact they will be deformed and in contact with the electrolyte during more time. So, more oxidized third body is expected.

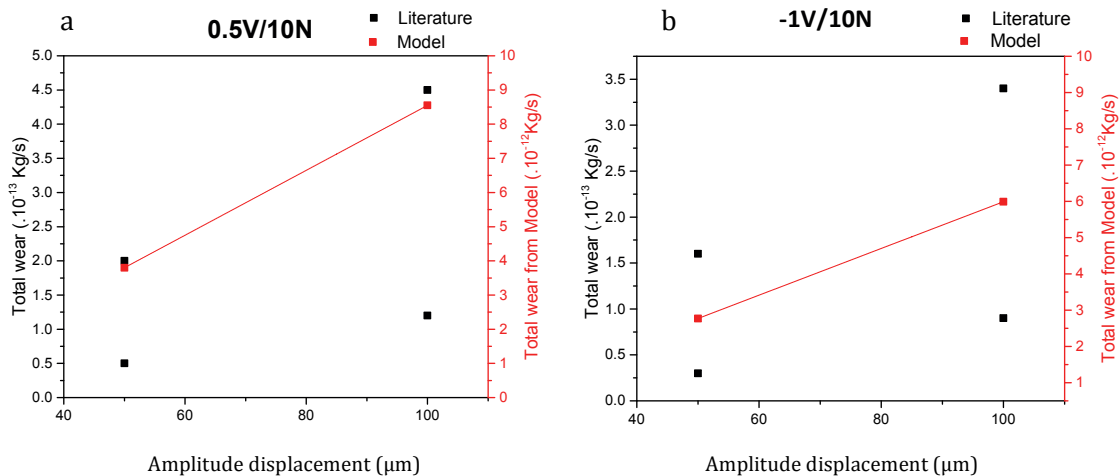


Figure 7-5. Comparison results from the model to values from the literature of the total wear volume rate as a function of the displacement and potential a) 0.5V and b) -1V

In order to check difference in the stiffness, a comparison was done between the slope of the transients loops reported by Barril et al [108] and the value obtained in the experiments carried out in this work. The stiffness values correspond to the loops registered under a normal load 10N, frequency 1Hz at 0.5V, which are the conditions

used to calibrate the model. Stiffness value reported by Barril et al [108] is $1.1\text{N}\cdot\mu\text{m}^{-1}$ while the value calculated from the experimental loops from Figure 6-2a is $0.5\text{N}\cdot\mu\text{m}^{-1}$. Accordingly, under the same load, frequency and electrochemical condition, thicker and more oxidized layers were found in Barril's work compared to the third body layers described in chapter 6, which corresponds to the difference in stiffness.

Different stiffnesses can be related to different factors as the sample holder but also to the mechanical properties of the contact, which depends of the material, the electrochemical conditions and surface properties of the sample (such roughness and hardness). The combined effect of these properties has an influence on the properties of the third body particles, which in turn affect strongly the stiffness [108]. Therefore, dissimilarities identified in the third body layers formed under the same load, frequency and electrochemical conditions but different stiffness, indicate a reciprocal effect. The stiffness drives to longer or shorter residence time of the particles in the contact, leading changes in the thickness and oxidation degree. This influences finally the mechanical properties (as hardness) and the surface energy of those particles modifying the wear.

In other words, under systems where the stiffness is higher the redeposition will have a strong influence on wear, as a consequence it cannot be neglected. Therefore, the dissimilarity between the total wear value reported in the literature and the value calculated through the model corresponds to the redeposition flow, ϕ_4 .

The prediction for the chemical volume wear rate was also done. To evaluate the model prediction, the same electrochemical condition was considered (0.5V) but under different loads. Because of the negative currents (hydrogen evolution masking the oxidation current of metal) chemical wear cannot be determined at -1V applied potential.

Values calculated for chemical volume follows the effect of the amplitude displacement and load as Figure 7.6 shows. Values obtained are in the same order of magnitude. Barril et al [57], [58], [108] already probe experimentally that difference in the stiffness do not affect the chemical volume rate obtained from the current.

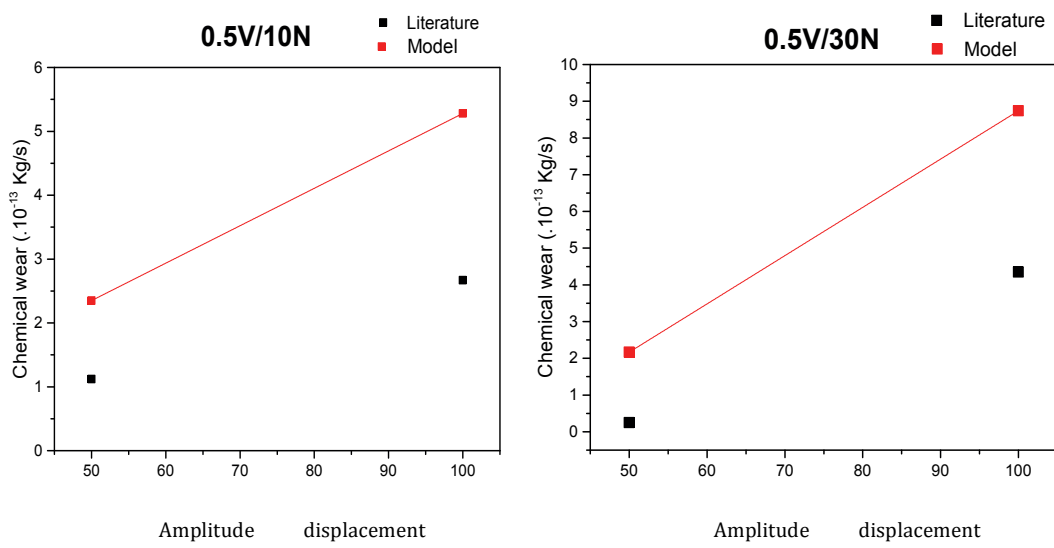


Figure 7-6. Comparison results from the prediction of the model and from experimental results from the literature of the chemical wear volume rate as a function of the displacement and normal force a) 10N and b) 30N

From these predictions values is noticed the influence of load, amplitude displacement and specially the electrochemical condition, which corresponds to what is observed experimentally.

The third body model proposed for fretting-corrosion is a promising tool to predict total wear but also to understand the evolution of the system as a function of mechanical and chemical key parameters. Comparison of model results and data from the literature shows that the model is able to predict total reasonable wear and chemical wear for systems where the mechanical response of the material in terms of elastic and plastic deformation is different.

8 Discussion

In recent years a large part of the discussion related to elucidating the degradation mechanisms of modular implants degradation has focused on crevice-corrosion phenomenon. One of the elements that supported this degradation mechanism lies on the geometrical configuration of head-neck and neck-head junctions, since once the prosthesis is assembled small crevices are created between the pieces.

Experimental results from the stainless steel Fe-Cr 15%, evaluated under the configuration mimicking the femoral head-neck junction, demonstrated the fact that this geometrical disposition promotes crevice-corrosion for alloys sensitive to this degradation mechanism. In addition, results from biomedical alloys evaluated under the same system show that even if the configuration, is able to reproduce crevice – corrosion deterioration, biomedical alloys resist and do not corrode under these conditions.

No deterioration evidence was found in Ti6Al4V and CoCr after crevice-corrosion experiments in several conditions using a geometry mimicking the femoral head-neck configuration. Those results demonstrated that crevice-corrosion unlikely occurs even though the geometrical configuration favors the occurrence of this mechanism.

Both alloys were evaluated under several potentials. CoCr alloys were evaluated in passive and trans-passive potential while Titanium alloy samples were evaluate in passive and cathodic conditions as well as in a potential close to E_{cor} . In none of those cases deterioration signs were found over time, and what is even more meaningful no change in the potential between the surface and the interior of the crevice was recorded. In other words, even if the conditions favor crevice-corrosion conditions, the differential aeration cell is not sustained since there is no potential drop within the crevice that leads to a significant potential difference between the crevice and the surface. Consequently, the passive layer is not affected under these conditions.

Based on the experimental results, some assumptions were done to check the applicability of the IR-voltage model to modular hip joint configurations. The agreement of the experimental results with those obtained from modeling, support the validity of the

experimental approach and the applicability of the IR-Voltage to a crevice-corrosion approach mimicking the modular head-neck geometry.

As well as the experimental approach, results from modeling show no risk of crevice-corrosion occurrence under two pH conditions for a wide range of passivation potential. Moreover, 3D maps built from this model make possible to analyze under which conditions (chemical, geometrical or electrochemical) the system is prone to develop crevice-corrosion. 3D representations of the critical distance as a function of the combined effect of crevice gap, passivation potential and conductivity were done. From them, it was determined that crevice -corrosion occurs in configurations that mimics a modular joint for solution conductivities lower than $5 \times 10^{-6} \text{S/cm}$, which corresponds to pure water.

According to the relevant role of the solution conductivity and to extrapolate the system to the hip joint condition, estimations of d_c were done using synovial fluid conductivity measured in In-Vivo conditions by Igual et al[55]. For values in the range of $6 \times 10^{-2} \text{S/cm}$ to 0.1S/cm , crevice corrosion occurs above 558 μm for Ti6Al4V and 29 μm for CoCr taking as crevice current the highest value measured experimentally (acid pH). If this critical distance is calculated with current values measured at pH 5.6, which is closer to the real pH measured of the synovial fluid, critical distances are above 1630 μm for Ti6Al4V and 37 μm for CoCr. Taper's length are approximately 14 mm (0.14 cm)

As a consequence, based on the presented experimental and theoretical approach, crevice-corrosion of biomedical alloys, Ti6Al4V and CoCr, in trunnion/ball contact geometries is unlikely to occur and this because the necessary corrosion cell is not electrochemically sustainable in typical biological conditions.

Therefore, based on these results the attention should be focus on fretting-corrosion.

Indeed, this mechanism has been widely accepted as a degradation driver in modular hip joint implants. In addition, as shown earlier similar tribofilms to those found in retrieval studies have been originated in fretting-corrosion In-Vitro experiments. This indicates that degradation modular hip joint implants can be approached by the study of the third body build-up and the main conditions that interfere in its formation during fretting-corrosion.

As shown before in chapter 5, tribofilms, also called in this study as third body layer, properties depend largely on the electrochemical and mechanical conditions. Difference in composition, thickness and hardness were found as a function of the potential applied. The characteristics of this layer may have an influence in the wear rate of systems under fretting-corrosion. As a consequence, this work proposes a third body model based on mass flows from the base material to the electrolyte environment via a third body. This model describes wear and third body build-up in terms of the mechanical and electrochemical parameters

As observed in chapter 7, there is a discrepancy of experimental results obtain under very similar conditions but different contact stiffness. The stiffness is supposed to modify the redeposition flow (ϕ_4 in Figure 7-2) that was considered negligible in the model

calibration. A further development of the model will consist in quantitatively linking ϕ_4 to the contact stiffness and integrating into the model. In this way, crucial clinical parameters affecting contact stiffness such as geometry and impact force could be directly related to implant degradation.

Furthermore, to check the applicability of the third body to real hip joint conditions, data about the mechanics in the body and from the electrochemical conditions inside of the body are required as well as a careful inspection and characterization of tribofilms from retrieved implant.

9

Conclusions

Degradation of modular hip joint prosthesis has been associated to health complications such as adverse tissue reaction and high level of metallic ions in the body. Therefore, several deterioration mechanisms have been proposed to explain modular hip joint degradation, such as fretting-corrosion, crevice-corrosion, galvanic coupling, hydrogen embrittlement and pitting. However, as explained earlier from the mechanism proposed two of them possibly can take place in the implants, those mechanism are fretting-corrosion and crevice-corrosion. Consequently, this work aimed elucidating the occurrence of these phenomena under hip joint conditions and so, determining key factors governing the degradation. Therefore, based on the experimental and theoretical approaches carried out by this work the following conclusions are highlighted:

- Laboratory simulations of crevice-corrosion configuration mimicking hip joint trunnions were carried out in NaCl solution under different pH and applied potentials. Results determined that CoCr and Ti alloys do not suffer of crevice-corrosion under those conditions.
- Furthermore, it was found that the Pickering IR-Voltage model of crevice-corrosion correctly predicts the occurrence or not of crevice corrosion in the developed laboratory test set-up. Extrapolation of the IR-Voltage model to hip joint trunnions shows that crevice corrosion of CoCr and Ti alloys cannot take place in In-Vivo, under plausible chemical, electrochemical and geometrical conditions established in the modular configuration.
- This work shows that Pickering IR-Voltage is an effective tool to predict crevice-corrosion occurrence in a trunnion/ball contact geometry.
- Fretting model for Ti alloys based on chemical and mechanical induced material flows within the contact was developed and calibrated using dedicated laboratory experiments.
- Fretting-corrosion model describes wear as a function of critical mechanical and electrochemical parameters. This theoretical approach constitutes the first step to

integrate in future works, important parameters such as: stiffness and third body particles properties, due to their strong influence on wear.

- This work shows that a rigorous scientific approach based on established theoretical and experimental concepts can bring solid progress in the understanding of corrosion and retting corrosion of hip joints, this despite the complexity of the topic.

10 References

- [1] Australian Orthopaedic Association, 'National joint replacement registry (AOANJRR). Hip, knee & shoulder arthroplasty. Annual report 2017', Australian Orthopaedic Association, Australia.
- [2] M.L. Wolford, K. Palso, A. Bercovitz, 'Hospitalization for total hip replacement among inpatients aged 45 and over: United States, 2000–2010', MD: National Center for Health Statistics, NCHS data brief, no 186. Hyattsville.
- [3] H. Maradit Kremers *et al.*, 'Prevalence of Total Hip and Knee Replacement in the United States', *J. Bone Joint Surg. Am.*, vol. 97, no. 17, pp. 1386–1397, Sep. 2015.
- [4] 'Patient Huefte'. [Online]. Available: <https://www.implantcast.de/fuer-patienten/patient-huefte/>. [Accessed: 22-Jan-2018].
- [5] S. Affatato, '1 - The history of total hip arthroplasty (THA)', in *Perspectives in Total Hip Arthroplasty*, Woodhead Publishing, 2014, pp. 3–18.
- [6] C. I. Esposito, T. M. Wright, S. B. Goodman, and D. J. Berry, 'What is the Trouble With Trunnions?', *Clin. Orthop. Relat. Res.*, vol. 472, no. 12, pp. 3652–3658, Dec. 2014.
- [7] A. J. Wassef and T. P. Schmalzried, 'Femoral taperosis', *Bone Amp Jt. J.*, vol. 95-B, no. 11 Supple A, p. 3, Nov. 2013.
- [8] G. Bergmann *et al.*, 'Hip contact forces and gait patterns from routine activities', *J. Biomech.*, vol. 34, no. 7, pp. 859–871, 2001.
- [9] S. Virtanen, I. Milošev, E. Gomez-Barrena, R. Trebše, J. Salo, and Y. T. Konttinen, 'Special modes of corrosion under physiological and simulated physiological conditions', *Acta Biomater.*, vol. 4, no. 3, pp. 468–476, May 2008.
- [10] N. Diomidis, S. Mischler, N. S. More, and M. Roy, 'Tribo-electrochemical characterization of metallic biomaterials for total joint replacement', *Acta Biomater.*, vol. 8, no. 2, pp. 852–859, Feb. 2012.
- [11] P. Hernigou, S. Queinnec, and C. H. Flouzat Lachaniette, 'One hundred and fifty years of history of the Morse taper: from Stephen A. Morse in 1864 to complications related to modularity in hip arthroplasty', *Int. Orthop.*, vol. 37, no. 10, pp. 2081–2088, Oct. 2013.

- [12] S. H. Hothi, R. K. Whittaker, J. M. Meswania, G. W. Blunn, J. A. Skinner, and A. J. Hart, 'Influence of stem type on material loss at the metal-on-metal pinnacle taper junction', *Proc. Inst. Mech. Eng. [H]*, vol. 229, no. 1, pp. 91–97, Jan. 2015.
- [13] H.S. Hothi *et al.*, 'Factors Associated With Trunnionosis in the Metal-on-Metal Pinnacle Hip', *J. Arthroplasty*, vol. 32, no. 1, pp. 286–290, Jan. 2017.
- [14] S. Jani, W. Sauer, T. McLean, R. Lambert, and P. Kovacs, 'Fretting Corrosion Mechanisms at Modular Implant Interfaces', in *Fretting Corrosion Mechanisms at Modular Implant Interfaces*, 1997.
- [15] J. Parekh, H. Jones, N. Chan, and P. Noble, 'Effect of Angular Mismatch Tolerance on Trunnion Micro-Motion in Metal-on-Metal THA Designs', *Bone Amp Jt. J. Orthop. Proc. Suppl.*, vol. 95-B, no. SUPP 34, p. 261, Dec. 2013.
- [16] S. Hussenbocus, D. Kosuge, L. B. Solomon, D. W. Howie, and R. H. Oskouei, 'Head-Neck Taper Corrosion in Hip Arthroplasty', *BioMed Res. Int.*, vol. 2015, p. 758123, 2015.
- [17] S.B. Kocagöz *et al.*, 'Does taper angle clearance influence fretting and corrosion damage at the head–stem interface? A matched cohort retrieval study', *Use Ceram. Total Hip Arthroplasty Contemp. Issues*, vol. 24, no. 4, pp. 246–254, Dicembre 2013.
- [18] M. L. Mroczkowski, J. S. Hertzler, S. M. Humphrey, T. Johnson, and C. R. Blanchard, 'Effect of impact assembly on the fretting corrosion of modular hip tapers', *J. Orthop. Res.*, vol. 24, no. 2, pp. 271–279, Feb. 2006.
- [19] A. Rehmer, N. E. Bishop, and M. M. Morlock, 'Influence of assembly procedure and material combination on the strength of the taper connection at the head–neck junction of modular hip endoprostheses', *Clin. Biomech.*, vol. 27, no. 1, pp. 77–83, Jan. 2012.
- [20] K. Abdullah, 'Study of Factors Affecting Taper Joint Failures in Modular Hip Implant Using Finite Element', Shkelzen Cakaj (Ed.), , DOI: 10.5772/8973. Available from'; in *Modelling, Modeling Simulation and Optimization - Focus on Applications*, InTech, 2010, pp. 121–134.
- [21] L. Scholl, G. Schmidig, A. Faizan, K. TenHuisen, and J. Nevelos, 'Evaluation of surgical impaction technique and how it affects locking strength of the head–stem taper junction', *Proc. Inst. Mech. Eng. [H]*, vol. 230, no. 7, pp. 661–667, Apr. 2016.
- [22] S. Valet, B. Weisse, J. Kuebler, M. Zimmermann, C. Affolter, and G. P. Terrasi, 'Are asymmetric metal markings on the cone surface of ceramic femoral heads an indication of entrapped debris?', *Biomed. Eng. OnLine*, vol. 13, pp. 38–38, 2014.
- [23] H. Breme, V. Biehl, N. Reger, and E. Gawalt, 'Chapter 1a Metallic Biomaterials: Introduction', in *Handbook of Biomaterial Properties*, W. Murphy, J. Black, and G. Hastings, Eds. New York, NY: Springer New York, 2016, pp. 151–158.
- [24] D. W. Hoepfner and V. Chandrasekaran, 'Fretting in orthopaedic implants: A review', *Wear*, vol. 173, no. 1, pp. 189–197, Apr. 1994.
- [25] H. Kaesche, *Corrosion of Metals: Physicochemical Principles and Current Problems*. Springer, 2003.

- [26] ASM International, *Metals Handbook. Properties and Selection: Nonferrous Alloys and Special-Purpose Materials*, 10th ed., vol. 2. ASM International, 1990.
- [27] H. Breme, V. Biehl, N. Reger, and E. Gawalt, 'Chapter 1c Metallic Biomaterials: Titanium and Titanium Alloys', in *Handbook of Biomaterial Properties*, W. Murphy, J. Black, and G. Hastings, Eds. New York, NY: Springer New York, 2016, pp. 167–189.
- [28] K. G. Budinski, 'Tribological properties of titanium alloys', *Wear*, vol. 151, no. 2, pp. 203–217, Dec. 1991.
- [29] P. S. Pastides, M. Dodd, K. M. Sarraf, and C. A. Willis-Owen, 'Trunnionosis: A pain in the neck', *World J. Orthop.*, vol. 4, no. 4, pp. 161–166, Oct. 2013.
- [30] J. B. Mistry *et al.*, 'Trunnionosis in total hip arthroplasty: a review', *J. Orthop. Traumatol. Off. J. Ital. Soc. Orthop. Traumatol.*, vol. 17, no. 1, pp. 1–6, Mar. 2016.
- [31] G. Gkagkalis, P. Mettraux, P. Omoumi, S. Mischler, and H. A. Rüdiger, 'Adverse tissue reaction to corrosion at the neck-stem junction after modular primary total hip arthroplasty', *Orthop. Traumatol. Surg. Res.*, vol. 101, no. 1, pp. 123–126, Feb. 2015.
- [32] H. J. Cooper, R. M. Urban, R. L. Wixson, R. M. Meneghini, and J. J. Jacobs, 'Adverse Local Tissue Reaction Arising from Corrosion at the Femoral Neck-Body Junction in a Dual-Taper Stem with a Cobalt-Chromium Modular Neck', *J. Bone Joint Surg. Am.*, vol. 95, no. 10, pp. 865–872, May 2013.
- [33] M. Huber, G. Reinisch, G. Trettenhahn, K. Zweymüller, and F. Lintner, 'Presence of corrosion products and hypersensitivity-associated reactions in periprosthetic tissue after aseptic loosening of total hip replacements with metal bearing surfaces', *Acta Biomater.*, vol. 5, no. 1, pp. 172–180, Jan. 2009.
- [34] E Ingham and J Fisher, 'Biological reactions to wear debris in total joint replacement', *Proc. Inst. Mech. Eng. [H]*, vol. 214, no. 1, pp. 21–37, Jan. 2000.
- [35] L. O. Simonsen, H. Harbak, and P. Bennekou, 'Cobalt metabolism and toxicology—A brief update', *Sci. Total Environ.*, vol. 432, pp. 210–215, Aug. 2012.
- [36] L. Leyssens, B. Vinck, C. Van Der Straeten, F. Wuyts, and L. Maes, 'Cobalt toxicity in humans—A review of the potential sources and systemic health effects', *Toxicology*, vol. 387, pp. 43–56, Jul. 2017.
- [37] J. Jacobs *et al.*, 'Metal Release in Patients Who Have Had a Primary Total Hip Arthroplasty. A Prospective, Controlled, Longitudinal Study*', *JBJS*, vol. 80, no. 10, 1998.
- [38] J. L. Gilbert, C. A. Buckley, and J. J. Jacobs, 'In vivo corrosion of modular hip prosthesis components in mixed and similar metal combinations. The effect of crevice, stress, motion, and alloy coupling', *J. Biomed. Mater. Res.*, vol. 27, no. 12, pp. 1533–1544, Dec. 1993.
- [39] G.B. Higgs, J.A. Hanzlik, D.W. MacDonald, J.L. Gilbert, C. M. C.M. Rimnac, and S.M. Kurtz, 'Is Increased Modularity Associated With Increased Fretting and Corrosion Damage in Metal-On-Metal Total Hip Arthroplasty Devices?: A

- Retrieval Study', *J. Arthroplasty*, vol. 28, no. 8, Supplement, pp. 2–6, Sep. 2013.
- [40] C. M. Arnholt *et al.*, 'Mechanically Assisted Taper Corrosion in Modular TKA', *AAHKS Suppl.*, vol. 29, no. 9, Supplement, pp. 205–208, Sep. 2014.
- [41] C. Arnholt *et al.*, 'Microgrooved Surface Topography Does Not Influence Fretting Corrosion of Tapers in Total Hip Arthroplasty: Classification and Retrieval Analysis', in *Microgrooved Surface Topography Does Not Influence Fretting Corrosion of Tapers in Total Hip Arthroplasty: Classification and Retrieval Analysis*, 2015.
- [42] S. M. Kurtz *et al.*, 'Do Ceramic Femoral Heads Reduce Taper Fretting Corrosion in Hip Arthroplasty? A Retrieval Study', *Clin. Orthop.*, vol. 471, no. 10, pp. 3270–3282, Oct. 2013.
- [43] R. B. Waterhouse, 'Fretting wear', *Wear*, vol. 100, no. 1, pp. 107–118, Dec. 1984.
- [44] N. Fillot, I. Iordanoff, and Y. Berthier, 'Wear modeling and the third body concept', *Wear*, vol. 262, no. 7, pp. 949–957, Mar. 2007.
- [45] M. Godet, 'Third-bodies in tribology', *Wear*, vol. 136, no. 1, pp. 29–45, Feb. 1990.
- [46] D. Landolt, 'Passivity of Metals', in *Corrosion and Surface Chemistry of Metals*, 1st edition., EPFL Press, 2007.
- [47] J. Jackson and W. Boyd, 'Crevice Corrosion of Titanium', in *Crevice Corrosion of Titanium*, 1968.
- [48] M. M. Pariona and I. L. Müller, 'An electrochemical study of the crevice corrosion of titanium', *J. Braz. Chem. Soc.*, vol. 8, pp. 137–142, 1997.
- [49] J. C. Griess, 'Crevice Corrosion of Titanium in Aqueous Salt Solutions', *Corrosion*, vol. 24, no. 4, pp. 96–109, April 1968.
- [50] J. S. Laub, 'Fretting Induced Fracture of Coupling Driven Shafts', presented at the International Compressor Engineering Conference, 1980.
- [51] K. G. Budinski, *Friction, Wear, and Erosion Atlas*. CRC Press, 2014.
- [52] R. Boyer, E.W. Collings, and G. Welsch, 'Titanium Alloys', in *Materials Properties Handbook*, OHIO: ASM International, 2007.
- [53] B.G. Pound, 'Corrosion behavior of metallic materials in biomedical applications. I. Ti and its alloys', *Corros. Rev.*, vol. 32, no. 1–2, p. 1, 2014.
- [54] D. C. Rodrigues, R. M. Urban, J. J. Jacobs, and J. L. Gilbert, 'In vivo severe corrosion and hydrogen embrittlement of retrieved modular body Titanium alloy hip-implants', *J. Biomed. Mater. Res. B Appl. Biomater.*, vol. 88, no. 1, pp. 206–219, Jan. 2009.
- [55] A. Igual Munoz, J. Schwiesau, B. M. Jolles, and S. Mischler, 'In vivo electrochemical corrosion study of a CoCrMo biomedical alloy in human synovial fluids', *Acta Biomater.*, vol. 21, no. Supplement C, pp. 228–236, Jul. 2015.
- [56] S. Barril, N. Debaud, S. Mischler, and D. Landolt, 'A tribo-electrochemical apparatus for in vitro investigation of fretting-corrosion of metallic implant materials', *Wear*, vol. 252, no. 9, pp. 744–754, May 2002.

- [57] S. Barril, S. Mischler, and D. Landolt, 'Influence of fretting regimes on the tribocorrosion behaviour of Ti6Al4V in 0.9wt.% sodium chloride solution', *Spec. Issue Wear Model.*, vol. 256, no. 9, pp. 963–972, May 2004.
- [58] S. Barril, S. Mischler, and D. Landolt, 'Electrochemical effects on the fretting corrosion behaviour of Ti6Al4V in 0.9% sodium chloride solution', *15th Int. Conf. Wear Mater.*, vol. 259, no. 1, pp. 282–291, Jul. 2005.
- [59] S. Y. Jauch, G. Huber, H. Haschke, K. Sellenschloh, and M. M. Morlock, 'Design parameters and the material coupling are decisive for the micromotion magnitude at the stem–neck interface of bi-modular hip implants', *Med. Eng. Phys.*, vol. 36, no. 3, pp. 300–307, Mar. 2014.
- [60] H. Haschke, S.Y. Jauch-Matt, K. Sellenschloh, G. Huber, and M. M. Morlock, 'Assembly force and taper angle difference influence the relative motion at the stem–neck interface of bi-modular hip prostheses', *Proc. Inst. Mech. Eng. [H]*, vol. 230, no. 7, pp. 690–699, May 2016.
- [61] D. Landolt, S. Mischler, M. Stemp, and S. Barril, 'Third body effects and material fluxes in tribocorrosion systems involving a sliding contact', *Spec. Issue Tribo-Corros.*, vol. 256, no. 5, pp. 517–524, Mar. 2004.
- [62] S. Guadalupe, C. Falcand, W. Chitty, and S. Mischler, 'Tribocorrosion in Pressurized High-Temperature Water: A Mass Flow Model Based on the Third-Body Approach', *Tribol. Lett.*, vol. 62, no. 1, p. 10, Mar. 2016.
- [63] H. W. Pickering, 'The significance of the local electrode potential within pits, crevices and cracks', *Ger.-Am. Colloq. Electrochem. Passiv.*, vol. 29, no. 2, pp. 325–341, Enero 1989.
- [64] H. W. Pickering, 'The role of electrode potential distribution in corrosion processes', *Mater. Sci. Eng. A*, vol. 198, no. 1, pp. 213–223, Jul. 1995.
- [65] M. I. Abdulsalam, 'Crevice Corrosion of Titanium in High Temperature-Concentrated Chloride Environments', *J. Mater. Eng. Perform.*, vol. 16, no. 6, pp. 736–740, Diciembre 2007.
- [66] M. I. Abdulsalam and H. W. Pickering, 'Effect of the applied potential on the potential and current distributions within crevices in pure nickel', *Corros. Sci.*, vol. 41, no. 2, pp. 351–372, Feb. 1998.
- [67] Y. Xu and H. W. Pickering, 'The Initial Potential and Current Distributions of the Crevice Corrosion Process', *J. Electrochem. Soc.*, vol. 140, no. 3, pp. 658–668, Mar. 1993.
- [68] K. Cho and H. W. Pickering, 'The Role of Chloride Ions in the $IR > IR^*$ Criterion for Crevice Corrosion in Iron', *J. Electrochem. Soc.*, vol. 138, no. 10, pp. L56–L58, Oct. 1991.
- [69] R. D. Klassen, P. R. Roberge, and C. V. Hyatt, 'A novel approach to characterizing localized corrosion within a crevice', *Electrochimica Acta*, vol. 46, no. 24, pp. 3705–3713, Agosto 2001.
- [70] J. C. Walton, G. Cragnolino, and S. K. Kalandros, 'A numerical model of crevice corrosion for passive and active metals', *Corros. Sci.*, vol. 38, no. 1, pp. 1–18, Enero 1996.
- [71] S. M. Sharland, 'A mathematical model of the initiation of crevice corrosion in metals', *Corros. Sci.*, vol. 33, no. 2, pp. 183–201, Feb. 1992.

- [72] G. F. Kennell, R. W. Evitts, and K. L. Heppner, 'A critical crevice solution and IR drop crevice corrosion model', *Corros. Sci.*, vol. 50, no. 6, pp. 1716–1725, Jun. 2008.
- [73] H. W. Pickering, 'IR drops and the local electrode potential during crevicing of iron', The Pennsylvania State University, United State, Technical Report, 1987.
- [74] H.W. Pickering and K. Cho, 'Demonstration of crevice corrosion in alkaline-solution without acidification', *J. Electrochem. Soc.*, vol. 137, no. 10, pp. 3313–3314, 1990.
- [75] Y. Xu and H. Pickering, 'A New Index for the Crevice Corrosion Resistance of Materials', in *A New Index for the Crevice Corrosion Resistance of Materials*, 1994.
- [76] A. Valdes and H.W. Pickering, 'IR drops and the local electrode potential during crevicing of iron', in *Advances in Localized Corrosion*, H.S. Isaacs, U. Bertocci, J. Kruger, S. Smialowska., Houston, TX: NACE, 1989.
- [77] H. W. Pickering, 'Important Early Developments and Current Understanding of the IR Mechanism of Localized Corrosion', *J. Electrochem. Soc.*, vol. 150, no. 5, pp. K1–K13, May 2003.
- [78] M. Niinomi, 'Mechanical biocompatibilities of titanium alloys for biomedical applications', *J. Mech. Behav. Biomed. Mater.*, vol. 1, no. 1, pp. 30–42, Jan. 2008.
- [79] M. Long and H. . Rack, 'Titanium alloys in total joint replacement—a materials science perspective', *Biomaterials*, vol. 19, no. 18, pp. 1621–1639, Sep. 1998.
- [80] H. J. Rack and J. I. Qazi, 'Titanium alloys for biomedical applications', *Proc. First TMS Symp. Biol. Mater. Sci.*, vol. 26, no. 8, pp. 1269–1277, Sep. 2006.
- [81] S. M. A. Hosseini and V. B. Singh, 'Active-passive behaviour of titanium and titanium alloy (VT-9) in sulphuric acid solution', *Mater. Chem. Phys.*, vol. 33, no. 1, pp. 63–69, Jan. 1993.
- [82] G. Mani, 'Chapter 1b Metallic Biomaterials: Cobalt-Chromium Alloys', in *Handbook of Biomaterial Properties*, W. Murphy, J. Black, and G. Hastings, Eds. New York, NY: Springer New York, 2016, pp. 159–166.
- [83] Y. Liao, E. Hoffman, M. Wimmer, A. Fischer, J. Jacobs, and L. Marks, 'CoCrMo Metal-on-Metal Hip Replacements', *Phys. Chem. Chem. Phys. PCCP*, vol. 15, no. 3, p. 10.1039/c2cp42968c, Jan. 2013.
- [84] ASM International. Handbook Committee, *ASM Handbook Vol 13. Corrosion*. USA: ASM International, 1990.
- [85] G. Mani, 'Chapter 1b Metallic Biomaterials: Cobalt-Chromium Alloys', in *Handbook of Biomaterial Properties*, W. Murphy, J. Black, and G. Hastings, Eds. New York, NY: Springer New York, 2016, pp. 159–166.
- [86] C. Yao, J. Lu, and T. J. Webster, '2 - Titanium and cobalt–chromium alloys for hips and knees', in *Biomaterials for Artificial Organs*, Woodhead Publishing, 2011, pp. 34–55.
- [87] A. W. E. Hodgson, S. Kurz, S. Virtanen, V. Fervel, C.-O. A. Olsson, and S. Mischler, 'Passive and transpassive behaviour of CoCrMo in simulated biological solutions', *Electrochimica Acta*, vol. 49, no. 13, pp. 2167–2178, May 2004.

- [88] N. Espallargas, A. Fischer, A. Igual Muñoz, S. Mischler, and M. A. Wimmer, 'In-situ generated tribomaterial in metal/metal contacts: Current understanding and future implications for implants', *Biotribology*, vol. 10, pp. 42–50, Jun. 2017.
- [89] B. Vicentini, D. Sinigaglia, and G. Taccani, 'Crevice corrosion of titanium. Behaviour of galvanic cell between shielded and unshielded titanium in sulphuric acid', *Corros. Sci.*, vol. 15, no. 6, pp. 479–492, Enero 1975.
- [90] N. Rajendran and T. Nishimura, 'Crevice corrosion monitoring of titanium and its alloys using microelectrodes', *Mater. Corros.*, vol. 58, no. 5, pp. 334–339, May 2007.
- [91] L. Chenghao, J. Li'nan, Y. Chuanjun, and H. Naibao, 'Crevice Corrosion Behavior of CP Ti, Ti-6Al-4V Alloy and Ti-Ni Shape Memory Alloy in Artificial Body Fluids', *Rare Met. Mater. Eng.*, vol. 44, no. 4, pp. 781–785, Abril 2015.
- [92] M. Akashi, G. Nakayama, and T. Fukuda, 'Initiation Criteria for Crevice Corrosion of Titanium Alloys Used for HLW Disposal Overpack', in *NACE-98158*, NACE, 1998.
- [93] K. L. Heppner and R. W. Evitts, 'Modelling of the effect of hydrogen ion reduction on the crevice corrosion of titanium A2 - Shipilov, S.A.', in *Environment-Induced Cracking of Materials*, R. H. Jones, J.-M. Olive, and R. B. Rebak, Eds. Amsterdam: Elsevier, 2008, pp. 95–104.
- [94] A. Kuhn, 'Corrosion of Co-Cr alloys in aqueous environments', *Biomaterials*, vol. 2, no. 2, p. 68–77, Apr. 1981.
- [95] T. M. Devine and J. Wulff, 'Closure to "Discussion of "The Comparative Crevice Corrosion Resistance of Co-Cr Base Surgical Implant Alloys" [T. M. Devine and J. Wulff (pp. 1433–1437, Vol. 123, No. 10)]"', *J. Electrochem. Soc.*, vol. 124, no. 6, pp. 869–870, Jun. 1977.
- [96] D. L. Levine and R. W. Staehle, 'Crevice corrosion in orthopedic implant metals', *J. Biomed. Mater. Res.*, vol. 11, no. 4, pp. 553–561, Jul. 1977.
- [97] L. Reclaru, R. Lerf, P.-Y. Eschler, A. Blatter, and J.-M. Meyer, 'Pitting, crevice and galvanic corrosion of REX stainless-steel/CoCr orthopedic implant material', *Biomaterials*, vol. 23, no. 16, pp. 3479–3485, 2002.
- [98] J. Goldberg, C. Buckley, J. Jacobs, and J. Gilbert, 'Corrosion Testing of Modular Hip Implants', in *Corrosion Testing of Modular Hip Implants*, 1997.
- [99] D. Landolt, S. Mischler, and M. Stemp, 'Electrochemical methods in tribocorrosion: a critical appraisal', *Electrochimica Acta*, vol. 46, no. 24, pp. 3913–3929, Aug. 2001.
- [100] N. Diomidis and S. Mischler, 'Third body effects on friction and wear during fretting of steel contacts', *Tribol. Int.*, vol. 44, no. 11, pp. 1452–1460, Oct. 2011.
- [101] J. Beard, 'The avoidance of fretting', *Mater. Des.*, vol. 9, no. 4, pp. 220–227, Jul. 1988.
- [102] K. J. Kubiak and T. G. Mathia, 'Influence of roughness on contact interface in fretting under dry and boundary lubricated sliding regimes', *17th Int. Conf. Wear Mater.*, vol. 267, no. 1, pp. 315–321, Jun. 2009.

- [103] J. Geringer, K. Kim, J. Pellier, and D. D. Macdonald, '3 - Fretting corrosion processes and wear mechanisms in medical implants', in *Bio-Tribocorrosion in Biomaterials and Medical Implants*, Y. Yan, Ed. Woodhead Publishing, 2013, pp. 45–73.
- [104] P. Kapsa, '4 - Environmental effects in fretting', in *Tribocorrosion of Passive Metals and Coatings*, Woodhead Publishing, 2011, pp. 100–117.
- [105] A. Igual Muñoz and S. Mischler, 'Effect of the environment on wear ranking and corrosion of biomedical CoCrMo alloys', *J. Mater. Sci. Mater. Med.*, vol. 22, no. 3, pp. 437–450, Mar. 2011.
- [106] V. Swaminathan and J. L. Gilbert, 'Fretting corrosion of CoCrMo and Ti6Al4V interfaces', *Biomaterials*, vol. 33, no. 22, pp. 5487–5503, Aug. 2012.
- [107] A. Igual Muñoz and N. Espallargas, '5 - Tribocorrosion mechanisms in sliding contacts', in *Tribocorrosion of Passive Metals and Coatings*, Woodhead Publishing, 2011, pp. 118–152.
- [108] S. Barril, 'Fretting corrosion of Ti6Al4V contribution to the in-vitro simulation of the femoral stem-bone cement interface', EPFL, 2003.
- [109] Y. Berthier, L. Vincent, and M. Godet, 'Fretting fatigue and fretting wear', *Tribol. Int.*, vol. 22, no. 4, pp. 235–242, Aug. 1989.
- [110] J. Duhart, S. Fouvry, and S. Gourdet, 'Application of plain fretting test to extract fatigue properties of materials', *Wear Mater. 2013*, vol. 301, no. 1, pp. 508–516, Apr. 2013.
- [111] T. E. Matikas and P. D. Nicolaou, 'Development of a model for the prediction of the fretting fatigue regimes', *J. Mater. Res.*, vol. 16, no. 9, pp. 2716–2723, 2001.
- [112] O. Vingsbo and S. Söderberg, 'On fretting maps', *Wear*, vol. 126, no. 2, pp. 131–147, Sep. 1988.
- [113] R. Wäsche and M. Hartelt, 'Fretting', in *Encyclopedia of Lubricants and Lubrication*, T. Mang, Ed. Berlin, Heidelberg: Springer Berlin Heidelberg, 2014, pp. 680–687.
- [114] S. Mischler, 'Electrochemical control of wear: a third body approach', in *Tribology Series*, vol. 41, Supplement C vols, D. Dowson, M. Priest, G. Dalmaz, and A. . Lubrecht, Eds. Elsevier, 2003, pp. 47–56.
- [115] H. Uhlig, 'Mechanism of fretting corrosion', *Trans. Am. Soc. Mech. Eng.*, vol. 21, no. 4, pp. 401–407, 1954.
- [116] S. Mischler, S. Debaud, E. A. Rosset, and D. Landolt, 'Surface degradation and third body formation in tribocorrosion systems', in *Tribology Series*, vol. 31, Supplement C vols, D. Dowson, C. M. Taylor, T. H. C. Childs, G. Dalmaz, Y. Berthier, L. Flamand, J.-M. Georges, and A. A. Lubrecht, Eds. Elsevier, 1996, pp. 623–629.
- [117] S. Mischler, S. Debaud, and D. Landolt, 'Wear-Accelerated Corrosion of Passive Metals in Tribocorrosion Systems', *J. Electrochem. Soc.*, vol. 145, no. 3, pp. 750–758, Mar. 1998.
- [118] S. Mischler, E. A. Rosset, and D. Landolt, 'Effect of Corrosion on the Wear Behavior of Passivating Metals in Aqueous Solutions', in *Tribology Series*, vol.

- 25, D. Dowson, C. M. Taylor, T. H. C. Childs, M. Godet, and G. Dalmaz, Eds. Elsevier, 1993, pp. 245–253.
- [119] F. Galliano, E. Galvanetto, S. Mischler, and D. Landolt, ‘Tribocorrosion behavior of plasma nitrided Ti–6Al–4V alloy in neutral NaCl solution’, *Surf. Coat. Technol.*, vol. 145, no. 1, pp. 121–131, Aug. 2001.
- [120] M. Stemp, ‘Tribocorrosion mechanisms of passivating metals under sliding wear conditions’, École Polytechnique Fédéral de Lausanne, 2001.
- [121] S. Cao, S. Guadalupe Maldonado, and S. Mischler, ‘Tribocorrosion of passive metals in the mixed lubrication regime: theoretical model and application to metal-on-metal artificial hip joints’, *Wear*, vol. 324–325, pp. 55–63, Feb. 2015.
- [122] S. Cao and S. Mischler, ‘Assessment of a recent tribocorrosion model for wear of metal-on-metal hip joints: Comparison between model predictions and simulator results’, *Wear*, vol. 362–363, pp. 170–178, Sep. 2016.
- [123] M. Baxmann, S. Y. Jauch, C. Schilling, W. Blömer, T. M. Grupp, and M. M. Morlock, ‘The influence of contact conditions and micromotions on the fretting behavior of modular titanium alloy taper connections’, *Med. Eng. Phys.*, vol. 35, no. 5, pp. 676–683, May 2013.
- [124] S. Hiromoto and S. Mischler, ‘The influence of proteins on the fretting–corrosion behaviour of a Ti6Al4V alloy’, *Tribocorrosion*, vol. 261, no. 9, pp. 1002–1011, Nov. 2006.
- [125] N. Diomidis, S. Mischler, N. S. More, M. Roy, and S. N. Paul, ‘Fretting–corrosion behavior of β titanium alloys in simulated synovial fluid’, *Wear*, vol. 271, no. 7, pp. 1093–1102, Jul. 2011.
- [126] M. Lgried, T. Liskiewicz, and A. Neville, ‘Electrochemical investigation of corrosion and wear interactions under fretting conditions’, *Wear*, vol. 282–283, pp. 52–58, Apr. 2012.
- [127] E. K. Ocran, L. E. Guenther, J.-M. Brandt, U. Wyss, and O. A. Ojo, ‘Corrosion and Fretting Corrosion Studies of Medical Grade CoCrMo Alloy in a Clinically Relevant Simulated Body Fluid Environment’, *Metall. Mater. Trans. A*, vol. 46, no. 6, pp. 2696–2709, Jun. 2015.
- [128] M. Pourbaix, *Atlas of Electrochemical Equilibria in Aqueous Solutions*. Pergamon Press, 1966.
- [129] J. W. Bullard and M. J. Cima, ‘Orientation Dependence of the Isoelectric Point of TiO₂ (Rutile) Surfaces’, *Langmuir*, vol. 22, no. 24, pp. 10264–10271, Nov. 2006.
- [130] A. Navrotsky, ‘Energetics of nanoparticle oxides: interplay between surface energy and polymorphism†’, *Geochem. Trans.*, vol. 4, pp. 34–34, 2003.
- [131] T.-D. Dang and T. T. H. Bui, ‘The Electrowetting and Corrosion Characterizations of Anodized As-Prepared Titanium Dioxide Nanotube’, *J. Electron. Mater.*, vol. 46, no. 6, pp. 3279–3284, Jun. 2017.
- [132] J. P. Holmberg, E. Ahlberg, J. Bergenholtz, M. Hassellöv, and Z. Abbas, ‘Surface charge and interfacial potential of titanium dioxide nanoparticles: Experimental and theoretical investigations’, *J. Colloid Interface Sci.*, vol. 407, pp. 168–176, Oct. 2013.

- [133] S. Guadalupe, S. Cao, M. Cantoni, W.-J. Chitty, C. Falcand, and S. Mischler, 'Applicability of a recently proposed tribocorrosion model to CoCr alloys with different carbides content', *21st Int. Conf. Wear Mater.*, vol. 376–377, pp. 203–211, Apr. 2017.
- [134] M.-G. Vergé, 'In-situ electrochemical quartz crystal microbalance studies of anodic film growth on valve metals', EPFL, 2003.
- [135] R. Hill, *The Mathematical Theory of Plasticity*. Clarendon Press, 1998.
- [136] G M Hamilton, 'Explicit Equations for the Stresses beneath a Sliding Spherical Contact', *Proc. Inst. Mech. Eng. Part C J. Mech. Eng. Sci.*, vol. 197, no. 1, pp. 53–59, Jan. 1983.
- [137] G. M. Hamilton and L. E. Goodman, 'The Stress Field Created by a Circular Sliding Contact', *J. Appl. Mech.*, vol. 33, no. 2, pp. 371–376, Jun. 1966.
- [138] A. F. Yetim, 'Investigation of wear behavior of titanium oxide films, produced by anodic oxidation, on commercially pure titanium in vacuum conditions', *Third Spec. Issue Dedic. Plasma Electrolysis*, vol. 205, no. 6, pp. 1757–1763, Dec. 2010.
- [139] K. M. Chen, Y. Zhou, X. X. Li, Q. Y. Zhang, L. Wang, and S. Q. Wang, 'Investigation on wear characteristics of a titanium alloy/steel tribo-pair', *Mater. Des. 1980-2015*, vol. 65, pp. 65–73, Jan. 2015.
- [140] K. Aniołek, M. Kupka, A. Barylski, and G. Dercz, 'Mechanical and tribological properties of oxide layers obtained on titanium in the thermal oxidation process', *Appl. Surf. Sci.*, vol. 357, pp. 1419–1426, Dec. 2015.
- [141] G. D. Revankar, R. Shetty, S. S. Rao, and V. N. Gaitonde, 'Analysis of surface roughness and hardness in ball burnishing of titanium alloy', *Measurement*, vol. 58, pp. 256–268, Dec. 2014.
- [142] Y. Zhou, Q. Y. Zhang, J. Q. Liu, X. H. Cui, J. G. Mo, and S. Q. Wang, 'Wear characteristics of a thermally oxidized and vacuum diffusion heat treated coating on Ti-6Al-4V alloy', *Wear*, vol. 344–345, pp. 9–21, Dec. 2015.

CURRICULUM VITAE

Ángela BERMÚDEZ CASTAÑEDA

Date of Birth : 11 July 1984

Nationality : Colombian

Email: angelabermudezcastaneda@epfl.ch

Education

- | | |
|-----------|---|
| 2014–2018 | Ph.D. in Materials Science, Swiss Federal Institute of Technology (EPFL), Lausanne, Switzerland. |
| 2010–2013 | Master of Engineering - major in Corrosion, Antioquia University , Medellín, Colombia |
| 2001–2009 | Bachelor of Materials engineer, Valle University, Cali, Colombia |

Professional Experiences

- | | |
|-----------------------|---|
| 2014 – 2018 | Doctoral candidate at the TIC laboratory of the Swiss Federal Institute of Technology in Lausanne (EPFL). Lausanne, Switzerland |
| 2013-2014 | Lecture in the construction materials course at Politécnico Colombiano Jaime Isaza Cadavid. Medellín, Colombia |
| 2007-2013 | Research Engineer at CIDEMAT research group of the Universidad de Antioquia. Medellín Colombia. |
| 2007-2010 Colombia | Quality and materials engineer at Industrias Haceb S.A. Copacabana, |

Distinctions

- | | |
|-----------|---|
| 2014-2018 | Swiss Government Excellence Scholarships for Foreign Scholars |
| 2014-2018 | Colciencias (2014-2018) – Loan-scholarship for Doctoral Studies |

Languages

Spanish : Mother tongue

English : Fluent

French : A1/A2

PUBLICATIONS LIST

Publications related to this thesis

Pending publications:

1. Bermudez, A., Mischler S. *Crevice-corrosion of biomedical alloys in hip joint configuration.*
2. Bermudez, A., Navarro-Laboulais, J., Mischler S. *Fretting-corrosion in biomedical alloys. A third body approach.*

Conferences

1. Bermúdez, J. Navarro-Laboulais, S. Mischler. *Crevice effect in systems under tribocorrosion conditions: Mechanisms competition.* In Eurocor 2017. Prague, Czech Republic.
2. Bermúdez, J. Navarro-Laboulais, S. Mischler. *Tribocorrosion Systems in presence of third body: Modelling for Fretting – Corrosion conditions.* Euro Friction Wear and Wear Protection 2017. Ettingen, Germany
3. J. Navarro-Laboulais, A. Bermúdez, S. Mischler, *Third-body Mass Balance Modelling for Tribocorrosion Systems.* In Eurocor 2016. Montpellier, France.
4. Bermúdez, A., Esguerra-Arce J., Esguerra-Arce A., Mischler, S. *Tribo-electrochemical resistance against bone of biomedical alloys.* In 21th Swiss Conference on Biomaterials and Regenerative Medicine. 2015. Lausanne, Switzerland.

Other publications

Peer-reviewed journals:

1. Bermúdez, A., Esguerra-Arce J., Esguerra-Arce A., Aguilar, Y., Mischler, S. *Fretting corrosion between bone and calcium phosphate-calcium titanate coatings,* (submitted to Wear)
2. Bedoya, F.E., Bermúdez, Á., Castaño, J.G, Echeverría F., Calderón J.E. *Electrochemical impedance study for modeling the anticorrosive performance of coatings based on accelerated tests and outdoor exposures.* Journal of Coatings Technology and Research (2016) 13: 895.
3. Bedoya, F.E., Calderón J.E., Bermúdez, Á., Castaño, J.G, Echeverría F., Maya-Montoya J. *New strategy to assess the performance of organic coatings during ultraviolet–condensation weathering tests.* Electrochimica Acta (2014): 124(1), 119-127

4. Bermúdez-Castañeda A., Castaño J.G., Echeverría F.. *Organic coatings deterioration: Mean models and quantification methods*. Revista Ingeniería y Desarrollo (2012), 30(2), 261-283.
5. Bedoya, F.E., Calderón J.E., Bermúdez, Á., Castaño, J.G, Echeverría F., Maya-Montoya J. *Análisis de los factores de mayor influencia en la evaluación del desempeño de recubrimientos orgánicos mediante ensayos acelerados y espectroscopia de impedancia electroquímica*. Ingeniería y Universidad (2011): 15(1), 245-268.

Conference proceedings

6. Bermúdez, A., Gallego, L.M., Castaño, J.G., Echeverría, F., Maya, J.G. *Compatibility study between anti-corrosion coatings, in UV/Condensation essays*. VIII Congreso Latinoamericano de Corrosión NACE 2012 . 2012. Lima, Perú.
7. Bermúdez, A., Bedoya, F.E., Gallego, L.M., Castaño, J.G., Calderón, J.A., Echeverría, F., Maya, J.G. *Influence of the electrochemical impedance spectroscopy measurements in the phenomenology of deterioration of organic coatings*, in VIII Congreso Latinoamericano de Corrosión NACE 2012 . 2012. Lima, Perú.
8. Bedoya, F.E., Bermúdez, A., Gallego, L.M., Castaño, J.G., Calderón, J.A., Echeverría, F., Maya, J.G. *Study of the durability of organic coatings by electrochemical impedance accelerated tests and statistical analysis*, in VIII Congreso Latinoamericano de Corrosión NACE 2012 . 2012. Lima, Perú.
9. Bedoya, F.E., Gallego, L.M., Calderón, J.A., Bermúdez, A., Castaño, J.G., Echeverría, F., Maya, J.G. *Evolution of the electrochemical properties of organic coatings after 12 hours of cyclic exposure in a UV/condensation chamber (ASTM D4587)*, in V Seminario Colombiano de Electroquímica. 2012. Medellín, Colombia.
10. Bedoya F.E., Gallego, L.M., Bermúdez, A., Castaño, J.G., Echeverría, F., Calderón, J.A. *Evolution of Electrochemical Properties of Organic Coatings During UV-Condensation Weathering Test*, in X Symposium on Electrochemical Methods in Corrosion Research. 2012. Maragorí, Brasil.
11. Bermúdez, Á., Castaño, J.G , Toro A. *Evaluation of Ni-P Coatings Modified with Magnetite Synthesized with and without Presence of Aluminium*. In XVIII International Materials Research Congress IMRC 2009.2009. Cancún – México.
12. Bermúdez, Á., Castaño, J.G , Toro A. *Evaluation of Ni-P Coatings Modified with Magnetite Synthesized with and without Presence of Aluminium*. In IV Cuarto Encuentro Nacional de Materiales. Universidad de Antioquia. 2208. Medellín – Colombia.

